

Electron Capture by Highly Charged Ions from Surfaces and Gases

DISSERTATION

zur Erlangung des akademischen Grades
doctor rerum naturalium
(Dr. rer. nat.)
im Fach Physik

eingereicht an der
Mathematisch-Naturwissenschaftlichen Fakultät I
der Humboldt-Universität zu Berlin

von
Frances Allen, M.Sci.
geboren am 22.12.1978 in Portsmouth, England

Präsident der Humboldt-Universität zu Berlin:
Prof. Dr. Christoph Marksches

Dekan der Mathematisch-Naturwissenschaftlichen Fakultät I:
Prof. Dr. Christian Limberg

Gutachter:

1. Prof. Dr. G. Fußmann
2. Prof. Dr. O. Benson
3. PD. Dr. Fritzsche

eingereicht am:	22. Oktober 2007
Tag der mündlichen Prüfung:	11. Januar 2008

Abstract

In this study highly charged ions produced in Electron Beam Ion Traps are used to investigate electron capture from surfaces and gases.

The experiments with gas targets focus on spectroscopic measurements of the *K*-shell x-rays emitted at the end of radiative cascades following electron capture into Rydberg states of Ar^{17+} and Ar^{18+} ions as a function of collision energy. The ions are extracted from an Electron Beam Ion Trap at an energy of 2 keV u^{-1} , charge-selected and then decelerated down to 5 eV u^{-1} for interaction with an argon gas target. For decreasing collision energies a shift to electron capture into low orbital angular momentum capture states is observed. Comparative measurements of the *K*-shell x-ray emission following electron capture by Ar^{17+} and Ar^{18+} ions from background gas in the trap are made and a discrepancy in the results compared with those from the extraction experiments is found. Possible explanations are discussed.

For the investigation of electron capture from surfaces, highly charged ions are extracted from an Electron Beam Ion Trap at energies of 2 to 3 keV u^{-1} , charge-selected and directed onto targets comprising arrays of nanoscale apertures in silicon nitride membranes. The highly charged ions implemented are Ar^{16+} and Xe^{44+} and the aperture targets are formed by focused ion beam drilling in combination with ion beam assisted thin film deposition, achieving hole diameters of 50 to 300 nm and aspect ratios of 1:5 to 3:2. After transport through the nanoscale apertures the ions pass through an electrostatic charge state analyzer and are detected. The percentage of electron capture from the aperture walls is found to be much lower than model predictions and the results are discussed in terms of a capillary guiding mechanism.

Keywords:

Highly Charged Ions, Electron Beam Ion Trap, electron capture, charge exchange

Zusammenfassung

In dieser Arbeit werden hochgeladene, mit einer Electron Beam Ion Trap produzierte Ionen für die Erforschung des Elektroneneinfangs von Oberflächen und Gasen eingesetzt.

Die Untersuchungen mit Gastargets konzentrieren sich auf die Energieabhängigkeit der Verteilung der K -Schalen-Röntgenstrahlen, die nach Elektroneneinfang in Rydberg-Zustände von Ar^{17+} und Ar^{18+} Ionen am Ende einer Kaskade von Elektronenübergängen entstehen. Die Ionen werden von der Ionenquelle mit einer Energie von 2 keV u^{-1} extrahiert, ladungsselektiert und anschließend bis auf 5 eV u^{-1} abgebremst, um dann mit einem Argon Gastarget zu interagieren. Für abnehmende Stoßenergien wird eine Verschiebung des Elektroneneinfangs in Zustände mit niedrigen Drehimpulsquantenzahlen beobachtet. Zum Vergleich wird auch die K -Schalen-Röntgenstrahlung auf Grund des Elektroneneinfangs bei Ar^{17+} und Ar^{18+} von dem Restgas in der Falle gemessen. Dabei wird eine Diskrepanz zu den Resultaten der Extraktionsversuche festgestellt. Mögliche Erklärungen werden diskutiert.

In den Untersuchungen zum Elektroneneinfang von Oberflächen werden hochgeladene Ionen von der Ionenquelle mit Energien von 2 bis 3 keV u^{-1} extrahiert, ladungsselektiert und auf Targets gelenkt. Diese bestehen aus Siliziumnitridmembranen mit einer Vielzahl nanometergroßer Löcher, welche mittels eines fokussierten Ionenstrahls in Kombination mit ionenstrahlinduzierter Abscheidung dünner Filme erstellt werden. Es werden hierbei Lochdurchmesser von 50 bis 300 nm mit Formfaktoren von 1:5 bis 3:2 erreicht. Bei den hochgeladenen Ionen handelt es sich um Ar^{16+} und Xe^{44+} . Nach dem Transport durch die Kapillare passieren die Ionen einen elektrostatischen Ladungstrenner und werden detektiert. Der Anteil des Elektroneneinfangs von den Wänden der Löcher ist weitaus geringer als Modellberechnungen vorhersagen. Die Resultate werden an Hand eines Kapillareffekts zur Ionenleitung diskutiert.

Schlagwörter:

Hochgeladene Ionen, Electron Beam Ion Trap, Elektroneneinfang, Ladungsaustausch

Contents

Preface	ix
1 Highly Charged Ions: An Introduction	1
2 The Electron Beam Ion Trap	11
2.1 Historical background	11
2.2 The EBIT device	14
2.2.1 Mode of operation	14
2.2.2 EBITs used in this work	19
2.3 Interaction processes in the trap	20
2.3.1 Electron impact ionization	21
2.3.2 Radiative collisions	22
2.4 Charge and temperature evolution in the trap	23
3 Experimental	29
3.1 The EBIT in magnetic trapping mode	30
3.1.1 Principles of magnetic trapping	30
3.1.2 The magnetic trapping experiment	31
3.2 Extraction of HCIs from an EBIT	33
3.2.1 Principles of extraction	33
3.2.2 The EBIT extraction beamline	34
3.2.3 Extraction onto a gas target	39
3.2.4 Extraction onto nanoscale apertures	43
4 Features of Charge Exchange Emission	51
4.1 Cascade simulations	51
4.2 Multiple electron capture	64

CONTENTS

5	Results and Discussion	67
5.1	Electron capture by HCIs from gases	68
5.1.1	X-ray emission from charge exchange in the EBIT . . .	68
5.1.2	X-ray emission from charge exchange at the gas target	82
5.1.3	Comparison of the <i>in situ</i> and extraction results	94
5.2	Electron capture by HCIs from surfaces	97
5.2.1	Transport of HCIs through nanoscale apertures	100
6	Conclusions and Outlook	111
	Acronyms	125
	List of Figures	127
	Acknowledgments	129
	Curriculum Vitae	133

Preface

The following chapters will guide the reader through the investigations of electron capture by highly charged ions (HCIs) from surfaces and gases carried out in the framework of this dissertation. The HCIs were generated using Electron Beam Ion Traps (EBITs) and electron capture was studied in three situations; in the trap itself via interactions with background gas, by extraction for collisions with an external gas target, and for the surface studies by extraction onto membranes perforated with nanoscale apertures.

In Chapter 1 an introduction to HCIs is given, detailing their abundance in the universe, unique properties and interactions with matter. The process of electron capture is discussed together with the motivation for the particular experiments carried out. An overview of laboratory devices for the production of HCIs is presented followed by a detailed description of the EBIT in Chapter 2.

Details of the various experimental methods implemented are given in Chapter 3. Electron capture by HCIs from gases was probed by measurements of x-ray emission. In the studies of electron capture by HCIs from surfaces, however, HCIs were transported through nanoscale apertures and the amount of electron capture was quantified by charge state analysis of the emergent beam.

The HCI-gas studies were conducted under the auspices of the Max Planck Institute for Plasma Physics at the former Division for Plasma Diagnostics, Berlin, and then at the Department for Plasma Physics at the Institute for Physics of the Humboldt University of Berlin. The HCI-surface studies were carried out during a one year research stay at the E. O. Lawrence Berkeley National Laboratory (LBNL), California, using two EBITs in the Accelerator and Fusion Research Division.

To set the scene for the interpretation of the spectroscopic measurements a range of simulated spectra are presented in Chapter 4. Then in Chapter 5 the experimental results are analyzed and discussed.

PREFACE

Finally, in Chapter 6 the results of the investigations of electron capture are summarized and suggestions for experimental improvements are made. The implications of the results of this thesis on other work are considered and conclusions are drawn.

Chapter 1

Highly Charged Ions: An Introduction

The vast majority of matter in the universe exists in an ionized state. This is due to the temperatures of millions of degrees which prevail in many parts of the cosmos, such as in stars, active galactic nuclei and supernova explosions. At these temperatures even the heaviest elements can become stripped of up to all of their electrons. The so-called HCIs which are subsequently formed are the most chemically reactive species known, scavenging for free electrons and the electrons of cooler matter in a bid to neutralize.

On Earth, however, in the absence of the extreme conditions of temperature found elsewhere in the universe, naturally occurring HCIs are rare. The terrestrial existence of naturally ionized species is mostly limited to low charge state ions of the light elements in the atmosphere, which are created as a result of ionization by ultraviolet radiation from the Sun, solar wind and cosmic rays, and in discharge events such as lightning strikes. Hence for the investigation of HCIs in the laboratory specialized sources have had to be developed. In fact, it was only recognized from the 1940s onwards that the exotic species which were being generated by artificial means might actually exist naturally elsewhere. The pivotal discovery was made by B. Edlén who, using laboratory data acquired with a vacuum spark ion source, identified many spectral lines in the solar corona as ‘forbidden’ transitions in the HCIs of calcium, iron and nickel [Edlén, 1942]. Since then the physics of HCIs has become firmly established as a very active area in contemporary scientific research. The field has developed from its origins in atomic physics towards a number of other disciplines including surface science, radiobiology,

astrophysics, nuclear and plasma physics. This has involved both investigations of a fundamental nature as well as work directed at a range of practical applications.

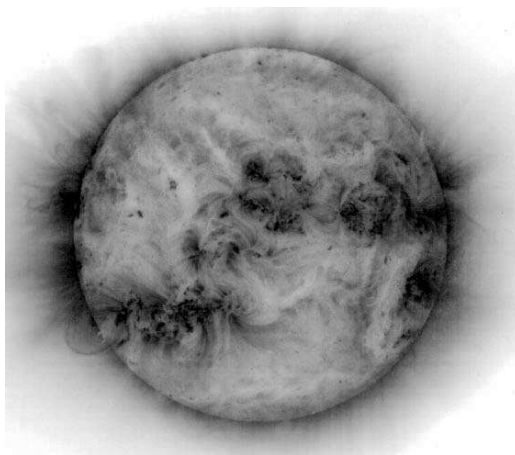


Figure 1.1: Image of the Sun resulting from the ultraviolet radiation emitted by Fe^{11+} ions in the solar corona.¹

The reason HCIs are important to such a broad spectrum of fields is predominantly due to the fact that many physical parameters scale with powers of the atomic number, Z [Gillaspy, 2001]. For example, the hyper-fine structure splitting, due to electron-nuclear overlap, scales with Z^3 , while the relativistic fine structure splitting and quantum electrodynamical Lamb shifts scale with Z^4 . Therefore experiments with HCIs enable sensitive tests of the theoretical models of atomic structure, on which most atomic reference data are based. The radiation emitted as a result of HCI interactions in space is routinely used to image cosmic objects and to track astrophysical events. This is illustrated in Figure 1.1, which shows an image of the Sun taken using the ultraviolet radiation emitted by Fe^{11+} ions in the solar corona. The spectroscopy of HCIs is also important for the understanding of solar flares, so that they might be accurately predicted in order to minimize the detrimental effects the energetic solar particles can have on satellite equipment and astronauts [Feldman et al., 2000; Gillaspy, 2001]. On a cosmological level, HCI research is even instrumental in estimating the age of the universe, as has

¹Credit: SOHO-EIT Consortium, ESA, NASA;
<http://antwrp.gsfc.nasa.gov/apod/ap010929.html>

been shown from the half-life measurements of radioactive HCIs of rhenium which exists in meteorites [Bosch, 1999].

HCIs are also central to many of the processes occurring in high temperature laboratory plasmas, as for example in the magnetically confined plasma of a Tokamak, the leading candidate for harnessing energy from nuclear fusion [Tawara, 2003]. The erosion of heavy elements from the Tokamak's cavity wall and subsequent ionization into high charge states in the hot plasma core gives rise to HCIs which then interact strongly with the electrons in the core plasma, predominantly leading to x-ray emission. It follows that when the amount of these so-called impurity ions becomes too high, severe cooling of the plasma core due to radiation losses can occur. However, the radiative emission from HCIs in the plasma is useful for spectroscopic diagnostics to determine key plasma parameters, such as temperature and density. These diagnostics can either be passive or active. Passive diagnostics are based on spectroscopic observations of impurity ions. Active diagnostics involve the injection of neutral particles or solid pellets which become ionized to form HCIs. These HCIs then undergo a range of measurable radiative interactions in the plasma.

Further applications of HCIs stem from their interactions with surfaces. HCIs carry an enormous amount of potential energy, given by the sum of the binding energies of the electrons removed. For example, by removing all the 92 electrons from a uranium atom, a HCI (bare U^{92+}) with a potential energy of 750 keV is generated. The potential energy of H^+ , in comparison, is a mere 13.6 eV. When these large amounts of energy are deposited on a solid target many secondary electrons and sputtered particles are produced. Consequently HCIs can be used for surface modifications and analysis [Schenkel et al., 1999]. In addition, the radiobiological effects of HCIs have been put to beneficial use in the particle beam therapy of inoperable tumours [Kraft, 2003].

This thesis focuses on aspects of electron capture, also known as charge exchange, in collisions of HCIs with surfaces and gases. In the interaction, a HCI captures one or more electrons into states of a high principal quantum number, the so-called Rydberg states, and the excited ion stabilizes by photon and/or Auger electron emission. For collision velocities much greater than the orbital velocity of the target electrons ($v_{Bohr} = 2.2 \cdot 10^6 \text{ ms}^{-1}$), ionization of the target, without capture into the HCI, dominates. In contrast, for low collision velocities of the order of the orbital velocity, target ionization followed by electron capture into the HCI is the dominant process. Hence

in the studies presented here ‘slow’ HCIs are used. Investigations of charge exchange are important in a fundamental sense, but also in various practical fields. For example in the determination of ion storage times in traps and storage rings [Stöhlker et al., 1998], or for spectral diagnostics of fusion plasmas heated by neutral beam injection [Tawara, 2003].

The experiments conducted in this work which use gas targets are further motivated by a particular discovery in astrophysics. Those implementing solid targets have been designed for a specific setup for single ion implantation. Details of these applications and the role of charge exchange in both are given below.

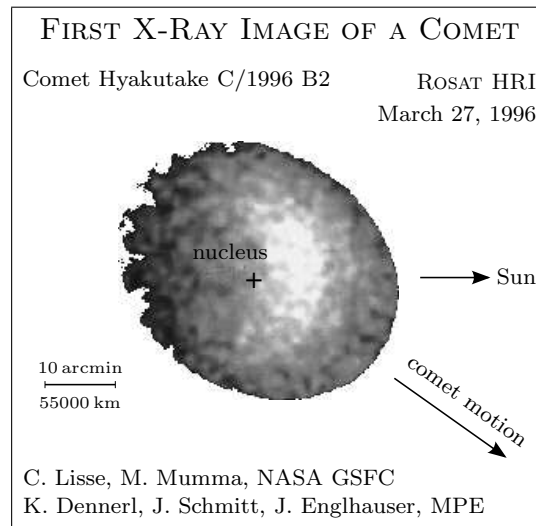


Figure 1.2: Comet Hyakutake and the first observation of cometary x-ray emission.²

The stimulus from astrophysics, which has heightened interest in HCI-gas charge exchange over the last decade, is the phenomenon of x-ray emission from comets. The discovery was made by Lisse *et al.* from measurements of comet Hyakutake using the Röntgen X-ray Satellite [Lisse et al., 1996] and produced the first ever x-ray image of a comet, shown in Figure 1.2. This finding was very surprising, since generally x-ray emission is associated with extremely hot sources. X-ray emission from numerous other comets has been confirmed [Dennerl et al., 1997], leading to the classification of all active

²Credit: C. Lisse, M. Mumma, K. Dennerl, J. Schmitt, and J. Englhauser;
<http://apod.nasa.gov/apod/ap960411.html>

comets as x-ray sources. Various emission mechanisms have been proposed, including Bremsstrahlung of solar wind electrons interacting with cometary gas or dust and the scattering of solar x-rays. However, the main cause of the emission has been established as charge exchange between HCIs in the solar wind and cometary gas [Cravens, 1997, 2002].

Cometary neutral species include H_2 , CO , H_2O and CO_2 , which become vaporized from the surface as the comet approaches the Sun. The composition of the solar wind, on the other hand, is identical to that of the solar corona, and thus predominantly consists of hydrogen ions with trace amounts of heavier ions, such as $\text{C}^{6+,5+}$, N^{6+} , $\text{O}^{7+,6+}$, Ne^{8+} , Si^{9+} and Fe^{12+} . The wind speed can be classified as having a slow ($\sim 4 \cdot 10^5 \text{ ms}^{-1}$, $\sim 0.8 \text{ keV u}^{-1}$) and a fast ($\sim 8 \cdot 10^5 \text{ ms}^{-1}$, $\sim 3.2 \text{ keV u}^{-1}$) component, with distinct relative ion abundances associated with each. In the coma (or atmosphere) of a comet, however, the solar wind ions can be decelerated to 50 eV u^{-1} and below [Krasnopolsky, 1997]. In fact, measurements of the cometary x-ray emission morphology have shown that up to 50 % of the emission might originate from inside the comet's bow shock, near the nucleus where the HCI velocity is the lowest [Lisse et al., 1999].

Since charge exchange emission is characteristic of the collision partners, it is proposed that cometary spectra can be used to probe the species of HCIs in the solar wind and neutrals in the coma [Beiersdorfer et al., 2003]. Furthermore, since in low energy collisions the angular momentum state into which an electron is captured depends strongly on collision velocity [Dijkamp et al., 1985] and the particular capture state determines the path of the subsequent radiative cascade, distinct emission spectra are expected from which the dynamics of the solar wind might be inferred [Beiersdorfer et al., 2001b]. During increased solar activity the solar wind is likely to contain more HCIs than usual, thus ultimately the comets could be used to monitor space weather without the need for heliospheric spacecraft. On Earth the detection of x-rays from space is restricted by atmospheric absorption, hence in order to carry out x-ray astronomy several orbiting x-ray observatories have been launched. A wealth of high precision data has been collected, in many cases surpassing the measurements made in the laboratory. For a review see [Beiersdorfer, 2003]. Thus for the interpretation of astrophysical spectra the atomic data available is often the limiting factor. In particular, laboratory data is lacking in the low energy regime relevant to the cometary spectra. The measurements of charge exchange spectra presented in this thesis aim to fill in some of the gaps.

As mentioned, the investigations in this work of electron capture by HCIs from surfaces are driven by a specific setup for single ion implantation. The implantation technique is under development by Schenkel *et al.* at LBNL and implements a low current beam of slow HCIs transported through a nanoscale hole in the cantilever of an Atomic Force Microscope (AFM) tip. Benchmark data on the transport of HCIs through small apertures are thus required. The ultimate goal of the project is to build a scalable test structure of solid state quantum bits to be used for quantum computation [Schenkel et al., 2003a]. Alignment of the implant beam is achieved by scanning the AFM tip across the target surface and the spatial resolution of the beam spot is controlled by the size of the nanoscale collimating aperture. In this way single ion implantation with nanometer precision can be achieved. This contrasts with the bulk implantation techniques which have become commonplace and are used widely in the semiconductor industry today.

In order to determine whether or not an ion has impacted at a particular location on the target a detection method is required. A possible approach makes use of the large numbers of secondary electrons which are produced when a HCI impacts a solid target, arising as a result of a combination of neutralization processes above and below the surface [Schenkel et al., 1999]. For example, for slow ($\sim 0.3 v_{Bohr}$) Xe^{44+} ions impacting a gold surface, the production of ~ 80 secondary electrons per incident ion has been measured, and an approximately linear increase in secondary electron yield with increasing charge state of the incident ion has been determined [Schenkel et al., 1997]. In the experiment at LBNL an externally applied magnetic field guides these secondary electrons away from the implant surface towards a fluorescent screen biased to a high positive voltage. The photons produced as a result of electron impact on the screen then travel through a light guide to a photomultiplier tube, the output pulse height of which is proportional to the number of incident photons per pulse and hence also to the number of secondary electrons generated for each HCI impact. A diagram showing the experimental arrangement for the single ion implantation technique is shown in Figure 1.3.

In a prototype device a silicon nitride membrane pierced with a nanoscale hole, mounted just above the aperture in the AFM cantilever, is used as a collimator. In the transport studies carried out for this thesis such membranes were used as the targets. This allowed the collection of data directly applicable to the materials used in the prototype. In addition, it enabled more experimental flexibility than would have been possible by using pierced

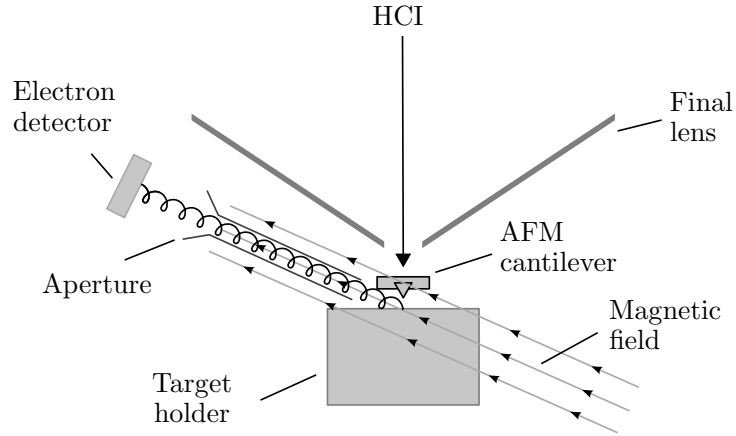


Figure 1.3: Setup for aligned single ion implantation using HCIs at LBNL.

AFM cantilevers alone. In fact, the transport of HCIs through small holes, or nanocapillaries, presents a very convenient method for the study of HCI-surface charge exchange. It was introduced by Y. Yamazaki and allows the extraction of HCIs which have captured electrons from the side walls into vacuum, where their relaxation processes can be studied [Yamazaki, 1997]. This contrasts with the situation for a planar target, where the HCI is destined to collide with the surface due to acceleration by its image charge potential. Recent work with slow, moderately charged ions and insulating capillary targets has also revealed an ion guiding effect by which charge exchange is suppressed [Stolterfoht et al., 2002]. Hence the experiments carried out here using silicon nitride targets are also of interest in this area.

For the production of HCIs in the laboratory a variety of devices has been developed, ranging from relatively small and inexpensive setups to very large scale multimillion projects, spanning kinetic energies of ions from almost at rest to the relativistic. Each source is associated with a select research niche, which combined make a broad spectrum of study possible.

Most laboratory ion sources are plasma-based and the earliest and most basic are of the discharge type, generating relatively low charge state ions via electron impact ionization following an electrical discharge between a cathode and an anode in a gas. Glow and arc discharge sources have been used in spectroscopy dating back to the 18th century, long before the underlying physical processes were understood or the full spectroscopic range could be measured. It was in the late 1920s that experimental studies of HCIs really

commenced, with the introduction of the vacuum spark ion source which operates at charging voltages and discharge currents of several tens of kilovolts and kiloamperes, respectively. Subsequent more exotic sources included exploding wires and imploding plasma devices. For a review see [Martinson, 1989].

High current beams of moderately charged ions and to a growing extent HCIs for injection into particle accelerators are commonly produced using Electron Cyclotron Resonance (ECR) ion sources [Leitner and Lyneis, 2004]. These are specialized microwave sources in which the gyrating electrons of a magnetically confined plasma are accelerated resonantly by microwaves at the cyclotron frequency. The high energy electrons ionize the atoms and ions in the plasma forming the HCIs which are then extracted. This concept was first proposed in 1969. Following the first device fabrications in the 1970s, a series of design improvements have increased output currents and charge states considerably. Moreover, recent advances in the fields of superconducting magnets and high frequency microwave generation have led to the ongoing development of even higher performance sources.

A further ion source currently benefitting from technological advances is the laser ion source which produces a plasma by irradiating a solid target with an intense laser beam, a technique introduced in the 1960s [Sharkov, 2004]. The high power density of the focused beam spot causes rapid electron heating, resulting in ionization and the production of a very dense, hot plasma. The HCIs in the plasma can either be investigated directly via spectroscopy or extracted to form a high current ion beam. Ion extraction from these relatively cheap and straightforward ion sources is appealing and applications include ion sources for accelerators and inertial fusion.

Relativistic beams of HCIs are produced using stripping techniques at heavy ion accelerator facilities such as at the Gesellschaft für Schwerionenforschung (GSI) in Darmstadt, Germany. On passing through the stripping medium, heavy ions become highly ionized and are then typically injected into storage rings for a range of experiments. Spectroscopy of relativistic ions, however, is hampered by Doppler broadening. In addition, the realization of low energy storage rings for HCIs is challenging due to the exceptionally high vacuum required to sufficiently reduce ion losses resulting from charge exchange.

The HCIs used in the experiments presented in this thesis were generated with an EBIT. This is a much smaller scale device than the facilities used to produce relativistic beams of HCIs. However, an EBIT is able to directly

create HCIs in the highest charge of states, surpassing the ionization capabilities of all other ion sources. In addition, the HCIs are very slow which makes them ideal for spectroscopic measurements. The EBIT is described in detail in the following chapter.

Chapter 2

The Electron Beam Ion Trap

This chapter begins with a historical overview of the development of the EBIT, followed by an explanation of its mode of operation. The myriad of interaction processes occurring in the trap is considered and to close, the evolution of ion temperature and charge states in the EBIT is discussed.

2.1 Historical background

An EBIT is a ‘table-top’ device for the production, confinement and study of HCIs which are almost at rest. It employs a quasi-monoenergetic, highly compressed electron beam to:

- 1) generate HCIs via successive electron-ion impact collisions;
- 2) radially confine the HCIs by its negative space charge;
- 3) excite the HCIs for spectroscopic investigations.

The ions can also be extracted for experiments with external targets.

The EBIT is based on a similar device called the Electron Beam Ion Source (EBIS) which was invented and first built in 1968 by Donets *et al.* at the Joint Institute for Nuclear Research in Dubna in the USSR [Donets, 1976; Donets and Ovsyannikov, 1981]. As an ion source, the EBIS is specialized for ion extraction and once the first model had proved successful at forming beams of HCIs, several design improvements were made leading to the installation of EBIS devices at various laboratories in a number of countries [Stöckli, 1991; Donets, 1998]. The most important development was the replacement of the permanent magnets which compressed the electron beam with a superconducting magnet. This enabled the production of higher ion charge states for the following reasons: Firstly, the higher magnetic field

created by the superconducting magnet results in increased compression and hence increased density of the electron beam, enhancing the rate of ionizing collisions. Secondly, cryopumping by the cold surfaces greatly improves the vacuum in the trap, preserving the HCIs in their high charge states for longer due to fewer charge exchange collisions with residual gas.

Then in 1986 the first EBIT was built, known as EBIT-I, developed by Levine and Marrs at the Lawrence Livermore National Laboratory (LLNL) in the USA [Levine et al., 1988]. Rather than being specialized for ion beam extraction, as the EBIS, the purpose of the EBIT was to produce HCIs and then investigate them in the trap itself. Thus although both devices have many common features and their basic operation is the same, an EBIT is a more compact system optimized for spectroscopy. The EBIT is also capable of producing considerably higher charge states than its predecessor. This is due to its much shorter trap, which is of the order of a few centimetres compared with ~ 1 m for an EBIS.

The shorter trap of the EBIT allows for a more stable electron beam. This in turn reduces the plasma instabilities, encountered in longer devices, that led to ion heating and thus limit the charge states attainable [Levine et al., 1985]. Detection of the photons emitted as a result of HCI interactions in an EBIT is made possible by the presence of multiple observation ports around the trap region, between the two elements of the Helmholtz coil which form the superconducting magnet. This contrasts with the EBIS setup, where the trap cannot be viewed from the side due to the single solenoid magnet used.

Initial experiments with EBIT-I were aimed at high resolution x-ray spectroscopy [Levine et al., 1989] and included the first cross section measurements for electron impact excitation and dielectronic recombination of HCIs [Marrs et al., 1988; Knapp et al., 1989]. Previous investigations of this type had been limited to lower charge states in crossed and merged beam experiments.

The importance of an EBIT, as an alternative to accelerators, in the field of HCI research quickly became clear and by 1990 projects to install duplicate devices at the Clarendon Laboratory in Oxford, England [Silver et al., 1994] and the National Institute of Standards and Technology (NIST) in Gaithersburg in the USA [Gillaspy, 1997] had begun.

The main advantage for spectroscopy with an EBIT over a conventional accelerator is the near absence of Doppler broadening, since the ions in the trap are effectively at rest. An EBIT is also a lot cheaper to build than an accelerator and it is of course much smaller.

In order to probe the radiation emitted in other regions of the electromagnetic spectrum further spectrometers can be positioned around the trap and contemporary EBITs are often equipped with a whole suite of instruments covering the range of photon energies from the visible to the hard x-ray regime. This has made extensive spectroscopic studies on the HCIs in the trap possible including measurements of excitation energies, the identification of line emissions and the determination of radiative lifetimes [Gillaspy, 1996; Beiersdorfer et al., 1996b, 2001a].

The first extraction of beams of HCIs from an EBIT was demonstrated in 1990 [Schneider et al., 1990]. Hence in addition to its status as an ion trap for experiments with HCIs *in situ*, the EBIT was established as a source of very low emittance beams of slow HCIs. The ability to extract HCIs opened up a whole new range of research possibilities with the EBIT, the most significant being atomic collision experiments with external targets using heavy ions in the highest of charge states.

Extraction onto a gas target enables the study of HCI-gas interactions independent of the electron beam under more defined conditions than in the trap [Tawara et al., 2003]. In the case of a solid target, HCI-surface interactions can be studied, which is simply not possible in the trap. Extensive studies using beams of HCIs extracted onto solid targets have been carried out and investigations include energy deposition, electron emission, sputtering, surface modifications, x-ray fluorescence and hollow atoms. A review can be found in [Schenkel et al., 1999].

To crown the list of EBIT achievements the device has been used to generate HCIs up to U^{92+} , the fully stripped ion of the heaviest naturally occurring element. This was first demonstrated in 1994 by Marrs *et al.* [Marrs et al., 1994] using a high voltage upgrade to EBIT-I [Knapp et al., 1993]. The so-called Super EBIT has heralded an important step for Doppler-free spectroscopic QED measurements of high- Z elements [Marrs et al., 1995]. (Previously such highly ionized species could only be formed using stripping techniques on relativistic accelerator beams.) Its ability to produce the highest ion charge states has greatly exceeded that of any EBIS or standard EBIT and has allowed the first direct measurements of the ionization cross sections for the formation of $U^{91+,92+}$ [Marrs et al., 1994]. In 1996 the Super EBIT extraction beamline was upgraded enabling study of the effects of its HCIs on external targets. X-ray measurements of the interaction of extracted beams with solid targets showed evidence of ions up to U^{90+} [McDonald et al., 2002]. With improvements in the ion transport efficiency, extraction experiments with $U^{91+,92+}$ ions could also be possible.

2.2 The EBIT device

2.2.1 Mode of operation

A schematic diagram showing the main components of a ‘standard’ EBIT, such as those used in this work, is presented in Figure 2.1. Of central importance is the electron beam. It follows the axis of the device and is formed at the base, at ground potential, by thermionic emission from the heated barium-doped tungsten cathode of a Pierce-type electron gun. The convex spherical surface of the cathode together with the focus electrode, which compensates for edge effects, ensure a converging electron beam. Magnetic compression of the electron beam reaches a theoretical maximum for laminar electron flow, therefore a zero field environment at the cathode is required [Hermann, 1958]. Consequently the electron gun is shielded by soft iron. For optimum beam conditions, however, it is in practice necessary to adjust the magnetic field at the cathode in order to minimize electron loss. This is achieved with the bucking coil. The electrons are accelerated away from the cathode by the anode using a bias of 2 to 5 kV, depending on the beam current required. They are then guided by the transition electrode through a small hole in the liquid nitrogen shield. Electron beam currents of up to 150 mA are routinely used.

Next the electron beam enters the main chamber. It is accelerated to its full interaction energy by the high voltage on the drift tube assembly in the trap region, which will be described in detail shortly. Generally an acceleration potential of up to 30 kV is employed. The acceleration potential of Super EBITs can reach 300 kV. Beam steering, to compensate for small mechanical misalignments, is achieved with four magnetic coils situated outside the vacuum system.

After the electron beam has passed through the trap region it is decelerated and removed by the collector electrode, which is typically biased at a potential of 1.5 kV. An electromagnet surrounding the collector helps to diverge the electron beam so that it is deposited over a large surface area and the heat generated is dissipated by a liquid nitrogen reservoir. Secondary electrons are prevented from being accelerated back into the trap by the suppressor electrode, located just below the collector. At the top of the collector, protruding slightly into it, is a negatively biased cone. This is the

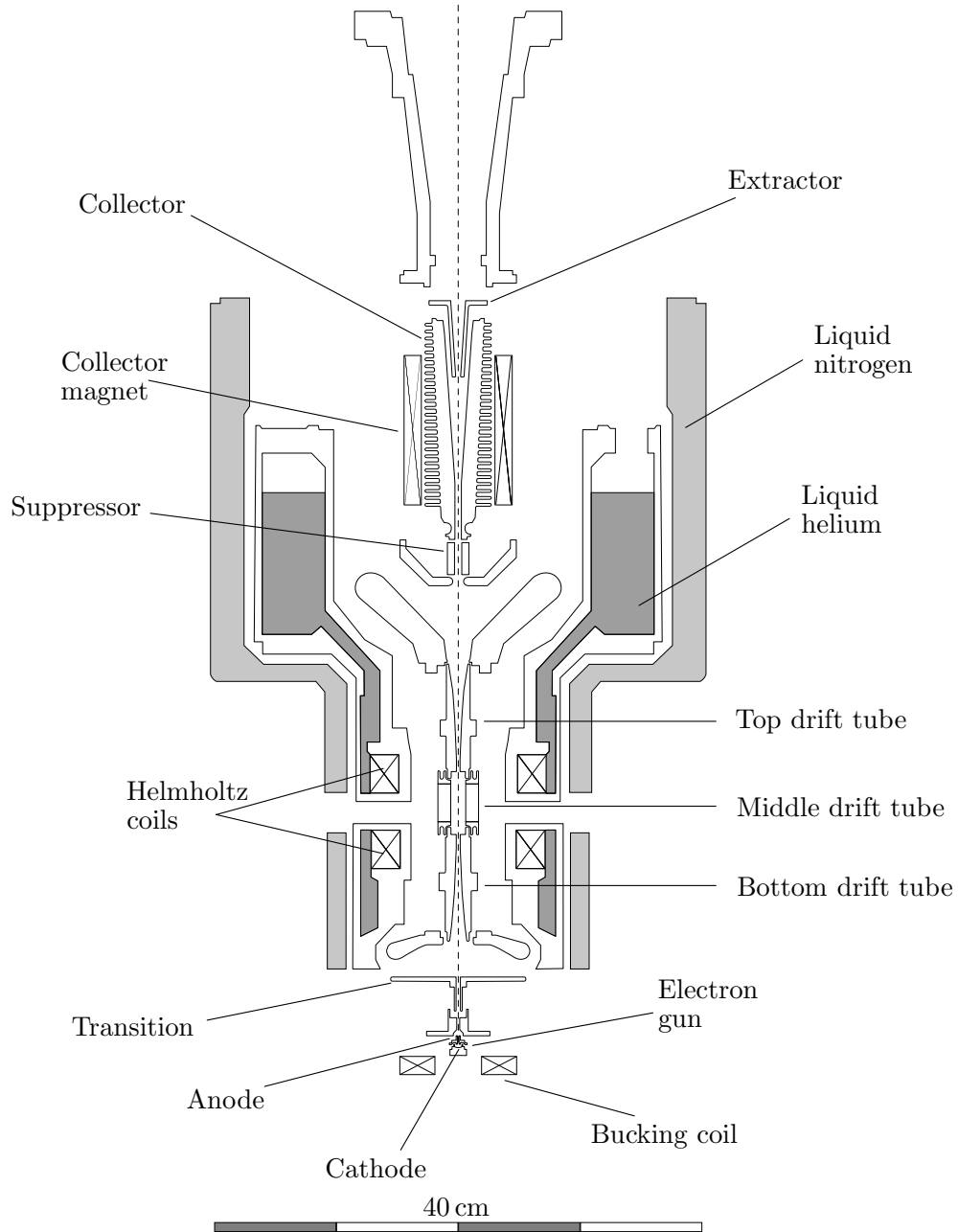


Figure 2.1: Schematic diagram of an EBIT.

extractor electrode and helps to guide ions out of the EBIT. It also prevents secondary electrons from escaping through the top of the trap.

For the production of the HCIs there needs to be a species in the trap which the electron beam can ionize. If the HCI precursor is a gas, e.g. argon or xenon as in the experiments conducted here, it can be introduced using a two stage, differentially pumped gas injector. This is installed at the side of the EBIT and incorporates a pair of collimating apertures. Gas at a pressure of 1 Pa is let into the first cavity, which is pumped to 10^{-3} Pa, and then into the second, which can be pumped down to 10^{-7} Pa. From there the gas can pass into the trap region to radially intersect the electron beam. The same setup can also be used in combination with an oven into which either a volatile compound or a metal with a high vapour pressure can be placed. A further technique for metallic ions is to use a device creating a metal vapour vacuum arc, known as a MEVVA [Brown, 1989]. This is mounted over the top of the EBIT chamber for injection along the trap axis. For barium and tungsten ions there is also the option to rely on their presence in the trap due to the vaporization of these elements from the cathode of the electron gun. These background levels are, however, low compared with the yields achieved with other techniques.

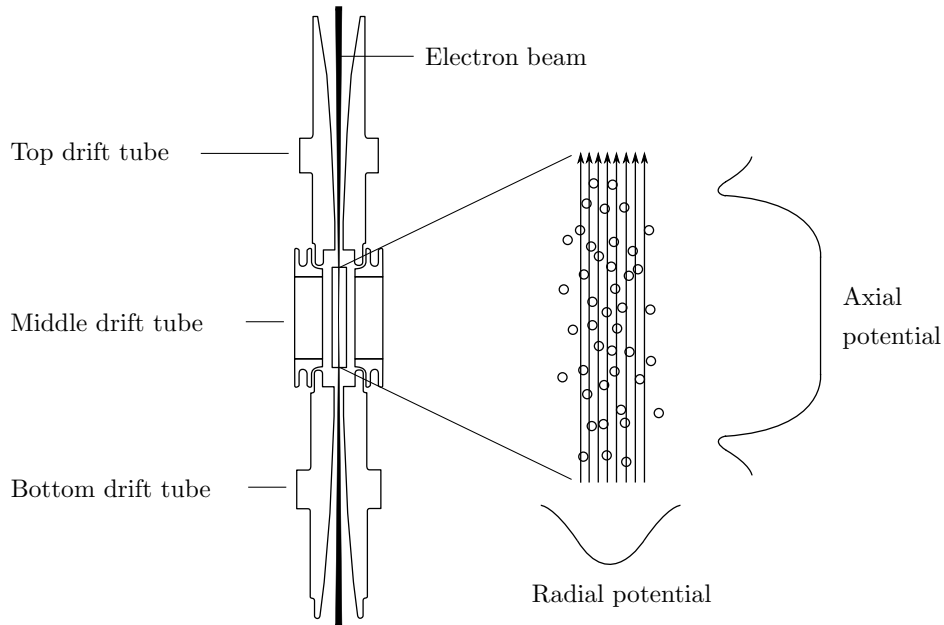


Figure 2.2: Schematic showing ion confinement in the trap region of an EBIT.

To ensure that very high charge states can be produced the ions need to be confined, otherwise they would escape the electron beam and avoid further ionization. Hence the ‘trap’ which is an inherent part of an EBIT. Ion confinement is accomplished by a combination of axial and radial trapping potentials, as illustrated in a detail of the trap region shown in Figure 2.2.

Radial trapping is primarily due to the space charge potential of the electron beam, which is highly compressed in order to maximize the rate of electron impact ionization collisions. The compression is achieved by the 3 T magnetic field generated by a pair of Helmholtz coils surrounding the drift tube assembly. These are cooled to around 4 K by a liquid helium cryostat, which is enveloped in a liquid nitrogen shield to minimize the amount of liquid helium required. As a result the diameter of the electron beam, measured elsewhere using an x-ray imaging technique [Levine et al., 1989], is reduced down to $\sim 70 \mu\text{m}$ (about the width of a human hair). This gives an electron beam density of the order of 10^{12} cm^{-3} .

The electron beam potential, V_e , as a function of radial distance, ρ , can be calculated to a good approximation by assuming that the charge distribution of the electron beam is homogenous. For a beam of radius r_e this gives:

$$V_e(\rho) = \frac{I_e}{4\pi\epsilon_0 v_e} \begin{cases} \left(\frac{\rho}{r_e}\right)^2 & \text{for } \rho < r_e, \\ \left(2 \ln\left(\frac{\rho}{r_e}\right) + 1\right) & \text{for } \rho \geq r_e, \end{cases} \quad (2.1)$$

with electron beam current I_e , electron velocity v_e and the permittivity of free space ϵ_0 . Beam energies are to a good approximation normally non-relativistic, with the exception of the Super EBIT. Hence calculating the electron velocity from an acceleration potential of $V_a = 10 \text{ kV}$, using $v_e = \sqrt{2eV_a/m_e}$, where e and m_e are the electron charge and mass, respectively, and using a beam current of $I_e = 100 \text{ mA}$, the potential V_e at the edge of the beam ($\rho = r_e = 35 \mu\text{m}$) takes a value of $\sim 15 \text{ V}$.

The electron beam space charge potential is, however, partially compensated by the space charge potential of the ions in the trap. This can be written as the sum of the ion potentials V_i , over all ions. In addition, the magnetic field produced by the Helmholtz coils acts to radially confine the ions. From the Lagrangian equation of motion an effective radial trapping potential can be obtained as:

$$V_{rad}(\rho) = V_e(\rho) + \sum_i \left(V_i(\rho) + \frac{eq_i B^2 \rho^2}{8m_i} \right), \quad (2.2)$$

with ion charge state q_i , ion mass m_i and magnetic field strength B . Solving for V_{rad} can only be performed numerically, as V_i depends on the ion distribution, which is in turn also a function of V_{rad} .

Axial trapping is achieved by a potential well determined by the voltages selected for three cylindrical copper drift tubes, named ‘top’, ‘middle’ and ‘bottom’. The outer tubes are biased more positively than the central one so that the ions are continuously reflected between the top and bottom, giving a trap length of ~ 4 cm. Typically, the potentials are selected to give an applied well depth of $V_{trap}=100$ to 300 V. The bias on the top tube is selected to be lower than that on the bottom in order to safeguard the electron gun from sputtering by the ions. Thus it is the shallower side of the well which determines the trap depth. When calculating the overall axial trapping potential, V_{ax} , however, a correction due to the image charge potentials of the electron beam on the drift tube walls has to be taken into account. These potentials depend on the tube radii. The inner radius of the central drift tube is larger than that of the outer tubes so that a trapping potential is created even before a voltage offset is applied. When the trap is loaded the image charge potential on the central tube is reduced as a result of space charge compensation of the electron beam by the ions. Combining the above, the total axial trapping potential can be written as:

$$V_{ax} = V_{trap} + (1 - f_{comp}) V_e(r_{middle}) - V_e(r_{top}), \quad (2.3)$$

where r_{middle} is the inner radius of the central, or middle drift tube, r_{top} is the minimum inner radius of the top drift tube, V_e is the electron beam potential given by Equation 2.1 and f_{comp} is the space charge compensation factor due to the ions in the trap. In depth discussion of the trapping potentials in an EBIT can be found in [Fussmann et al., 1999; Currell, 1999].

Spectroscopic investigations of the trap inventory are made possible by slits machined into the middle drift tube, which face ports in the chamber wall. There are typically eight slits, one of which is reserved for the gas injector leaving the others free for direct radial access of a range of spectrometers to the trap.

The vacuum requirements of an EBIT are very high, as any background gas in the trap presents a route for the HCIs to regain electrons via charge exchange collisions. Continuous pumping by turbomolecular and ion pumps together with meticulous cleanliness achieve a vacuum of 10^{-7} Pa. The cathode of the electron gun is very sensitive to oxidation and is therefore separated from the main chamber by a small opening and pumped by its own ion pump.

When the EBIT is in operation there is also efficient cryopumping in the trap region by the drift tube surfaces, as these are in thermal contact with the liquid helium cooling the superconducting Helmholtz coils. This extra pumping gives rise to a vacuum which can no longer be measured by the gauges in the chamber, as these have a lower limit of 10^{-8} Pa and moreover do not access the space within the drift tubes where the vacuum is the highest. However, estimates such as those based on comparing the charge state distributions of extracted ions with those obtained from numerical simulations indicate that in the trap region a vacuum of the order of 10^{-9} Pa is reached [Schneider et al., 1991].

2.2.2 EBITs used in this work

Three EBIT facilities were used for the experimental work presented in this thesis, the first in Berlin, Germany, and the second and third in Berkeley, California in the USA.

The EBIT in Berlin has been in operation since 1996. It was installed at the Max Planck Institute for Plasma Physics, primarily to investigate HCI processes relevant to thermonuclear fusion [Biedermann et al., 1997]. Then in 2001 an extraction beamline incorporating a gas target was added, furthering the research capabilities of the device. In 2003 the EBIT and its extraction system were moved to their current location at the Humboldt University of Berlin.

In Berkeley, the two EBITs used were the so-called EBIT-II and a Refrigerated EBIT (REBIT). EBIT-II is the second EBIT to have been built at LLNL and was relocated to LBNL in 2000. Research with EBIT-II concentrates on phenomena arising when HCIs are extracted onto solid targets [Schenkel et al., 2002]. The REBIT is a novel device designed for ion beam extraction, built by J.W. McDonald and D.H.G. Schneider [McDonald and Schneider, 2005]. It uses a closed cycle cryogenic refrigerator system to cool the superconducting magnet. This circumvents expensive liquid gas cooling from external sources. The new cooling system also has the advantage that once set up for a given measurement, the REBIT can be left in unsupervised operation, which is a great asset for experiments requiring very long data acquisition times.

2.3 Interaction processes in the trap

A plethora of interactions takes place between the electrons, atoms and ions in an EBIT. First and foremost is the generation of HCIs with the electron beam, via successive electron impact ionization of the precursor species injected into the trap. However, several other inelastic collisions also occur. These result in the emission of radiation which can be measured. The dominant source of this emission is direct electron impact excitation. Further radiative collisions, which involve the removal of electrons and hence play a role in determining the ionization balance in the trap, are electron-ion recombination processes and charge exchange between HCIs and residual gas neutrals. Elastic electron-ion and ion-ion collisions are central to energy exchange in the EBIT, with those HCIs gaining sufficient kinetic energy escaping the trap. As a result the remaining ion ensemble is cooled, which also affects the ionization balance attained.

In this section the process of ionization by the electron beam and the radiative interactions to which the HCIs then succumb are discussed. Elastic collisions are considered in Section 2.4, in the context of the evolution of ions in the trap.

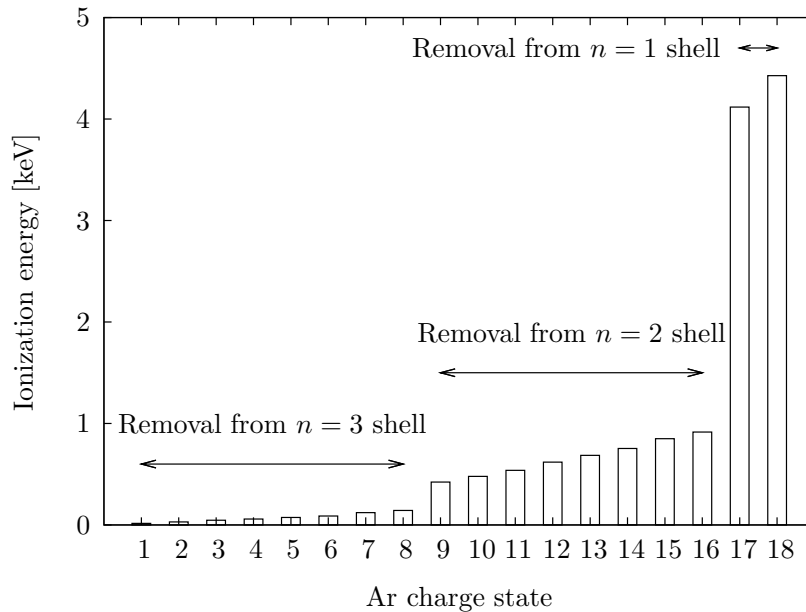


Figure 2.3: Ionization energies for the formation of Ar^+ to Ar^{18+} [Dyall et al., 1989].

2.3.1 Electron impact ionization

Ionization occurs when an incident electron transfers enough kinetic energy to a bound electron for it to be ejected from the atom or ion concerned. Specifically, the removal can only take place when the beam electron carries an energy into the collision which is greater than or equal to the binding energy of the electron in the target. Successive ionization impacts then result in the generation of HCIs. This is illustrated by Figure 2.3 which shows a plot of the charge states of argon versus the ionization energy for their production, calculated using the GRASP code [Dyall et al., 1989]. Energies range from 16 eV for the creation of Ar^+ to 4.4 keV for the creation of Ar^{18+} . The energy gaps between quantum shells give rise to the steps seen in the figure, with progressively greater amounts of energy being needed to remove electrons bound more tightly to the nucleus. In an EBIT the maximum charge state of a particular ion species in the trap is thus determined by the energy selected for the electron beam.

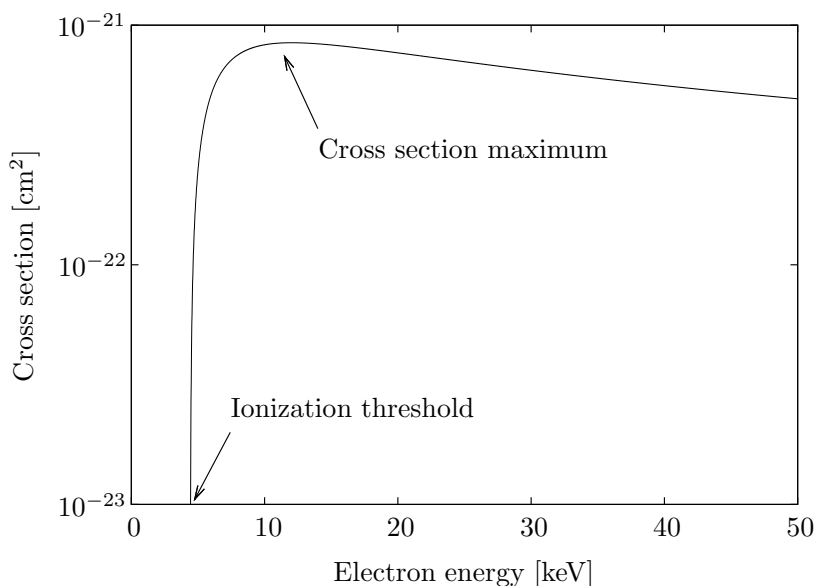


Figure 2.4: Electron impact ionization cross sections for the formation of Ar^{18+} versus electron energy [Lotz, 1968].

The cross sections for electron impact ionization are widely calculated using the semi-empirical Lotz formula [Lotz, 1968] and depend on the electron beam energy, the ionization potential of the electron to be removed and

the ion's particular electronic configuration. The formula allows the general trend over a large range of electron energies to be obtained. Figure 2.4 shows the result for the formation of Ar^{18+} by electron impact ionization of Ar^{17+} ions. It can be seen that the cross section peaks at an electron energy of ~ 10 keV, which is approximately twice the ionization energy. This relationship generally holds for all HCIs. As a result, to maximize the yield of a particular ion in an EBIT the electron beam energy is typically set a factor of two higher than the ionization energy required for its creation.

2.3.2 Radiative collisions

As previously mentioned, the dominant radiative process occurring in the trap is direct electron impact excitation of the HCIs. This is related to impact ionization, although rather than an electron being ejected into the continuum it is promoted to a higher bound state. The excited system then decays by the refilling of the electron hole accompanied by the emission of a photon.

Further radiative interactions involve the capture of beam electrons by HCIs. If the excited state does not auto-ionize then a reduction in the charge on the ion results. One scenario is radiative recombination, by which an electron is captured into a certain energy level of the ion and then on relaxation a photon is emitted with an energy equal to the sum of the kinetic energy of the beam electron and the binding energy of the capture state. Essentially this is the time-reversal of the photoelectric effect. The cross sections for radiative recombination are typically one or two orders of magnitude lower than those for electron impact ionization. For example, the ionization cross section for 10 keV electrons impacting on Ar^{17+} ions is 10^{-21} cm^2 , as demonstrated in Figure 2.4. The corresponding cross section for radiative recombination is of the order of 10^{-23} cm^2 [Kim and Pratt, 1983].

At resonant beam energies an alternative process called dielectronic recombination can occur. This involves the simultaneous excitation of a second electron giving rise to a doubly excited state which then also decays. The resonance condition is that the energy of the incoming electron must equal the transition energy of the excitation. In this work, however, this resonance was not sought.

In the collisions of HCIs with neutrals, electron capture proceeds into Rydberg states of the HCI, resulting in radiative cascades to the ground state. This is the process of charge exchange, the key interaction investigated in this

thesis, and is described in more detail in Chapter 4. The cross sections for charge exchange are relatively large. For example for $\text{Ar}^{17+,18+}$ ions they are of the order of 10^{-14} cm^2 [Müller and Salzborn, 1977]. Hence when it comes to preserving HCIs in their high charge states the presence of background gas in the trap is an interference. This explains why ultra high vacuum conditions are needed in the EBIT. It has been found, however, that the injection of small amounts of a low mass neutral gas significantly increases the yield of the highest charge states in an EBIT. This is due to evaporative cooling, which is described in the following section.

2.4 Charge and temperature evolution in the trap

The generation of the highest charge states in an EBIT can take of the order of seconds and the charge state equilibrium reached for a particular species is determined by a variety of competing processes. On the one hand, successive electron impact ionization of the injected species increases the charge of the ions, while on the other, the processes of radiative recombination with beam electrons and charge exchange with residual gas act to lower it. Furthermore, there is axial and radial escape of ions from the trap. In order to estimate the number of ions which can finally be trapped in an EBIT one can, as a first approximation, assume that the electron charge in the trap region becomes completely compensated by that of the ions. The space charge of the electron beam, Q_e , is derived from the electron beam current I_e , trap length l and electron velocity v_e , as follows:

$$Q_e = -I_e \frac{l}{v_e}, \quad (2.4)$$

where the electron velocity can again be obtained non-relativistically using $v_e = \sqrt{2eV_a/m_e}$. For $I_e=100 \text{ mA}$, $l=4 \text{ cm}$ and $V_a=10 \text{ keV}$, Equation 2.4 gives $Q_e \approx 10^8 e$, in units of electron charge. Due to the fact that there is a distribution of ion charge states in the trap, this translates to a trapping capacity of the order of 10^6 HCIs per charge state. In reality, however, it is presumed that complete neutralization of the electron beam charge will not occur. This is because as the fraction of ions increases the radial trapping potential becomes progressively weaker due to space charge compensation (see Equation 2.2).

The energy balance of the trapped ions is also determined by a range of processes. These are electron beam heating, elastic ion-ion collisions and cooling as a result of ion escape. Following the model introduced by Penetrante *et al.*, the number, N_i , and temperature, T_i , evolution of ions of charge state i in the trap can be calculated from the following set of coupled rate equations [Penetrante et al., 1991]:

$$\begin{aligned}
 \frac{dN_i}{dt} = & R_i^{inj} && \text{Species injection} \\
 & + R_{i-1 \rightarrow i}^{EI} - R_{i \rightarrow i+1}^{EI} && \text{Electron impact ionization} \\
 & + R_{i+1 \rightarrow i}^{RR} - R_{i \rightarrow i-1}^{RR} && \text{Radiative recombination} \\
 & + R_{i+1 \rightarrow i}^{CX} - R_{i \rightarrow i-1}^{CX} && \text{Charge exchange} \\
 & - R_i^{esc} && \text{Ion escape}
 \end{aligned} \tag{2.5}$$

$$\begin{aligned}
 \frac{d}{dt} (N_i k T_i) = & \frac{d}{dt} (N_i k T_i)^{beam} && \text{Electron beam heating} \\
 & + \frac{d}{dt} (N_i k T_i)^{exc} && \text{Ion-ion energy exchange} \\
 & - \frac{d}{dt} (N_i k T_i)^{esc} && \text{Cooling via ion escape.}
 \end{aligned} \tag{2.6}$$

The various terms for the number evolution appear with their respective rates, R , with the appropriate super- and subscripts. For the temperature evolution the energy distribution is assumed to be Maxwellian, which is valid to a good approximation; k is the Boltzmann constant.

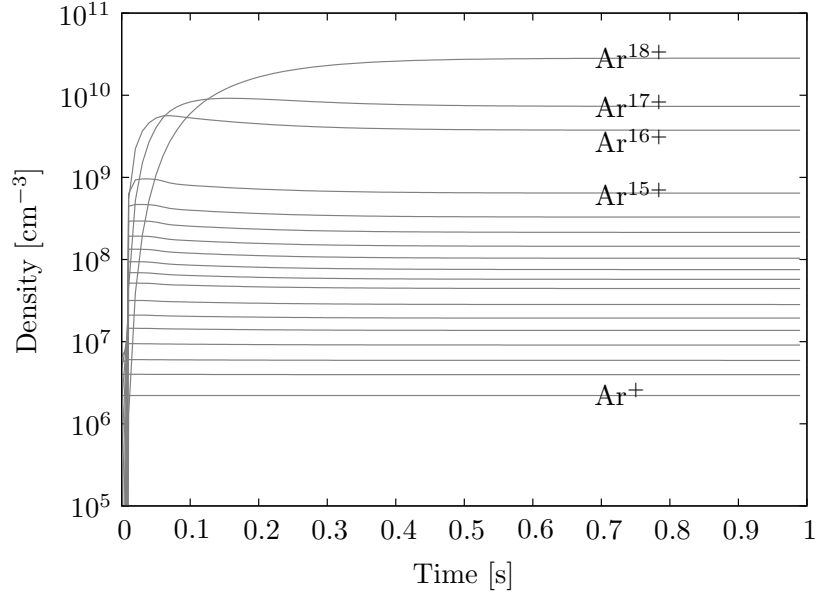
Each contribution from electron impact ionization, radiative recombination and charge exchange in Equation 2.5 consists of a pair of terms. In the former process an ion of charge state i is formed by ionization and can then itself be ionized and thereby removed, whereas in the latter two processes an ion of charge state i is formed after electron capture and can then be eliminated by the further capture of an electron. Double and higher order electron impact ionization and charge exchange do not play a significant role in the charge state evolution as they have cross sections which are generally at least an order of magnitude lower than their single counterparts. The cross sections for dielectronic recombination are, in contrast, relatively high. However, since this is a resonant process, averaging its cross sections over the velocity distribution of ions in the trap gives negligible values. Ion-ion

charge exchange is neglected due to the low ion temperatures in the trap, which prevent the Coulomb barrier for this interaction from being overcome. The final term in Equation 2.5 refers to ion escape from the trap, which can occur axially and radially, and is dependent on ion temperature. Usually the rate of radial escape is much lower than that for axial escape, unless the trap is very deep and the space charge compensation of the ion beam has become very large.

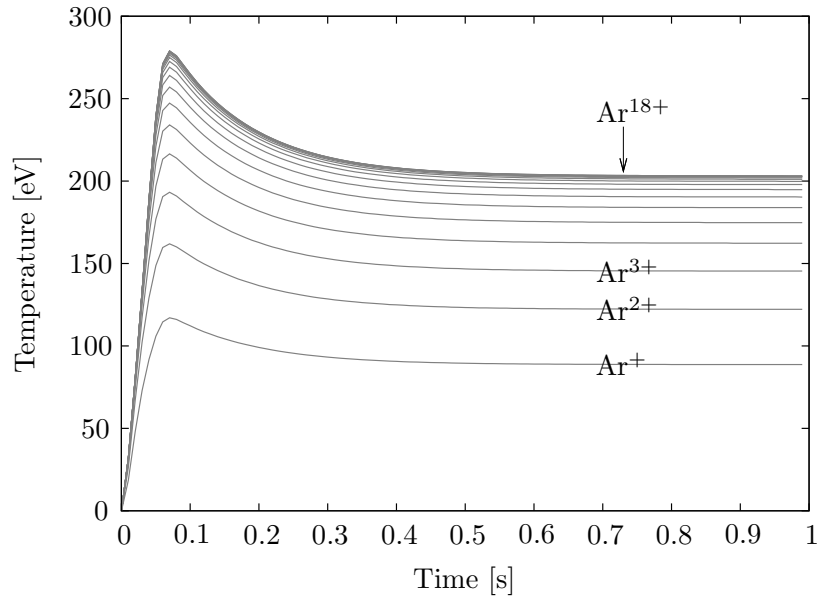
Moving on to Equation 2.6, the first term corresponds to electron beam heating and describes the elastic long range Coulomb collisions between energetic electrons and the trapped HCIs. It has a quadratic dependence on ion charge, thus the highest charge state ions become the hottest. The term for ion-ion energy exchange refers to the long range Coulomb collisions between the trapped HCIs. The collision times for encounters between the highest charge states are the shortest. As a result, these states exchange energy the fastest and so equilibrate at similar temperatures. Cooling via ion escape, given by the final term, arises when sufficiently energetic ions leave the trap. Ions in lower charge states escape the most readily, leaving behind the high charge state ions, which equilibrate their temperatures via ion-ion collisions. This phenomenon is called evaporative cooling [Levine et al., 1988, 1989]. In order to enable the generation of the highest charge states of heavy elements evaporative cooling is deliberately enhanced by the continuous injection of a low mass gas into the trap.

In depth discussion of the coupled rate equations just introduced can be found in [Currell, 2003; Currell and Fussmann, 2005]. For the purposes of the overview presented here, the results of a numerical simulation for argon ions based on Equations 2.5(a) and 2.5(b) are presented. The simulation was performed using a code developed in the Berlin EBIT group. Figures 2.5(a) and 2.5(b) show the data obtained for ion density and temperature, respectively, versus breeding time. The code inputs include the density of neutrals injected for ionization, the physical dimensions of the trap and atomic physics data. Theoretical cross sections are assumed. The electron beam current, acceleration potential and axially applied trapping potential were set to 120 mA, 10.1 kV and 100 V, respectively.

Comparing the two figures it is observed that the ion density curves rise much more steeply than those for ion temperature. This reflects the very fast rate at which ionization occurs. Focusing on the density plot, it can be seen that the final densities reached after 1 s of breeding rise with increasing ion charge state. This confirms the suitability of an EBIT for the generation of



(a) Charge state evolution



(b) Temperature evolution

Figure 2.5: Numerical simulation for the evolution of charge state and temperature of argon ions in an EBIT over 1 s. $I_e = 120$ mA, $V_a = 10.1$ kV and $V_{trap} = 100$ V.

ions in the highest of charge states. For Ar^+ to Ar^{17+} ions the density maxima are reached within 0.1 s, after which their numbers are depleted due to further ionization before they finally equilibrate. In contrast, the density of Ar^{18+} ions increases continuously to a plateau. The temperature plot demonstrates a rapid monotonic increase in ion temperature after which the temperatures decrease, due to ion escape. Finally the temperatures equilibrate, via ion-ion collisions. The highest charge states reach the highest temperatures and share their energy the most effectively, as described.

Chapter 3

Experimental

In order to conduct the studies of electron capture by HCIs presented in this thesis, a series of experiments was designed. The investigations of electron capture from gases were carried out at the Berlin EBIT by using HCIs interacting with residual gas in the trap and by extracting beams of HCIs onto a gas target. The investigations of electron capture from surfaces were carried out at the two EBIT facilities in Berkeley, using beams of HCIs extracted onto solid targets.

This chapter first describes the in-trap HCI-gas interaction experiments which were implemented using an EBIT in magnetic trapping mode. There the emission of K -shell x-rays resulting from electron capture into bare and hydrogenic ions was studied. Next the methods of extracting HCIs from an EBIT are introduced, accompanied by descriptions of the main beamline components. The details of the experiments using beams of HCIs incident on gaseous and solid targets are then given. In the studies implementing an external gas target, the x-ray emission measurements carried out in the trap were extended in order to investigate the effect of collision energy on the electron capture state. This was achieved by using a setup to decelerate the extracted ions. The investigations with solid targets concentrated on quantifying the amount of charge exchange taking place when HCIs interact with surfaces. For this purpose special targets were prepared and the fabrication techniques of these targets are also described.

3.1 The EBIT in magnetic trapping mode

3.1.1 Principles of magnetic trapping

In addition to the standard mode of operation described in Section 2.2, the EBIT can be operated in several other modes depending on the particular investigation in mind. For the in-trap investigations presented here, the operation technique chosen was to switch the electron beam on and off in a cycle. This method was first introduced by Beiersdorfer *et al.* [Beiersdorfer et al., 1996d]. During the time when the electron beam is on, the EBIT operates in the normal way: HCIs are created, trapped and excited. This part of the cycle is known as the electron beam mode (EBM). However, once the electron beam is switched off, the device effectively becomes a Penning trap. Axially the ions are still trapped by the potentials on the drift tubes, but radially there is only trapping by the magnetic field of the Helmholtz coils, i.e. trapping by the space charge of the electron beam no longer occurs. The part of the cycle when the electron beam is off is thus called the magnetic trapping mode (MTM).

It may not immediately be clear what could be gained by turning off the electron beam and thus compromising an EBIT's ability to produce and confine HCIs. However, the presence of HCIs in the trap in the absence of the electron beam enables a range of new EBIT experiments. For example, mass spectrometry of the HCIs created in EBM becomes possible via Fourier transform ion cyclotron resonance [Beiersdorfer et al., 1996a]. This technique involves the insertion of electrodes through observation ports in the middle drift tube to excite and detect the ions' cyclotron motion, which is not possible in the presence of the electron beam because its electric field strongly modifies the ion orbits. Another research area is the measurement of atomic lifetimes for electric dipole-forbidden transitions [Crespo López-Urrutia et al., 1998]. This is based on the fact that all excitation ceases once the electron beam is switched off, allowing the temporal evolution of the emission from a particular decay to be tracked without collisional perturbations.

With the aim of studying x-ray emission following electron capture by trapped HCIs from neutrals, MTM is the method of choice because in the absence of the electron beam, charge exchange becomes the exclusive x-ray production mechanism. This is in stark contrast to the situation during EBM, where the radiation emitted as a result of charge exchange is masked by that from electron impact excitation. Due to the fact that the trap depth

limits the kinetic energy of the ions, the *in situ* experiments involve HCIs in a given relatively narrow energy regime. Estimates of the kinetic energy of the HCIs in the MTM experiments are given in Section 5.1.1.

3.1.2 The magnetic trapping experiment

A cross section through the Berlin EBIT showing the experimental arrangement for the MTM experiments is presented in Figure 3.1. Gas was continuously injected into the trap using the gas injector, serving as the species to ionize during EBM and as a target for electron capture by the HCIs during MTM. The gas chosen was argon and it was supplied from the gas injector at a backing pressure of 10^{-5} Pa.

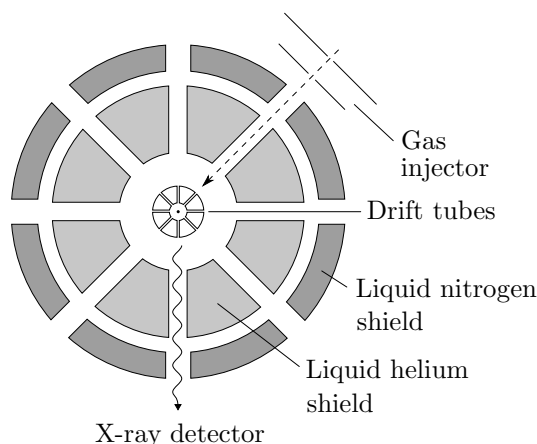


Figure 3.1: Cross section through the Berlin EBIT showing the gas injector and x-ray detector installed on radial observation ports.

The x-rays emitted as a result of HCI interactions in the trap were measured using a windowless solid state *Canberra GUL0035P* detector, which implements a liquid nitrogen-cooled germanium P-I-N photodiode with an active area of 30 mm^2 . It achieves a full width at half maximum (FWHM) peak resolution of 136 eV at 5.9 keV. The detector is mounted on a manipulator directed towards a $1.6 \times 40\text{ mm}$ slit in the middle drift tube, of which a length of 16 mm is visible, due to the smaller diameter opening in the cryogenic shield. In its regular position the detector head is at a distance of 200 mm from the trap axis, whereas for the magnetic trapping experiments it was moved in by 115 mm. In this way the solid angle for photon detection

was increased from $7.5 \cdot 10^{-4}$ sr to $4.2 \cdot 10^{-3}$ sr. The detector was calibrated using the K_α and K_β line emissions, between 3 and 4 keV, from impact excitation collisions of $\text{Ar}^{17+}, 18+$ ions with the electron beam. Theoretical values for the transition energies were taken from [Fritzsche, 2003]. From a linear fit to the calibration data a calibration accuracy of ± 25 eV is inferred.

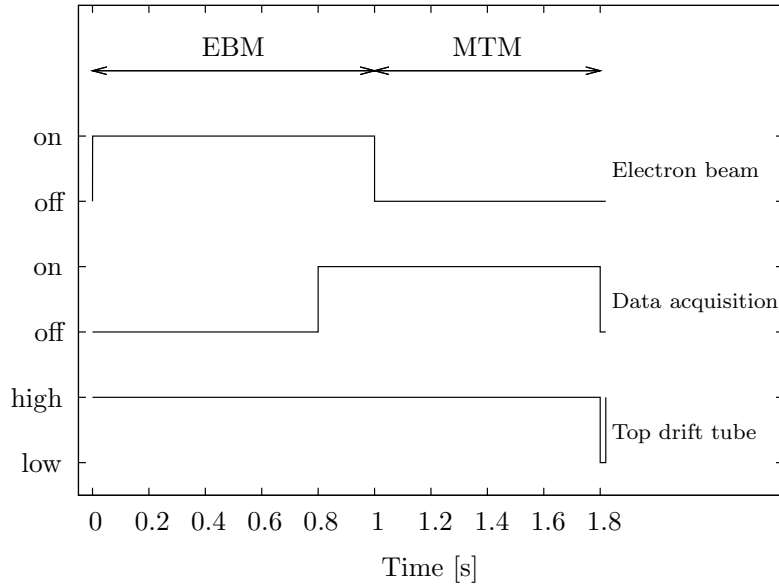


Figure 3.2: Timing pattern used for the magnetic trapping experiments. The switching of the electron beam and data acquisition system together with the brief lowering of the top drift tube potential at the end of a cycle are shown.

Rapid switching of the electron beam was achieved by controlling the anode voltage of the electron gun with a function generator in combination with a high voltage amplifier. In each switching cycle the electron beam was turned on to the required ionization potential, within 8 ms, to give 1 s of breeding after which it was turned off, within 4 ms, to give 0.8 s of magnetic trapping for the charge exchange experiment. Some experiments using MTM times of up to 20 s were also carried out. The x-rays emitted from the trap were recorded as a function of time, for the last 0.2 s of EBM (much more intense emission in this phase) and for the full duration of MTM. In this way the time evolution of x-ray emission in both modes was recorded. At the end of each cycle the ions remaining in the trap were expelled by lowering the potential on the top drift tube. This was done to avoid the accumulation of contaminating heavy ions, such as those of tungsten and barium from

the cathode of the electron gun. For a given measurement the cycle was repeated several thousand times. The timing pattern, regulated by the EBIT sequencer, is shown in Figure 3.2.

In order to investigate whether the axial trapping potential of the EBIT might affect the charge exchange emission spectra recorded, a selection of trap depths was employed using $V_{trap} = 30, 100$ and 700 V. The particular HCIs of interest were Ar^{17+} and Ar^{18+} . These were created using an electron beam current of 70 mA and 100 mA, respectively. For the experiments with Ar^{17+} ions the electron beam energy was set to 4.3 keV, just below the ionization potential for forming Ar^{18+} . In contrast, in the experiments investigating Ar^{18+} ions an electron beam energy of 10.1 keV was selected. This maximizes the yield of Ar^{18+} ions, as discussed in Section 2.3.1. The x-ray contributions from the Ar^{17+} ions inevitably also present are then subtracted out. The results of the magnetic trapping experiments are presented in Section 5.1.1.

3.2 Extraction of HCIs from an EBIT

3.2.1 Principles of extraction

There are two methods by which ions are extracted from an EBIT. One is called leaky mode and the other pulse mode. In leaky mode a continuous beam of HCIs is produced, comprising those ions with sufficient kinetic energy to escape from the trap over the axial potential barrier. This energy is gained through the process of collisional heating, mainly by the electron beam. In contrast, in pulse mode ion bunches are periodically ‘dumped’ into the extraction beamline after a given breeding time. This is typically achieved by ramping the potential of the middle drift tube up and over that of the top drift tube at the end of each pulse cycle. In both cases the ions are accelerated out of the trap to ground potential and the velocity, v , of the extraction ions is given by:

$$v \geq \sqrt{\frac{2eqV_{ext}}{m}}, \quad (3.1)$$

with ion charge state q and ion mass m . The inequality sign takes account of the kinetic energy distribution of the trapped ions. The extraction potential, V_{ext} , is determined by the base potential of the drift tube assembly plus the

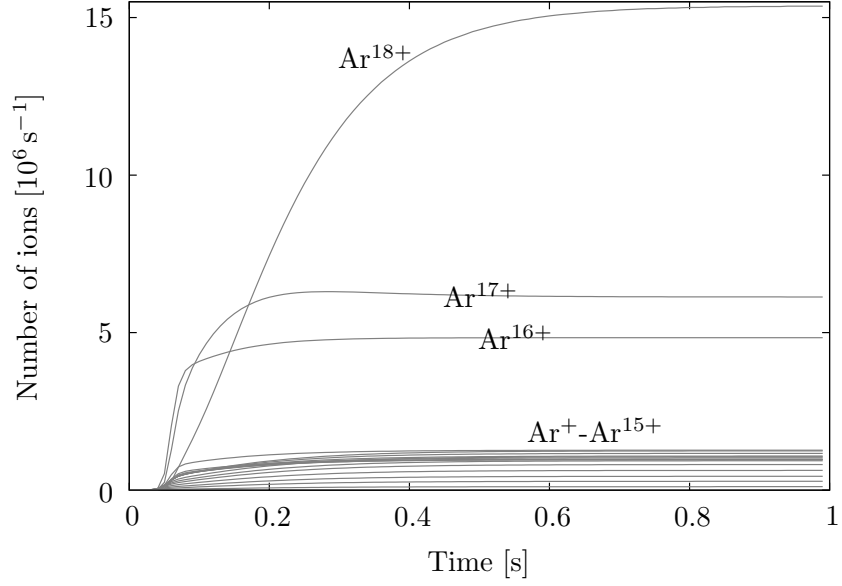
voltage selected for the top drift tube, i.e. $V_{ext} = V_{drift} + V_{top}$ and is modified by the electron beam and ion space charges in a similar way to that shown for the axial trapping potential in Equation 2.3. This correction is quantified in Section 3.2.3.

A comparison of the two extraction techniques is illustrated in Figure 3.3, calculated using the same numerical simulation described in Section 2.4. Figure 3.3(a) shows the escape rates of argon ions in leaky mode over 1 s and Figure 3.3(b) shows the rate at which argon ions are extracted in the ejection phase of a pulse mode cycle, after 0.9 s of breeding. The vertical dashed line in the second figure marks the time at which the space charge-compensated axial trapping potential reaches zero and thus all ions have been expelled. For both plots an ionization potential of 10.1 kV was defined. This maximizes the ionization cross section for the generation of Ar^{18+} ions, as previously mentioned. Accordingly, it can be seen that in both modes the extraction rates for the highest charge states reach the highest values. An advantage of pulse mode, however, is that the ionization potential does not have to equal the extraction potential, i.e. before raising the potential of the middle drift tube the base potential of the drift tube assembly can also be changed. In this way the extraction of HCIs at a lower potential than the ionization potential required for their creation becomes possible.

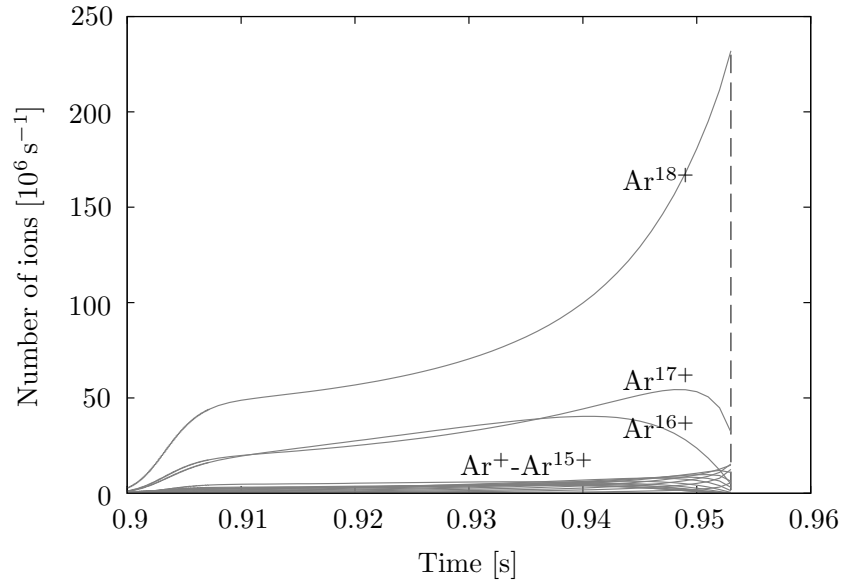
The extraction beamline, which the HCIs enter after expulsion through the top of the trap, is now described.

3.2.2 The EBIT extraction beamline

A beamline for the extraction of ions from an EBIT consists of a series of elements to steer, focus and collimate the ion beam, a device to separate and select charge states, and finally the setup for the particular investigation envisaged. A description of ion extraction from an EBIT in the context of the experiments carried out for this thesis is now given. This takes the form of a discussion of the various beamline elements, divided into three categories: Ion beam optics, charge state selection and ion beam diagnostics. Diagrams of the extraction beamlines used in this work are presented in Figures 3.6 and 3.10, to accompany the descriptions of the extraction experiments undertaken.



(a) Leaky mode



(b) Pulse mode

Figure 3.3: Numerical simulations for the extraction of argon ions from an EBIT in leaky and pulse mode. $I_e = 120$ mA, $V_a = 10.1$ kV and $V_{trap} = 100$ V.

Ion beam optics

For a maximum yield of extracted ions it is necessary to transport the beam efficiently through the beamline. Optimization actually starts within the trap itself, where the electron beam helps to focus and guide the ions to the extractor. The steering coils are very important here and even slight adjustments to the bucking coil at the electron gun can have large effects. Then there are several elements in the extraction beamline which are used to control the ion beam. Typically, one of the first of these elements is a 90° electrostatic bender, consisting of two oppositely biased, curved plates. This is used to deflect the ion beam out of the EBIT axis, which is often vertical, into the horizontal plane of the beamline.

After the bender (and sometimes also before it) a series of elements helps to transport the ion beam along the beamline to the experiment. To control the direction of the beam, electrostatic deflectors are in place. In principle parallel plates biased at opposing voltages would achieve the deflection, but it is more effective to use an arrangement of cylindrical electrodes, as this technique avoids fringe fields [Pikin et al., 1996]. One such deflector element consists of a cylinder which has been sliced diagonally to give two electrodes. In order to be able to deflect the beam in perpendicular planes, another cylinder with its slice rotated 90° with respect to the first is installed directly afterwards.

Focusing of the ion beam is achieved with Einzel and quadrupole lenses. An Einzel lens consists of three sequential cylindrical electrodes. The outer electrodes are typically grounded and the inner electrode is given a positive bias which can be tuned. In contrast, a quadrupole lens consists of four electrodes arranged radially, with alternate positive and negative biases, around a section of the beamline axis.

Collimation is achieved by moving slits into the beam or passing it through an aperture machined into a metal plate.

Charge state selection

In order to carry out experiments with specific ion charge states, the ions extracted from the trap are separated according to their mass-to-charge ratio. In EBIT beamlines it has become standard to achieve charge separation with a 90° sector magnet and this is the device used in Berkeley. The more recent extraction beamline at the Berlin EBIT was not initially equipped with such an element, but as part of this dissertation a Wien filter was added, which

also allows mass-to-charge separation. As opposed to the bender magnet, the Wien filter is a straight-line device. This means that its addition into an existing beamline involves less upheaval. The principle of operation of each device is now explained.

The sector magnet consists of two identical electromagnets placed in sandwich formation above and below a 90° bend in the beamline. A magnetic field perpendicular to the ion beam is generated, which exerts a force on the ions so as to guide them into the bend. Equating the forces experienced by the charged particle moving in a curved path of radius r and substituting for the velocity of the ions from Equation 3.1, the following relation for the magnetic field is obtained:

$$B = \frac{\sqrt{2V_{ext}}}{r} \sqrt{\frac{m}{eq}}. \quad (3.2)$$

Thus the magnetic field is proportional to the square root of the mass-to-charge ratio of the ions. For a given extraction potential and fixed radius of curvature, the magnetic field can be selected such that only ions with a certain mass-to-charge value are allowed to pass through a collimator positioned at the exit of the magnet setup. A typical magnet scan for xenon ions (isotopically pure ^{136}Xe) is shown in Figure 3.4. The scale on the x-axis shows the current passed through the magnet, to which the magnetic field is directly proportional. The count rate was recorded using a multi channel plate (MCP) detector installed at the end of the beamline. As can be seen from the figure, there were also ion species other than xenon present in the beam. These result from the ionization of residual gases in the EBIT. The trap is tuned to maximize only the yield of the particular ion species of interest, but background contaminants do aid the calibration of scans. In an experiment, however, an ion charge state which has the same mass-to-charge ratio as a contaminant ion is not usually selected.

The Wien filter makes use of an electric field, E , and a magnetic field, B , which are arranged perpendicular to one another so that ions passing through the arrangement experience the electric and magnetic forces in opposite directions. The E and B fields are chosen such that the resultant Lorentz force on the ions of a particular velocity is zero, i.e. these ions will pass through the filter undeflected. In this case the ion velocity is given by:

$$v = \frac{E}{B}. \quad (3.3)$$

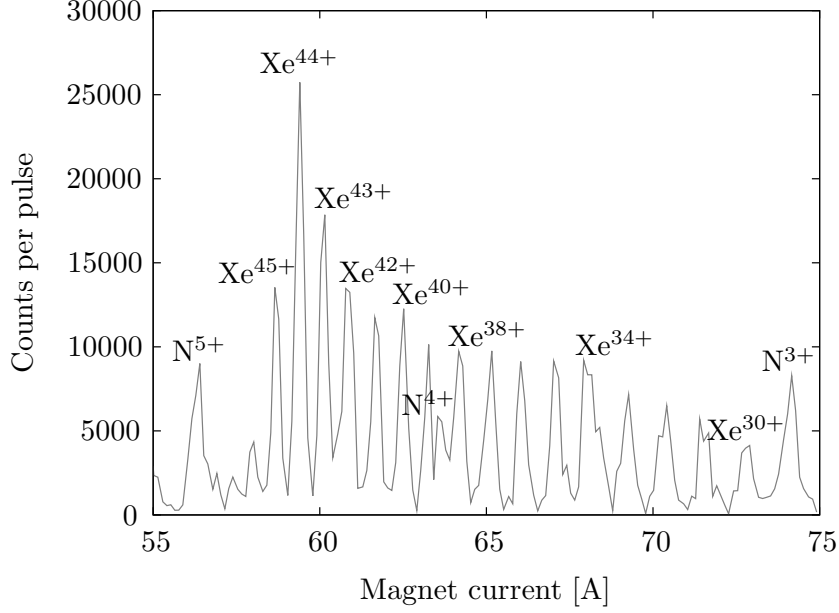


Figure 3.4: Magnet scan of the charge states of xenon ions extracted in pulse mode from the REBIT in Berkeley for a breeding time of 0.9 s. $I_e = 70$ mA, $V_a = 8.1$ kV, $V_{trap} = 100$ V and $V_{ext} = 9.2$ kV.

The device can be operated by keeping the electric field constant and varying the magnetic field or vice versa. Here the electric field was held constant and the magnetic field was scanned. Substituting Equation 3.1 into Equation 3.3, the following relation for the magnetic field is obtained:

$$B = \frac{E}{\sqrt{2V_{ext}}} \sqrt{\frac{m}{eq}}. \quad (3.4)$$

Hence, as with the sector magnet, the magnetic field is proportional to the square root of the mass-to-charge ratio of the ions. A typical Wien scan for argon ions is shown in Figure 3.5, again demonstrating the presence of contaminants in the beam. The electric field was maintained at 33.6 kVm^{-1} , which is the maximum value of the device, therefore enabling maximum separation of the different charge states. Note that the distribution of charge states depends strongly on the conditions in the trap, in particular on pressure. Consequently it is to be expected that ion beams extracted from different EBITs will have different charge state distributions, as the scans presented in Figures 3.4 and 3.5 demonstrate.

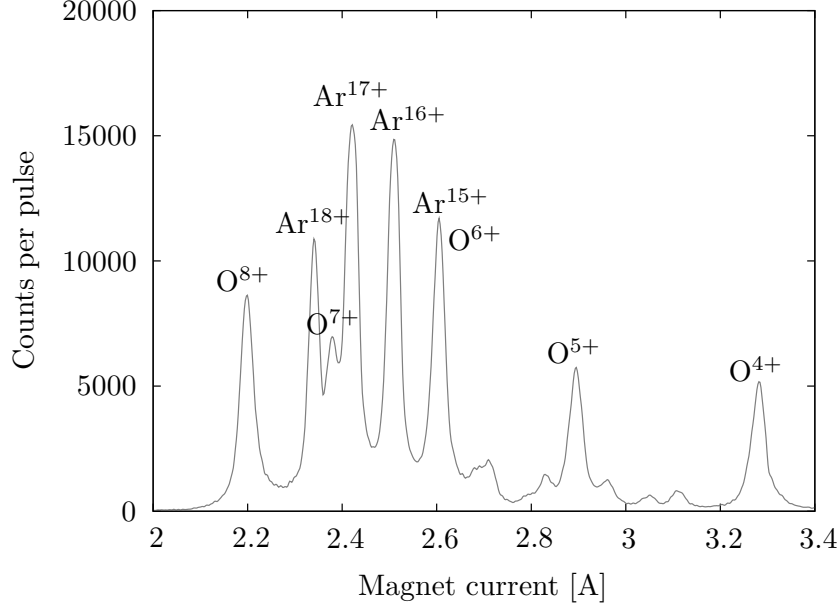


Figure 3.5: Wien scan of the charge states of argon ions extracted in pulse mode from the Berlin EBIT for a breeding time of 0.9 s. $I_e = 120$ mA, $V_a = 10.1$ kV, $V_{trap} = 100$ V and $V_{ext} = 5.2$ kV.

Ion beam diagnostics

In order to tune the ion beam, a means to monitor the extracted ions is necessary. There are various devices which can be implemented in a beamline for this purpose. The ion beam current is routinely measured using a Faraday cup, which is mounted on a manipulator for movement in and out of the beam, and these are positioned at various points along the beamline. Low ion flux can also be measured using MCP detectors, with an amplification factor (the number of secondary electrons generated per incident ion) of the order of 10^6 . If a phosphor screen is incorporated into the rear of the MCP setup the ion beam can also be imaged. A position sensitive MCP detector with a resistive anode, which was used in the investigations of HCI transport through nanoscale apertures, is described in Section 3.2.4.

3.2.3 Extraction onto a gas target

A schematic of the Berlin EBIT beamline, used for the experiments with extracted beams of HCIs onto an external gas target, is presented in Fig-

ure 3.6. As in the magnetic trapping experiment, charge exchange between $\text{Ar}^{17+,18+}$ ions and argon gas was investigated. The difference here is that the charge states can be selected individually and the collision velocity can be controlled over a wide range.

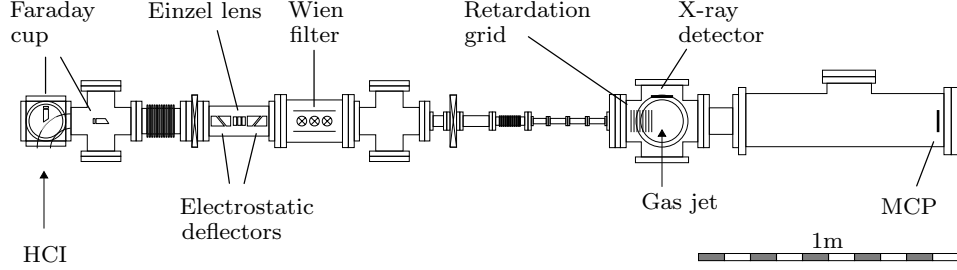


Figure 3.6: Schematic of the EBIT extraction beamline in Berlin incorporating a gas target.

Argon gas was injected into the EBIT using the gas injector at a backing pressure of 10^{-5} Pa and the ions generated were extracted in pulse mode at a rate of one ion bunch per second. An electron beam current of 120 mA was selected and the potentials on the drift tubes, set over the drift tube base potential, V_{drift} , were $V_{bottom} = 500$ V, $V_{middle} = 100$ V and $V_{top} = 200$ V. During the breeding phase of each cycle, lasting 0.9 s, V_{drift} was set to 10 kV giving an electron beam acceleration potential into the trap region, V_a , of $V_{drift} + V_{middle} = 10.1$ kV. This value was chosen to maximize the yield of the highest charge states, in the same way as the yield of Ar^{18+} was maximized in the magnetic trapping experiment. In the extraction phase V_{drift} was lowered to 5 kV and then V_{middle} was ramped up from 100 to 400 V over 0.1 s. This gave ion pulses of ~ 30 ms in duration at an extraction potential, V_{ext} , of $V_{drift} + V_{top} = 5.2$ kV.

The ion beam was transported through the beamline, a particular charge state selected using the Wien filter, and then just prior to the target area the retardation assembly was reached. The latter consists of a series of parallel grids biased to decelerate the ions and enabled a systematic investigation of the effect of collision energy on electron capture from the gas target to be carried out. The entry grid is at ground potential and the retarding potential, V_{ret} , selected for the last grid determines the ions' final kinetic energy, i.e:

$$E_{final} = eq(V_{ext} - V_{ret}). \quad (3.5)$$

The grid directly after the entry grid was typically set 100 V lower than

V_{ret} , and a uniform retarding field was achieved by biasing the following plates at successively increasing voltages, controlled by a series of resistors. Experiments were carried out with non-retarded ions and then using a range of retardation potentials. The slowest ions had an energy of $10q$ eV. A 10 mm diameter cylinder was positioned in close proximity to the final grid, and in electrical contact with it, so that the retarded ions passed through a field free drift region to the gas target. This prevented them from being re-accelerated.

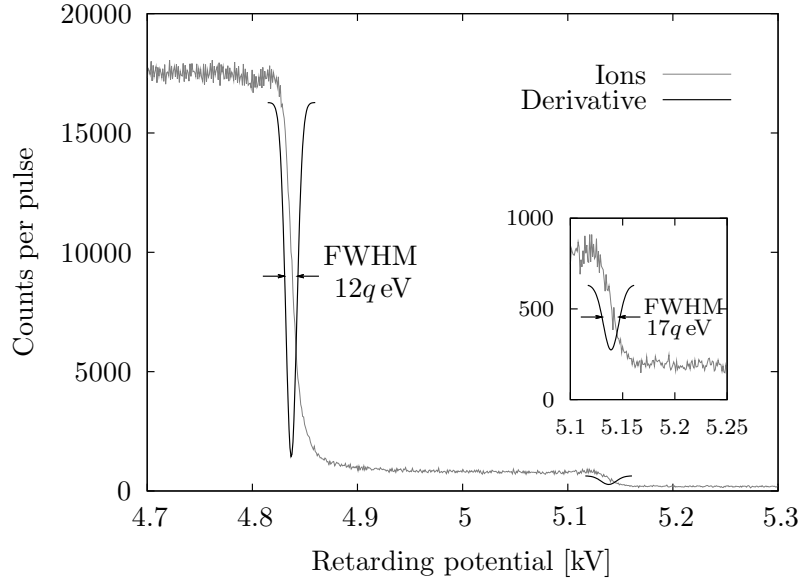


Figure 3.7: Reverse bias analysis of the extracted HCIs. The first step corresponds to Ar^{17+} ions selected by the Wien filter and the second, to Ar^{16+} ions formed by charge exchange in the beamline.

In order to measure the mean energy and energy spread of the extracted ions, scans of V_{ret} were implemented and the ion count rate was monitored on the MCP at the end of the beamline. Figure 3.7 shows the result of a measurement for Ar^{17+} ions selected by the Wien filter. The extraction potential in this particular example was 5.1 kV. On continuous increase of the reverse bias there comes a point when the ions start to be reflected. Subsequently a sharp decrease in the ion count rate is observed until all the ions of a given energy are repelled. From the peak position of a Gaussian fitted to the derivative of this decrease, the mean energy of the Ar^{17+} ions can be inferred. Here a mean energy of $4.837q$ keV is determined, giving a reduction in energy from the extraction potential of $\sim 260q$ eV. Since the ions

are accelerated from the top of the trap to ground potential, this quantifies the combined effect of the ion and electron space charge on the potential experienced by the ions at the top drift tube. The space charge component due to the electron beam in this region can be estimated using Equation 2.1, which for the experimental parameters $I_e = 120$ mA, $V_{ext} = 5.1$ kV and $\rho = r_{top} = 0.03$ cm, with $r_e = 35$ μ m, gives ~ 370 V. From the difference between this value and the 260 V calculated above, a value of ~ 110 V for the space charge potential of the ions is inferred. This estimates a space charge compensation factor of the electron beam of 30 %. The energy spread of the Ar^{17+} ions is given by the FWHM of the Gaussian distribution, measured as 12 q eV. A second much smaller step centred at 5.139 q keV with a FWHM of 17 q eV is also observed. The position of this step is consistent with the energy of Ar^{16+} ions which are formed when a fraction of the Ar^{17+} ions selected by the Wien filter undergoes charge exchange in the beamline prior to the retardation setup. From the step heights the amount of single electron capture by Ar^{17+} which occurred is estimated at 4 %.

Argon gas was injected into the target region using a pulsed supersonic valve directed at 90° to the ion beam axis. The valve operates via a pair of parallel beam conductors in a hairpin configuration, through which a high current is passed in opposite directions. The resulting magnetic force causes one of the beams, which is free to move, to lift, allowing a small amount of gas into a specially designed nozzle from which it expands supersonically into the target region. Typically the valve was operated with a current of 3.6 kA and a backing pressure of 10^4 Pa. Gas pulses were ~ 60 μ s in length and synchronized to coincide with the arrival of ion bunches from the EBIT.

In order to detect x-ray photons from the HCl-gas charge exchange interactions, a solid state *Amptek XR-100CR* x-ray detector is installed at the target, perpendicular to both the ion beam axis and the gas jet. The detector implements a thermoelectrically cooled silicon P-I-N photodiode, with an active area of 5 mm² and a FWHM peak resolution of 168 eV at 5.9 keV. It is mounted 44 mm from the target centre, giving a solid angle for photon detection of $2.6 \cdot 10^{-3}$ sr. A 12.5 μ m beryllium window separates the diode from vacuum, resulting in significantly reduced transmission below 2 keV. This is not of importance for the x-ray measurements carried out here, as the energy range of interest is higher. Calibration of the detector in the range of 2.3 to 6.5 keV was carried out before installation into the beamline using Mn K_α and K_β line emissions from a ⁵⁵Fe source and also the K -lines from the excitation of Ca, Cl and S samples with the radioactive source. Database

values for the x-ray emission lines were taken from [Thompson et al., 2001]. From a linear fit to the calibration points a calibration accuracy of ± 12 eV is inferred.

The duration of the extraction experiments ranged from 1 hour for the fastest ions up to 30 hours for the slowest ions. This large time difference results from ion losses due to defocusing in the retardation assembly, which became severe for the largest retardation potentials implemented. The results of these extraction experiments are presented in Section 5.1.2.

3.2.4 Extraction onto nanoscale apertures

For the investigation of electron capture by HCIs from surfaces, special targets relevant to the ion implantation setup discussed in Chapter 1 were prepared. These were then mounted in an analysis chamber which was installed at the end of each of the two EBIT beamlines in Berkeley for experiments with the extracted ions.

The target material was silicon nitride, in the form of low stress membranes of thickness 200 nm and 500 nm, mounted on silicon frames. Nanoscale holes of diameter 100 to 300 nm were formed in the membranes and imaged *in situ* using the FEI Strata 235 Dual Beam Focused Ion Beam (FIB) microscope at the National Center for Electron Microscopy (NCEM) in Berkeley. This device combines a low divergence, highly focused Ga^+ ion beam with a Scanning Electron Microscope (SEM) column. The electron and ion beam are aligned at 45° to one another and can be rastered across surfaces creating secondary electrons which are detected for imaging. In addition, the beams can be used to modify surfaces. In this work the electron beam was used to image the samples while the ion beam was used to drill holes by sputtering, forming the nanoscale apertures. A 30 keV Ga^+ beam with an intensity of 10 pA and a diameter of 10 nm was used to drill arrays of up to 800 holes. Before loading into the FIB chamber, the membranes were sputter coated on both sides with a thin film (~ 20 nm) of gold-palladium alloy, in order to prevent charging under ion and electron beam exposure.

The maximum aspect ratio (hole diameter to depth) achievable using the FIB technique on the membranes was about 5:1, which results from a balance of sputtering and re-deposition of target material. For high aspect ratios re-deposition dominates, precluding the direct drilling of deep, narrow holes. However, holes with smaller diameters than achievable by direct drilling alone can be formed via electron and ion beam assisted thin film

deposition [Schenkel et al., 2003b]. A gas needle is used to expose the target to a precursor gas, e.g. an organometallic compound containing platinum or the gas tetraethylorthosilicate, and at the same time the ion or electron beam is scanned over the area of interest. The primary beam, in combination with the secondary electrons produced when the beam strikes the surface, then causes the gas to be cracked. As a result thin films are deposited. This method was used here to close 100 nm diameter holes down to a final diameter of 50 nm.

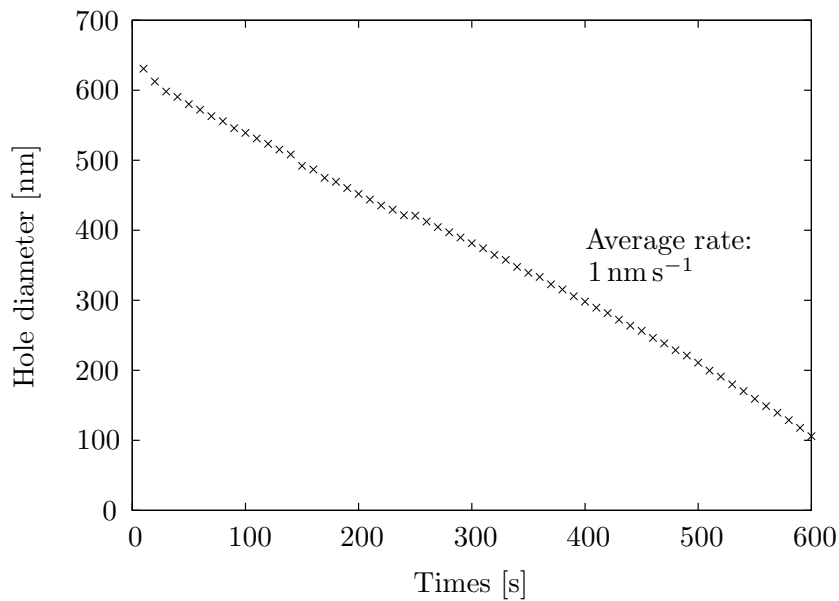
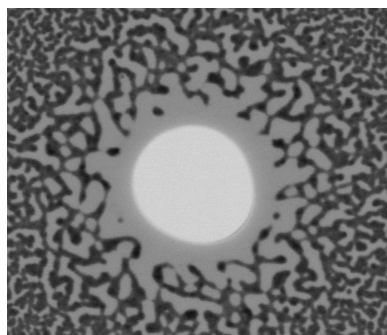


Figure 3.8: Rate of hole closing by platinum deposition.

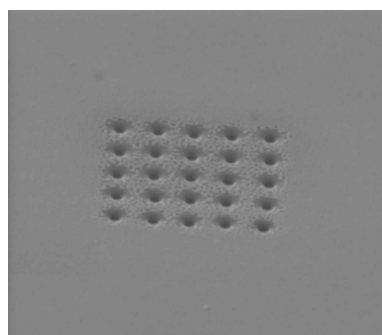
In order to investigate the process of hole closing over time, a larger 630 nm diameter hole in a 200 nm thick membrane was exposed to platinum vapour and a 20 keV electron beam for a total of 600 s. In 10 s intervals the process of platinum deposition was interrupted to take an image of the hole with the SEM. As a result the diameter of the hole after each deposition step was able to be determined. The results are shown in Figure 3.8. A hole closing rate of $\sim 1 \text{ nm s}^{-1}$ is inferred. It should be noted, however, that the cross sections of the reduced diameter holes were found to be asymmetric [Minor et al., 2004]. This is attributed to the precursor gas streaming in from one side. The effect appears to have been more pronounced for the insulator deposition than for platinum, hence only holes closed with platinum were

used in the transport studies.

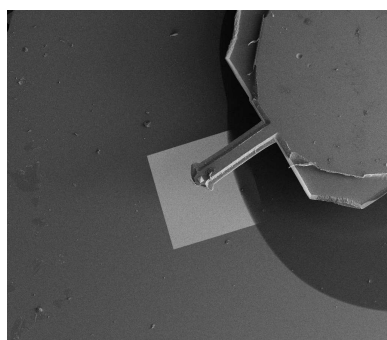
SEM images of some of the targets prepared for the charge exchange experiments are presented in Figure 3.9. Figure 3.9(a) shows a 100 nm diameter hole drilled into a 500 nm thick membrane and Figure 3.9(b) shows an array of these holes. Light and dark areas show contrast due to the gold-palladium coating. Additional targets were prepared to test the principle of transporting ions through aligned holes in an AFM tip and a collimating membrane. Figure 3.9(c) shows an AFM cantilever which was mounted over a silicon nitride membrane using silver epoxy glue. The FIB was then used to drill a



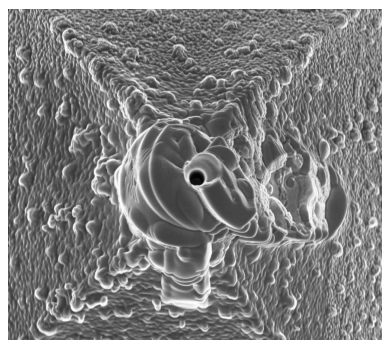
(a) A 100 nm diameter hole in a silicon nitride membrane coated with a gold-palladium alloy.



(b) An array of 25 holes; arrays of up to 800 holes were used in the experiments.



(c) An AFM cantilever mounted over a silicon nitride membrane.



(d) A $1.5\mu\text{m}$ diameter hole in the chromium pyramid of an AFM tip.

Figure 3.9: Nanoscale aperture targets prepared for the study of electron capture by HCIs from surfaces.

hole through the hollow chromium AFM tip and the membrane below. The $1.5\ \mu\text{m}$ diameter hole in the tip can be seen in Figure 3.9(d).

Once the targets were prepared, the HCI-surface charge exchange investigations commenced. These experiments were first carried out using the EBIT-II beamline, a schematic of which is shown in Figure 3.10. At 90° to the EBIT axis, in the plane of the beamline, there is an additional ion source for low charge state ions, the *04-303 Physical Electronics Industries* sputter ion gun. It produces a continuous beam of ions via ionization by a heated filament and was used for preliminary tests with the targets. Argon gas at a pressure of 10^{-4} Pa was fed to the ion gun chamber and Ar^+ to Ar^{4+} ions were extracted using potentials of up to 4 kV on the acceleration grid at the exit. The advantage of the ion gun is that it is a high current source enabling relatively short experiments compared with EBIT runs, albeit with low charge states.

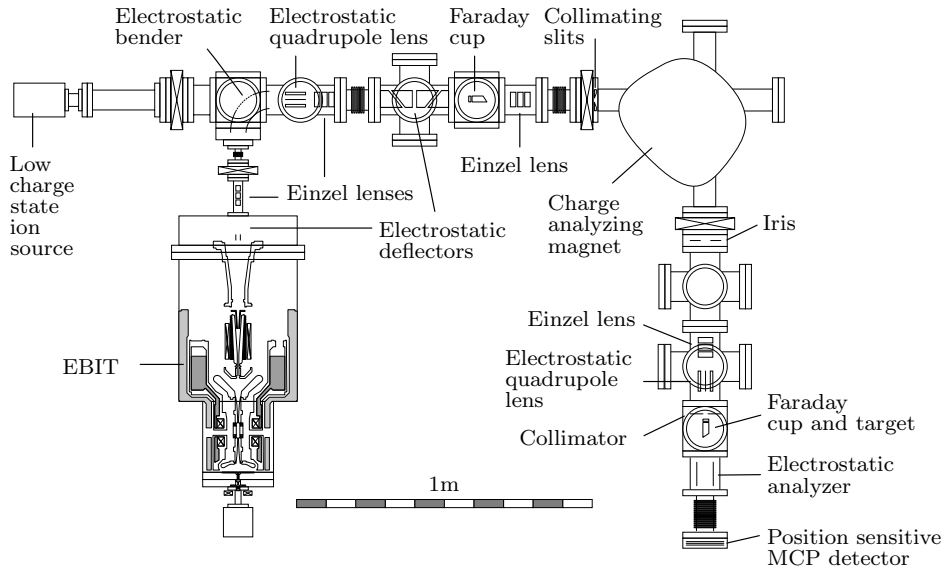


Figure 3.10: Schematic of the EBIT-II extraction beamline incorporating a solid target.

In the subsequent experiments with HCIs from EBIT-II and the REBIT highly charged argon and xenon ions were used. The respective precursor gases were injected into the traps at backing pressures of the order of 10^{-4} Pa. Due to the range and relative abundances of the naturally occurring isotopes of xenon, isotopically pure xenon gas, ^{136}Xe , was used. Typically electron

beam currents of 50 to 70 mA and acceleration potentials of 4 to 8 kV were selected, and an axial trap depth of 100 V was applied. Ion extraction proceeded in pulse mode at a rate of one ion bunch per second, with extraction potentials ranging from 5 to 9 kV.

The ions were transported through the EBIT-II beamline, which was at a base pressure of 10^{-6} Pa, and selected according to their mass-to-charge ratio by the bender magnet. The emerging ion beam was collimated to a spot size of 3 mm and the upper limit on the beam divergence just before the target was estimated at 0.8° . The HCIs of argon typically selected were Ar^{16+} , due to the relatively high extraction yield of this ion resulting from its closed shell configuration. In the case of the HCIs of xenon, Xe^{44+} was chosen for the same reason. For the experiments using the low charge state source in the EBIT-II beamline, the electrostatic bender was grounded to allow those ions to pass through the transmission grid in the outer bender plate straight into the beamline. The layout of the REBIT beamline is much the same as that of EBIT-II, except that there is no 90° electrostatic bender. This is because the REBIT is installed with its axis horizontal, i.e. ions can be extracted and transported straight towards the bender magnet. There is also no low charge state ion source installed.

The silicon nitride membranes with the nanoscale holes and the AFM tip/membrane assemblies were mounted in the target region, near the end of the beamline. Using copper tape they were attached to a metal disc on the end of a Faraday cup of diameter 10 mm and length 50 mm. This enabled the ion current incident on the apertures to be measured. The front of the Faraday cup was biased negatively, typically to -200 V, in order to prevent the escape of secondary electrons. A second Faraday cup mounted parallel to the first enabled two targets to be in the beamline at the same time. The arrangement was fixed to a manipulator to allow each cup to be moved in and out of the beam as required.

A survey of the transport of low charge state argon ions through the range of samples of varying aperture aspect ratios was undertaken. The experiments with HCIs, however, concentrated on a 500 nm thick silicon nitride membrane sample with 200 nm diameter holes. The reason for this was that the experiments with HCIs involved up to 20 hours of beam exposure, due to the relatively low beam currents from the EBIT (picoamperes per charge state on a beam spot of 3 mm compared with the nanoamperes per charge state extracted from the ion gun). This demonstrates the importance of drilling large numbers of holes into the targets, which was in itself also a

time-consuming task.

The charge states of the ions emerging from the nanoscale apertures were separated using an electrostatic analyzer. This consists of two parallel plates, typically biased at ± 100 V, positioned 35 cm downstream of the targets. Ions in the highest charge states are deflected the most and neutrals are left undeflected. Figure 3.11 demonstrates the principle. After an ion flight distance of 45 cm, particle detection was achieved using a position sensitive detector consisting of two 40 mm diameter MCPs and a resistive anode, in that order, in a sandwich arrangement. The front side of the first channel plate was biased negatively, typically at -900 V, to accelerate the positive ions towards the detector. A positive potential gradient was supplied to accelerate the secondary electrons through the stack, with the interface between the two plates at 0 V, the back face of the second plate typically at +900 V and the resistive anode biased slightly higher, at around +950 V. The resistive anode is responsible for the position sensitive detection and comprises a square conductive sheet with a wire connection to each corner. The signals from each of the corners are amplified and the charge ratio from opposite corners gives the event position. In this way a 2D picture of particle events is obtained.

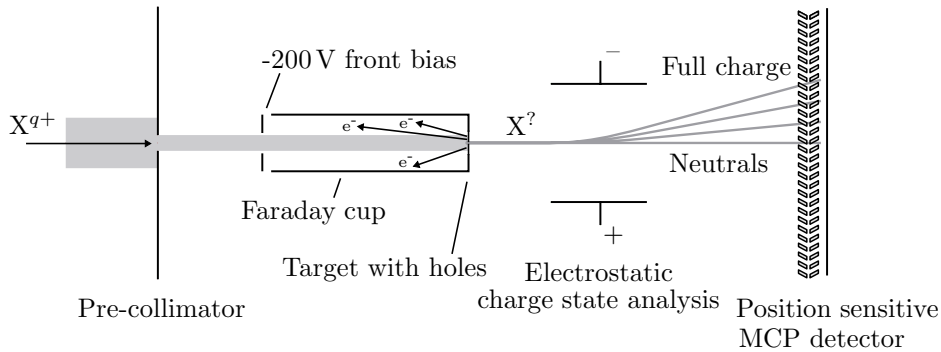


Figure 3.11: Setup for the electrostatic charge state analysis of ions transported through nanoscale apertures.

After exposure of the hole arrays to ions, the targets were imaged using the SEM capability of the FIB microscope. This is because electronic sputtering, due to the impact of HCl_is in particular, could have led to hole enlargement [Schenkel et al., 1999]. In contrast, in the literature a competing process of hole closing by ad-atom diffusion has also been reported, which occurs under specific conditions of target temperature, composition and ion dose rate [Li et al., 2001]. On inspection, however, no change in the aperture

structure was observed. Hence it is concluded that significant target erosion or ad-atom diffusion did not occur. The results of the extraction experiments onto nanoscale apertures are presented in Section 5.2.

Chapter 4

Features of Charge Exchange Emission

To facilitate the interpretation of the x-ray emission recorded in the investigations of HCI-gas charge exchange, a series of emission spectra have been simulated. This chapter presents these theoretical spectra, which are based on calculations of the electron cascades for a range of likely capture states. The effect of multiple capture on the x-ray spectra is also discussed.

4.1 Cascade simulations

As introduced in Chapter 1, collisions between slow ($\sim v_{Bohr}$) HCIs and neutrals are dominated by electron capture. One or more electrons are transferred into Rydberg states of the HCI, which then stabilizes via a combination of radiative decay and autoionization. The focus in this work is on radiative decay, which is the principal relaxation mechanism following electron capture into very highly ionized species [Cowan, 1981], such as those investigated here. The radiative cascade of an electron to the ground state results in a photon emission spectrum which is characteristic of the initial capture state. Hence a comparison of the various spectra recorded in the magnetic trapping and extraction experiments should allow any dependence of the capture state on the experimental conditions to be inferred.

An analytical method widely used to describe charge exchange by slow HCIs is the classical over-the-barrier (COB) model. It was initially developed to predict cross sections for single electron capture into bare projectiles from atomic hydrogen [Ryufuku et al., 1980], then augmented to include

multielectron targets [Mann et al., 1981] and further extended to account for multiple electron capture [Bárány et al., 1985; Niehaus, 1986]. The model is essentially a static treatment and is based on a consideration of the electrostatic potential experienced by the active electron during transfer. For a fully stripped HCI of charge q interacting with an atomic target, the superposition of the two Coulomb potentials, in atomic units, is given by:

$$U(r) = -\frac{q}{|r|} - \frac{1}{|R-r|}, \quad (4.1)$$

where r is the electron-HCI distance and R is the target-HCI distance. The barrier to charge exchange is determined by the maximum between the two potential wells:

$$U_{max} = -\frac{(\sqrt{q}+1)^2}{R}. \quad (4.2)$$

As the HCI approaches the target, the barrier is lowered. Then once U_{max} dips below the binding energy of the target electron, which is Stark-shifted by the Coulomb potential of the HCI, the electron can be transferred classically to the projectile. This condition for electron capture can be written as:

$$-I_P - \frac{q}{R} \geq -\frac{(\sqrt{q}+1)^2}{R}, \quad (4.3)$$

where I_P is the ionization potential of the electron on the target. Figure 4.1 illustrates the situation, showing the electrostatic potential experienced by the active electron just prior to capture. Electron transfer due to quantum mechanical tunneling through the barrier is neglected, because tunneling rates are low compared with the timescale of the interaction.

The second requirement for capture is the resonance condition:

$$-I_P - \frac{q}{R} = -\frac{q^2}{2n^2} - \frac{1}{R}, \quad (4.4)$$

which states that the Stark-shifted binding energy of the target electron must equal the binding energy, E_n , of a hydrogenic state in the HCI with principal quantum number n , which is Stark-shifted by the Coulomb potential of the ionized target.

The critical distance for electron capture, R_c , can be obtained by solving Equation 4.3 for R , which gives:

$$R_c = \frac{2\sqrt{q}+1}{I_P}. \quad (4.5)$$

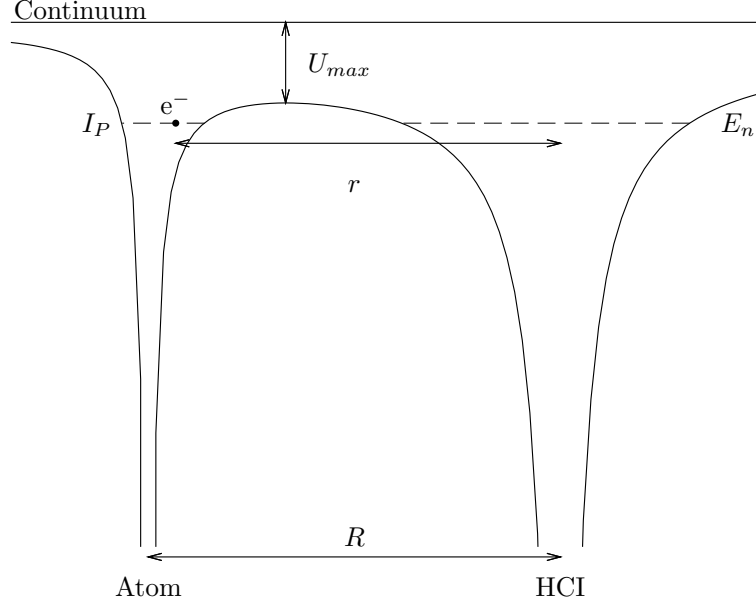


Figure 4.1: Electrostatic potential experienced by the active electron of an atomic target close to the critical distance for capture by a HCl. The electron-HCl distance, r , target-HCl distance, R , ionization potential of the target, I_P , binding energy of a hydrogenic state in the HCl, E_n , and the potential barrier maximum, U_{max} , are marked.

Then by substituting R_c into Equation 4.4, the principal quantum number of the capture state in the HCl can be predicted using:

$$n_c = \sqrt{\frac{1 + 2\sqrt{q}}{4 + 2\sqrt{q}}} \frac{q^{3/4}}{\sqrt{I_P/13.6}}, \quad (4.6)$$

with q in units of electron charge and I_P in electronvolts. For $q \gg 1$ the following approximation is obtained:

$$n_c \simeq \frac{q^{3/4}}{\sqrt{I_P/13.6}}. \quad (4.7)$$

Comparison with experiment has shown that Equation 4.6 underestimates n_c slightly and that in fact Equation 4.7 gives more accurate predictions. For a recent example see [Otranto et al., 2006] in which the line emission cross sections for electron capture by O^{8+} from a range of targets are presented.

The results of classical trajectory Monte Carlo (CTMC) calculations are also in support of the approximated relation [Olson, 1981].

Electron capture does not proceed into a unique n capture state, however. Instead, experimental data show that a range of n -states centred around n_c becomes populated and that the distribution broadens for increasing collision velocities [Janev and Winter, 1985]. For the slow collisions relevant to this thesis, state-selective measurements reveal a narrow distribution of $\Delta n \approx \pm 1$ [Cassimi et al., 1996]. This dynamical effect is explained by A. Niehaus in his Molecular COB model for multiple electron capture [Niehaus, 1986]. In the molecular extension two stages of the collision process are distinguished; the ‘way in’ and the ‘way out’. (In the previous description only the former was considered.) On the ‘way in’ the HCI approaches the target and the Coulomb potential barrier experienced by the target electrons lowers. During this phase the barrier ceases to be effective in order of increasing Stark-shifted ionization potentials of the target electrons. As a result the target electrons sequentially become ‘molecular’, i.e. they become shared between the HCI and the target. The barrier continues to be reduced until a turning point is reached, at which the target-HCI distance equals the impact parameter of the collision. Then on the ‘way out’ the HCI and target separate. The potential barrier rises and the ‘molecular’ electrons are sequentially, in order of decreasing Stark-shifted binding energies, either captured by the HCI or recaptured by the target, there being a finite probability for each outcome. Considering the time dependence of the barrier height during electron transfer and applying the time-energy uncertainty relation, a minimum uncertainty in the barrier height for a given time interval of a measurement is inferred. This uncertainty, which is proportional to the collision velocity, is then used to estimate the actual uncertainty in the barrier height. Consequently a velocity-dependent ‘energy window’ for electron capture into the HCI is obtained, within which several n -states are available.

In slow collisions n_c is virtually independent of collision velocity. The same cannot, however, be said for the orbital angular momentum capture state, ℓ_c , which is found to depend strongly on collision velocity in the low energy regime [Janev and Winter, 1985; Dijkkamp et al., 1985]. The velocity of the projectile relative to the target is not considered in the COB model treatments discussed. As a result, an estimate of ℓ_c cannot be directly inferred. In an attempt to rectify this, Burgdörfer *et al.* proposed an extension to the COB model to allow the angular momentum distribution of the captured electron to be described [Burgdörfer et al., 1986]. The modification

is based on the assumption that the initial angular momentum, L , of the active electron is conserved during capture. As viewed in the rest frame of the projectile, L is thus estimated using:

$$L \simeq bv, \quad (4.8)$$

where b is the impact parameter of the collision and v is the relative collision velocity. Atomic units apply. From this it can be seen that for decreasing collision velocity, electron capture into lower ℓ_c -states is expected. Burgdörfer *et al.* then include a term for the centrifugal potential of the electron orbiting the projectile into Equation 4.1. In order to calculate the angular momentum distribution of the captured electron, the geometric cross section for charge exchange is decomposed into rings corresponding to the partial cross sections for each subshell. On comparison with the experimental data for single electron capture in [Dijkkamp et al., 1985], it was found that the mean angular momentum of the captured electron could be predicted with reasonable success. In contrast, predictions of the distribution of angular momentum values were unreliable. More accurate calculations can be made using numerical quantum mechanical and Monte Carlo methods. To date, however, the focus has mainly been on the high energy collisions of relevance to high temperature laboratory plasmas. Therefore theoretical and experimental work in the energy range of relevance to this thesis is limited.

For the purposes of the simulations of $\text{Ar}^{17+,18+}$ -Ar charge exchange emission performed here, n_c is first predicted using Equation 4.7, giving $n_c = 8$. Then cascades from the various $8\ell_c$ -states are calculated. The spectroscopic notations s, p, d, f, g, h, i, j to denote the orbital angular momentum quantum states $\ell = 0, 1, 2, 3, 4, 5, 6, 7$, respectively, are used. Atomic data for the energy levels and transition probabilities of hydrogen-like and helium-like argon ions, corresponding to single electron capture into Ar^{18+} and Ar^{17+} , respectively, were supplied by S. Fritzsche from the University of Kassel [Fritzsche, 2003] using the Relativistic Atomic Transition and Ionization Properties (RATIP) code [Fritzsche, 2001, 2002]. The energies of the various $n\ell j$ -states (where j is the quantum number for spin) up to $n = 8$ and the transition probabilities for all the electric dipole-allowed (E1) cascading transitions in that range are given. Note that in the helium-like configurations one electron is in the 1s-state, as is the case for single electron capture into a non-excited Ar^{17+} ion. In addition, for the hydrogen-like data set transition probabilities for the electric quadrupole (E2), magnetic dipole (M1) and magnetic quadrupole (M2) cascade steps were also supplied, so that the

effect of these electric dipole-forbidden transitions on the emission spectra could be investigated. As the emphasis of this study is on the ℓ_c selectivity of charge exchange, the cascade spectra for capture into the various $8\ell_c$ -states are averaged over the composite $8\ell_c j_c$ results, equal population of j_c being assumed. Therefore, in the following discussion reference to $n\ell$ -states only is made.

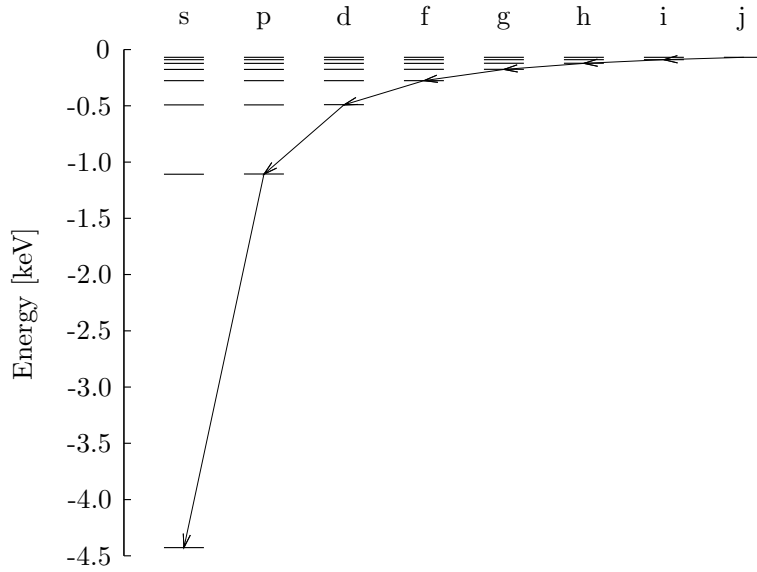


Figure 4.2: Energy levels for hydrogenic argon showing the electron cascade from state 8j.

To illustrate the simplest cascade scenario, Figure 4.2 presents an energy level diagram for hydrogenic argon showing the electron cascade following capture into the state 8j ($\ell_c = 7$). The only allowed transitions are those following the selection rules $\Delta n \geq 1$ and $\Delta \ell = \pm 1$. Thus for capture into 8j there is only one transition possible at each step. This sequence is known as the Yrast chain. In contrast, cascades from the remaining $8\ell_c$ -states have more than one possible transition available at each step, therefore opening up a large number of possible decay paths.

The energy of the photon in a given cascade step is given by:

$$E_\gamma = E_{n\ell} - E_{n'\ell'}, \quad (4.9)$$

where $E_{n\ell}$ and $E_{n'\ell'}$ are the energies of the initial and final states, respectively. The intensity, J , of the transition can be calculated from the so-called

branching ratio of the cascade step, according to:

$$J_{n\ell}^{n'\ell'} = \frac{A_{n\ell}^{n'\ell'}}{\sum_{n'\ell'} A_{n\ell}^{n'\ell'}}, \quad (4.10)$$

where $A_{n\ell}^{n'\ell'}$ is the corresponding transition probability, or Einstein coefficient. In the cascade simulations all the possible decay paths are tracked, each path consisting of a series of radiative steps from the capture state to the ground state. The probability for a given decay path is obtained from the product of the branching ratios of all steps in that path. Then by summing the probabilities obtained for each transition over all the decay paths, plots of transition intensity versus energy can be obtained.

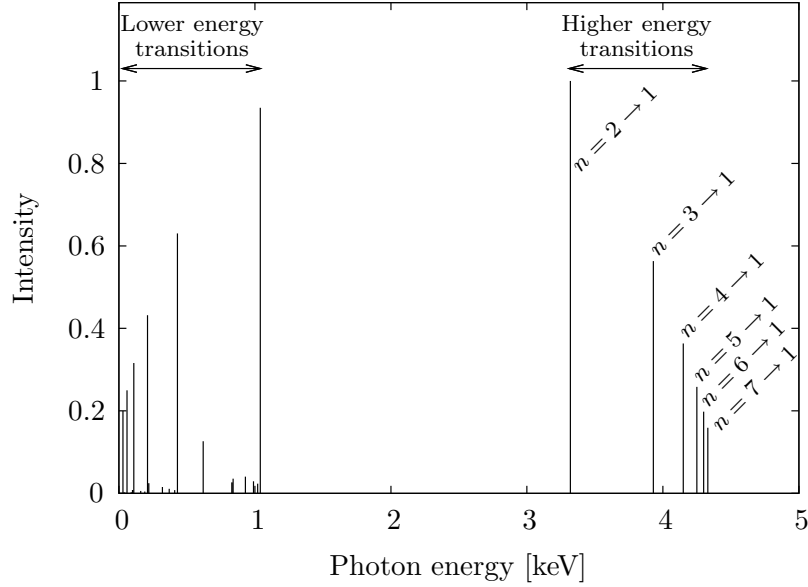


Figure 4.3: Normalized line emission spectrum in the full energy range simulated for electron capture by Ar^{18+} into the state $8s$.

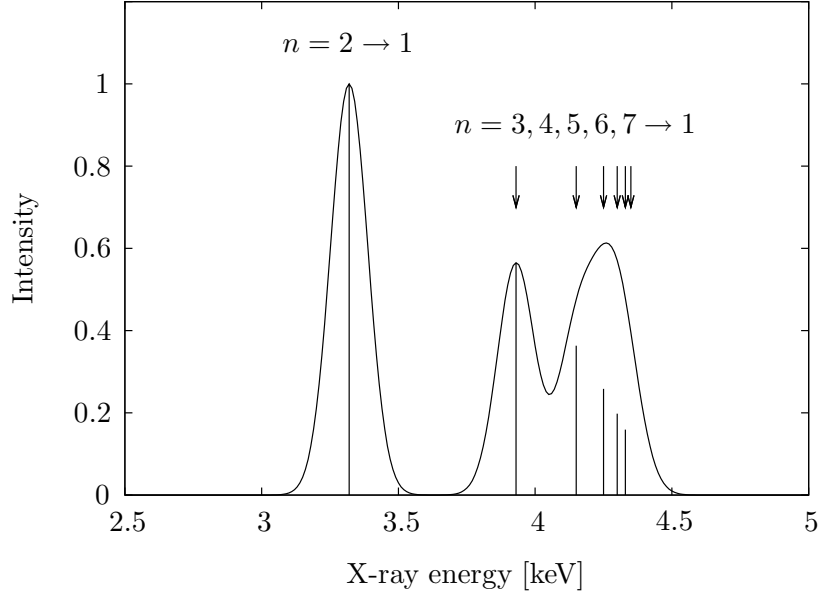
In Figure 4.3 the normalized line emission spectrum simulated for electron capture into the $8s$ -state of Ar^{18+} , using E1 transitions only, is plotted. Essentially the spectrum consists of two parts. The first part appears at 1 keV and below, in the soft x-ray to the extreme ultraviolet regime, and corresponds to transitions into a final state with $n \geq 2$. The second part, in the x-ray regime between 3 and 5 keV, corresponds to all transitions into the state $n = 1$. The individual K -shell line emissions of this portion are

labeled. Note that for capture into 8s there is no emission from $n = 8 \rightarrow 1$, as this would be a ‘forbidden’ $\Delta\ell = 0$ transition. In the experiments, the focus was on photon detection in the energy range of the K -shell emission, i.e. the measurements are sensitive to the last step in the radiative decay. Thus from now on only the high energy portions of the simulated spectra are presented.

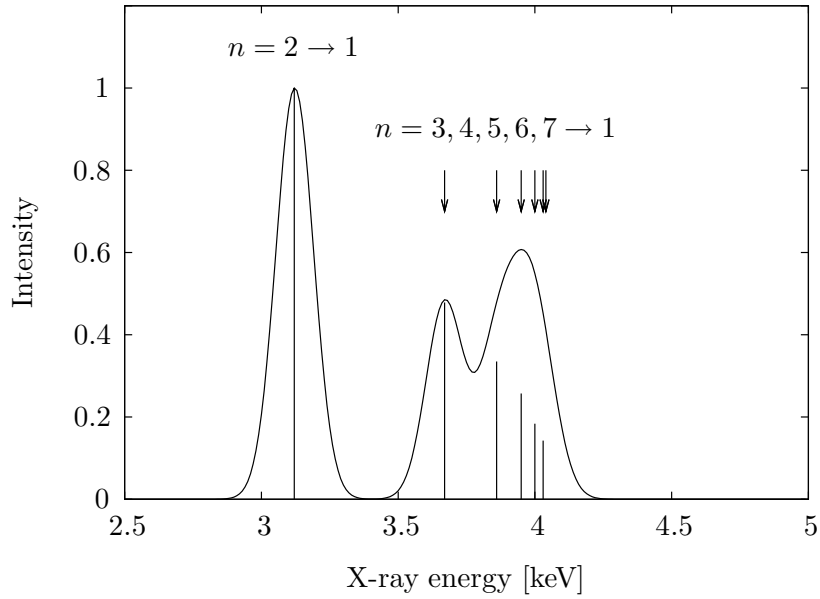
The line emissions for electron capture into Ar^{17+} are shifted to slightly lower energies than those for Ar^{18+} , due to the shielding of the nuclear potential by the 1s electron in the helium-like system. This can be seen clearly in Figure 4.4, where the simulated x-ray emission spectra for capture into the 8s-state are presented for both ion charge states. For the $n = 2 \rightarrow 1$ line emission, the energy shift amounts to ~ 200 eV. In order to distinguish the shielded from the non-shielded scenario, emission from an ion with one electron in the ground state is often termed normal satellite emission, while for an ion with two vacancies in the ground state the term hypersatellite emission is used. This terminology will be of use in Section 4.2. Experimental spectra are of course subject to detector broadening, therefore to form an idea of what the measured spectra might look like, the lines in each spectrum in Figure 4.4 have been replaced with Gaussian distributions and the sum of these gives the broadened spectra plotted. For direct comparison with the spectra recorded in the magnetic trapping experiments, a peak FWHM of 160 eV is used. The peaks measured in the extraction experiments are slightly broader, as will be seen.

The full series of emission spectra simulated for capture into the various $8\ell_c$ -states for Ar^{18+} and Ar^{17+} charge exchange are presented in Figures 4.5 and 4.6, respectively. Only the line-broadened plots are shown, again calculated using a Gaussian FWHM of 160 eV. The spectra for Ar^{18+} are simulated using E1 transitions only (solid curves) and then once more including the ‘forbidden’ M1, E2 and M2 transitions (dashed curves). It can be seen that for capture into 8s- and 8p-states, the inclusion of ‘forbidden’ transitions in the cascade calculations noticeably alters the relative weights of the emission peaks, while for the remaining spectra this effect diminishes. The difference is that when the second data set is implemented the $n = 2 \rightarrow 1$ peak is enhanced with respect to the peaks from higher energy transitions. This can be explained in terms of more efficient feeding and decay of $n = 2$ states, due to the inclusion of ‘forbidden’ $\Delta\ell = 0$ transitions.

In all the Ar^{18+} spectra, except that for capture into 8p, the $n = 2 \rightarrow 1$ (K_α) peak is the most intense. The reason is that this transition is fed by



(a) Capture into Ar^{18+}



(b) Capture into Ar^{17+}

Figure 4.4: Normalized x-ray emission spectra simulated for electron capture by Ar^{18+} and Ar^{17+} into the state 8s. A broadened envelope, obtained by replacing the line emissions with Gaussian distributions of FWHM 160 eV, is plotted in each.

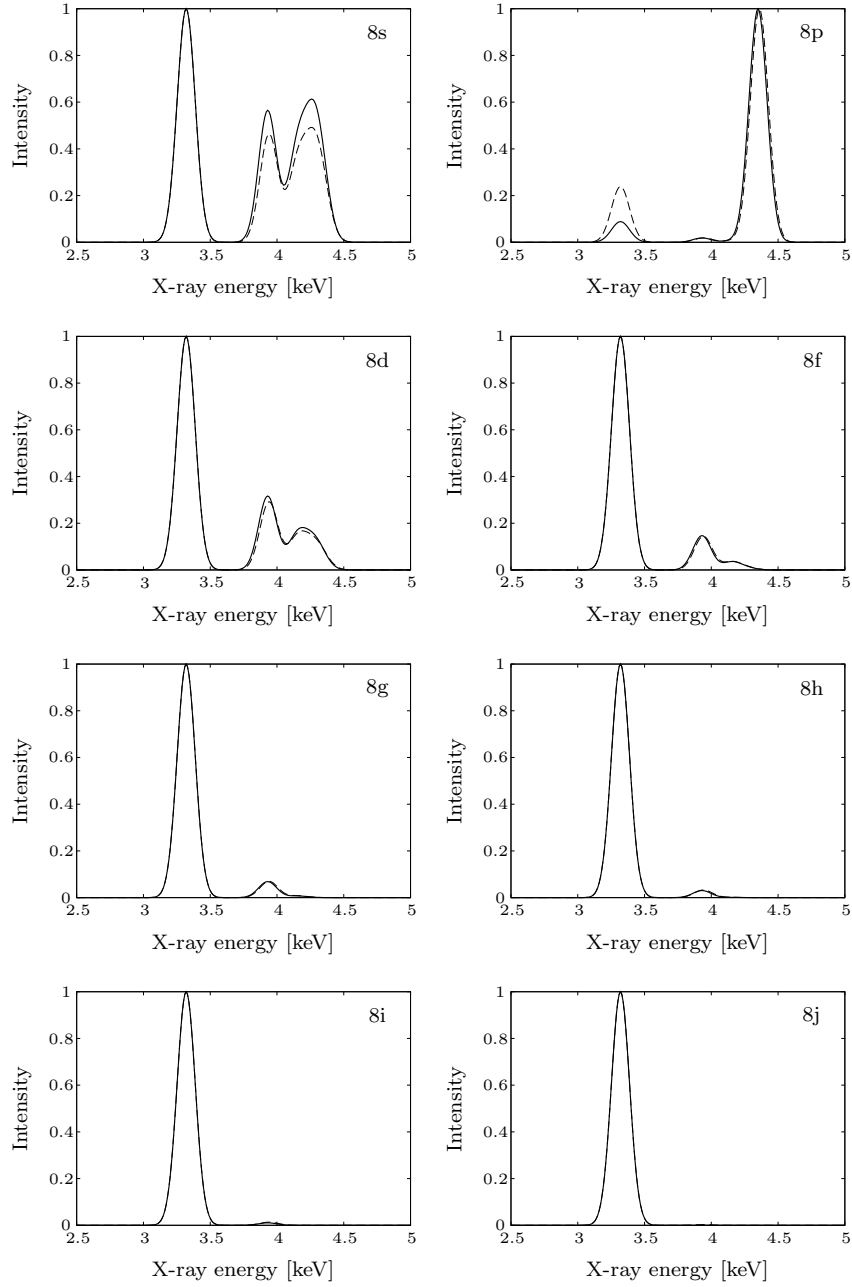


Figure 4.5: Normalized x-ray emission spectra simulated for electron capture by Ar^{18+} into the states 8s–8j, with a line broadening of 160 eV. Solid curves are for E1 transitions only and dashed curves are for E1, M1, E2 and M2 transitions.

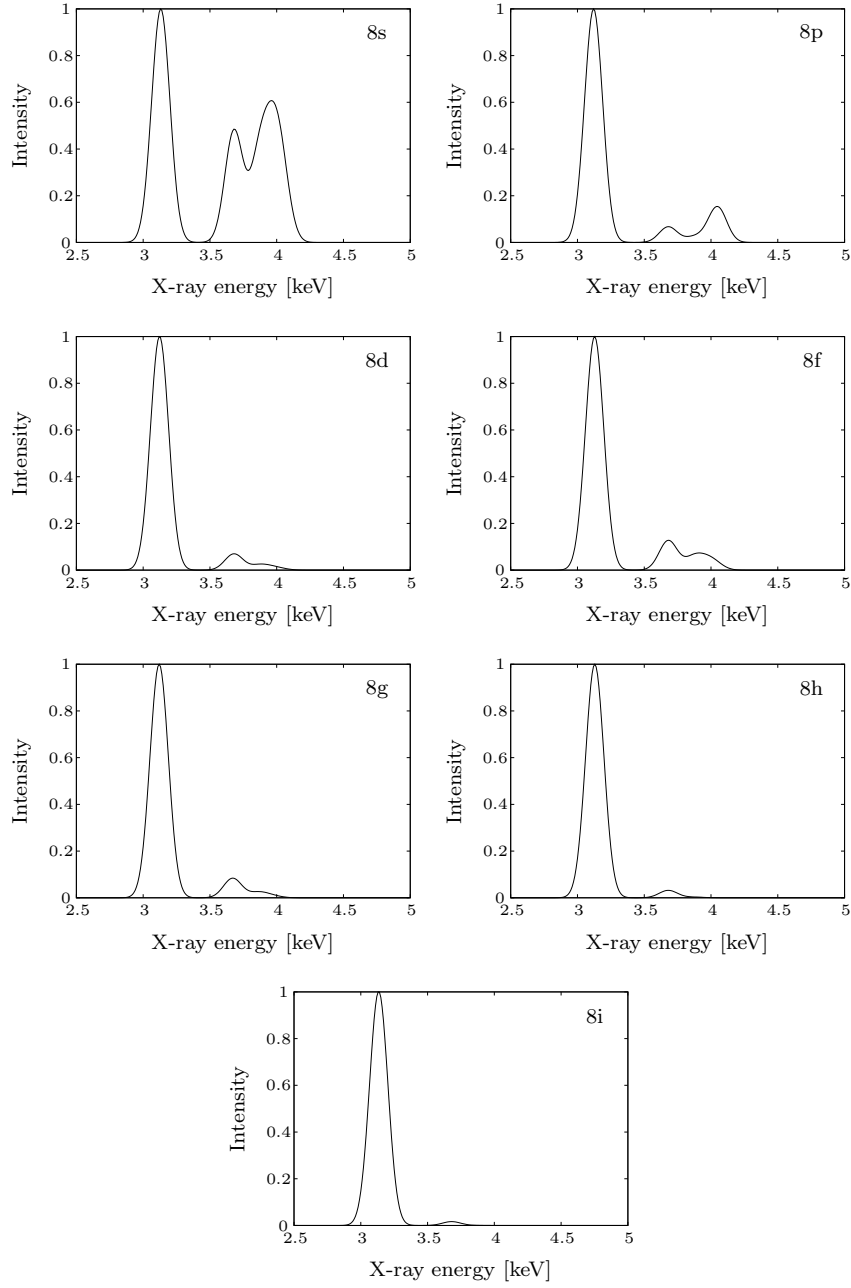


Figure 4.6: Normalized x-ray emission spectra simulated for electron capture by Ar^{17+} into the states 8s–8i, with a line broadening of 160 eV. The simulations are for E1 transitions only.

all cascades from higher levels, except those ending in direct steps to $n = 1$, which give rise to the remaining K -shell emissions. For cascades from $8p$ the K_α peak is relatively weak, because the $8p \rightarrow 1s$ transition dominates. The second most intense emission in the $8s$ and $8d-8j$ spectra corresponds to the $n = 3 \rightarrow 1$ (K_β) transition, it too being fed by a large proportion of cascades. Note that in the broadened spectra, the highest energy emission band is formed by a number of closely-lying emissions. Therefore, even though in the $8s$ spectrum the peak area of this band is larger than that of the neighbouring K_β peak, its constituent emissions are actually less intense, as seen in Figure 4.4. Following through the rest of the spectra a decrease in the relative intensity of $n \geq 3 \rightarrow 1$ emission is observed, which is due to those direct K -shell transitions becoming progressively less accessible. Finally, for capture into $8j$ only the K_α peak remains, as a result of the Yrast chain illustrated in Figure 4.2.

For the Ar^{17+} simulations only E1 transition probabilities were available, as mentioned previously. In addition, although data for capture into the state $8j$ could not be obtained using the present computational method, the $8j$ emission spectrum is predicted to be almost completely dominated by the K_α peak, as in the Ar^{18+} case. In any event, it will be seen that in the experiments electron capture was confined to the lower angular momentum states.

The main differences between the emission spectra for capture into Ar^{18+} and Ar^{17+} can be explained in terms of the unpaired electron present in the K -shell of the latter. As a result the captured electron has fewer cascade pathways available to it and a number of np -states will be metastable. This is particularly evident from the spectrum for capture into the $8p$ -state of Ar^{17+} in Figure 4.6, where the $8p \rightarrow 1s$ transition is dramatically de-emphasized because singlet $1s8p \ ^1P_1 \rightarrow 1s^2 \ ^1S_0$ decay is spin-allowed whereas triplet $1s8p \ ^3P_1 \rightarrow 1s^2 \ ^1S_0$ decay is spin-forbidden. The same applies to all singlet versus triplet decay, hence the relative intensities of the $n \geq 3 \rightarrow 1$ transitions in the remaining Ar^{17+} spectra are also lower than their Ar^{18+} counterparts.

A useful technique to compare the relative shapes of the various charge exchange spectra is to calculate hardness ratios, \mathcal{H} , defined here as the intensity, I , ratio of all $n \geq 3 \rightarrow 1$ to $n = 2 \rightarrow 1$ transitions, i.e:

$$\mathcal{H} = \frac{\sum_{n=3}^{n_c} I_{n \rightarrow 1}}{I_{2 \rightarrow 1}}. \quad (4.11)$$

A survey of the hardness ratios calculated from the simulated spectra in

Figures 4.5 and 4.6 is presented in Figure 4.7. Solid lines connect the sets of data obtained for Ar^{17+} and Ar^{18+} from the spectra for E1 transitions only. Dashed lines connect the values obtained from the Ar^{18+} spectra for which E2, M1 and M2 transitions were also taken into account. The large hardness ratio corresponding to electron capture into the 8p-state of Ar^{18+} reflects the suppression of the $n = 2 \rightarrow 1$ transition, as discussed. The counter effect of including the electric dipole-forbidden transitions for this capture state is clearly seen. In contrast, the relatively small hardness ratio for capture into the 8p-state of Ar^{17+} is observed. The plot demonstrates that the hardness ratios for Ar^{18+} charge exchange are generally larger than the corresponding ratios for Ar^{17+} , in particular of course for capture into 8p. In addition, it becomes evident that the hardness ratios for capture into Ar^{18+} vary within a wider range than those for Ar^{17+} . This will prove to be a useful characteristic for the interpretation of the experimental results.

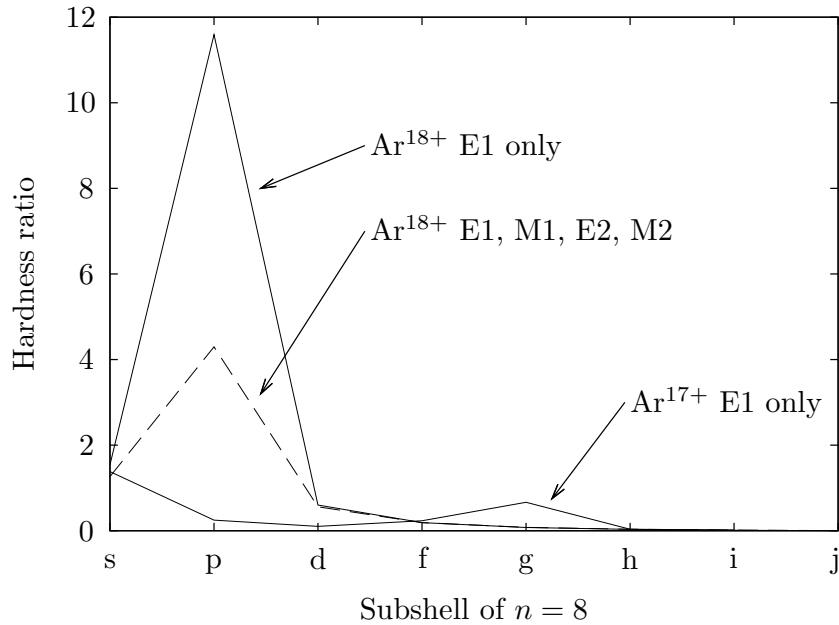
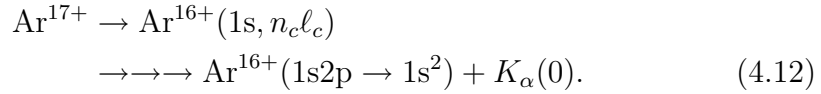


Figure 4.7: Hardness ratios versus capture state, obtained from the simulated x-ray emission spectra for single electron capture into Ar^{17+} and Ar^{18+} . Solid lines show the trend for the $\text{Ar}^{17+, 18+}$ results calculated with E1 transitions only and the dashed line marks the trend for the Ar^{18+} results for which E2, M1 and M2 transitions are also considered.

4.2 Multiple electron capture

In the simulations presented, radiative cascades resulting from single electron capture were considered. However, in interactions of slow HCIs with multielectron targets the amount of multiple capture, in particular double capture, can be significant [Ali et al., 1994; Greenwood et al., 2001] and wide variations in the ratio of autoionization to radiative stabilization have been measured [Martin et al., 1997]. With respect to the low energy $\text{Ar}^{17+,18+}$ -Ar collisions of interest here, the cross sections for single and double electron capture calculated from the widely used empirical relation in [Müller and Salzborn, 1977] are approximately $2 \cdot 10^{-14} \text{ cm}^2$ and $4 \cdot 10^{-15} \text{ cm}^2$, respectively, i.e. the cross section for double capture is around a fifth of that for single capture. The focus of this section is thus to consider the effect double electron capture could have on the charge exchange emission spectra recorded.

To recap, first for Ar^{17+} , single electron capture into a Rydberg state of the HCI is followed by a radiative cascade in which the final transition to the ground $1s^2$ state of the product Ar^{16+} ion results in the emission of a normal satellite K_α x-ray. This process can be written as:

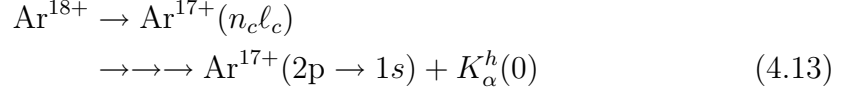


The triple arrows denote a series of cascade steps and the zero in $K_\alpha(0)$ indicates that there are no spectator electrons in higher ($n > 1$) shells. In the case of double electron capture, the second electron (if it is retained by the ion) generates an L -shell x-ray in its final cascade step, because the K -shell is then already fully occupied. Hence the investigations in the energy range of K -shell emission implemented here are insensitive to the final transition of Ar^{17+} double capture. For Ar^{18+} the situation is different, because both substates of the K -shell are initially vacant.

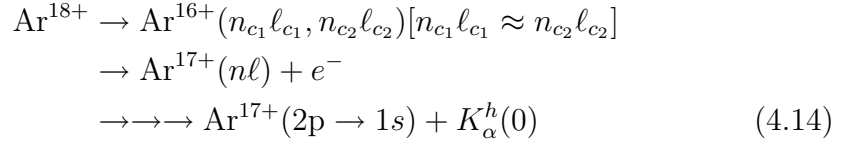
Recalling Ar^{18+} single electron capture, a hypersatellite K_α x-ray ($K_\alpha^h(0)$) is emitted at the end of the radiative cascade to the ground state, again without spectator electrons. Before discussing the effect double electron capture into Ar^{18+} could have on the K -shell emission, the modes by which it manifests need to be distinguished, i.e. either it occurs by what is known as symmetric double electron capture or by asymmetric double electron capture. In the former, two electrons enter states with very similar quantum numbers (i.e. $n_{c1} \ell_{c1} \approx n_{c2} \ell_{c2}$) and the doubly excited ion mainly stabilizes by autoionization [Stolterfoht et al., 1990]: One electron is ejected into the

continuum while the other electron cascades to the ground state. As a result the end of the cascade is essentially the same as that for single electron capture into Ar^{18+} , generating a $K_\alpha^h(0)$ x-ray. Strictly speaking, this process should be termed symmetric double electron transfer, as only one electron actually remains captured. In contrast, in asymmetric double electron capture one electron enters a much lower energy shell than the other (i.e. $n_{c1} \ll n_{c2}$). This electron then typically cascades to the ground state followed by the other, generating a $K_\alpha^h(1)$ and a $K_\alpha(0)$ x-ray, respectively [Martin et al., 1997]. The processes of single and double electron capture into Ar^{18+} can thus be summarized as:

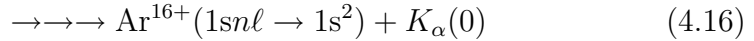
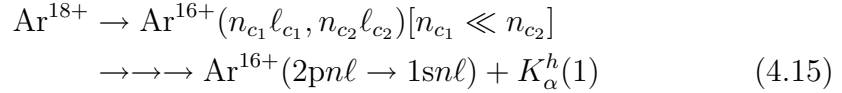
Single electron capture:



Symmetric double electron capture:



Asymmetric double electron capture:



The K -shell x-ray emission following asymmetric double electron capture into Ar^{18+} is therefore characterized by two K_α peaks separated in energy by ~ 200 eV; $K_\alpha(0) \approx 3.1$ keV and $K_\alpha^h(1) \approx K_\alpha^h(0) \approx 3.3$ keV. In contrast, emission alluding to symmetric double electron capture is more subtle, though it can be found as a result of the ejection process of one of the two electrons into the continuum. By energy conservation the remaining electron is demoted to a lower n -shell from which enhanced K -shell emission will then be observed. These emission features of double electron capture will be seen in the experimental charge exchange spectra presented in the next chapter.

Chapter 5

Results and Discussion

The results of the experimental studies of charge exchange by HCIs are now presented.

In Section 5.1 the focus is on the x-ray measurements of the radiative cascades following electron capture from gases. The results of the *in situ* magnetic trapping experiments are introduced by a discussion of the x-ray spectra obtained with and without the electron beam, from which estimates of the densities of ions and neutrals in the trap are inferred. Next the spectra obtained for various axial trap depths are presented and analyzed. This is followed by an analysis of the x-ray emission spectra recorded in the extraction experiments for a range of collision energies. The dependence of the angular momentum capture state on collision energy is investigated by means of hardness ratios calculated from the spectra. Finally the results of the *in situ* and extraction experiments are compared.

Section 5.2 is dedicated to the results of the investigation of electron capture by HCIs from surfaces. First an extension to the COB model introduced in Chapter 4 is used to describe HCI-surface charge exchange. Then the measurements made in the experiments using beams of low charge state ions are presented, followed by those using HCIs. COB model predictions of the percentage charge exchange on transport of the ions through the nanoscale apertures are compared with the experimental findings and the results are interpreted in terms of a capillary guiding mechanism.

5.1 Electron capture by HCIs from gases

5.1.1 X-ray emission from charge exchange in the EBIT

A scatter plot showing the time evolution of x-ray emission in a typical magnetic trapping experiment is presented in Figure 5.1. The data were recorded over 12500 electron beam on/off cycles. In the ionization phase, or EBM, the electron beam of the EBIT was set to an energy of 10.1 keV for a duration of 1 s. This allowed the production of all argon charge states up to the bare ion. The x-rays generated in the last 0.2 s of EBM were registered and give rise to the intense band of emission at the bottom of the figure. When the electron beam is on, the emission is mainly due to electron-ion collisions. Therefore, once the beam is switched off there is an abrupt decrease in x-ray intensity and the emission from charge exchange is unmasked. In the figure this much weaker emission during the 0.8 s of MTM is clear to see. The ratio of charge exchange to electron-ion collisions is determined to be $\sim 1\%$, which is calculated simply from the cross sections for charge exchange and electron impact ionization, the electron and ion velocities, and the densities of neutrals, ions and electrons in the trap. These data are given in Chapter 2 and further on in the present section. The percentage obtained is in good agreement with that calculated along similar lines elsewhere [Wargelin et al., 2005].

Plots of x-ray energy versus intensity are obtained by integrating the scatter data over time. For closer examination of the emission generated with and without the electron beam, this procedure has been implemented for the EBM and MTM portions of the scatter plot in Figure 5.1. The results are presented in Figures 5.2(a) and 5.2(b), respectively.

In Figure 5.2(a) the emission below the energy of the electron beam mainly results from direct excitation of HCIs by beam electrons, whereas above this energy the x-ray peaks result from the radiative recombination of beam electrons into HCIs. Some direct excitation of barium ions, which originate from the cathode of the electron gun, is visible, but the dominant excitation peaks come from the K_α , and to a lesser extent K_β , transitions of $\text{Ar}^{17+,18+}$ ions. Lower charge states of argon do not contribute to this signal as they lack the required K -shell vacancies. The main radiative recombination peaks, which have been magnified for clarity, are due to recombination into the K -shell of $\text{Ar}^{17+,18+}$ ions.

As mentioned, electron-ion collision cannot occur when the electron beam

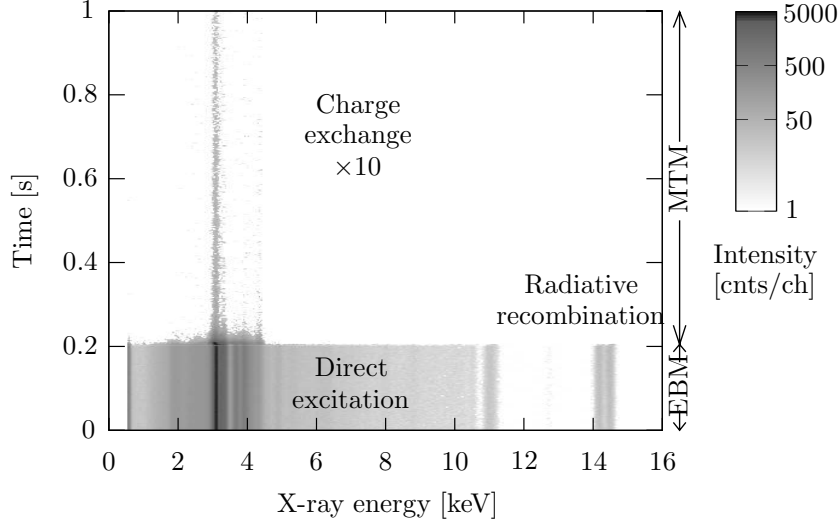
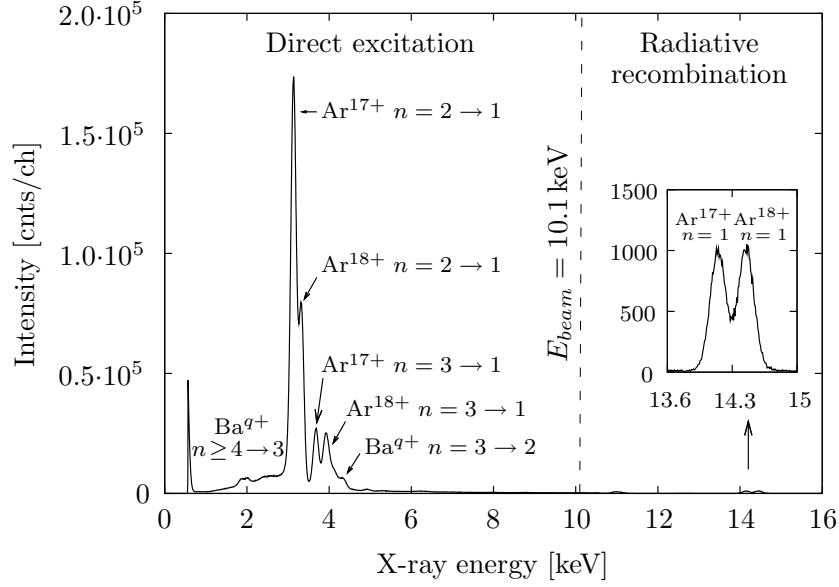


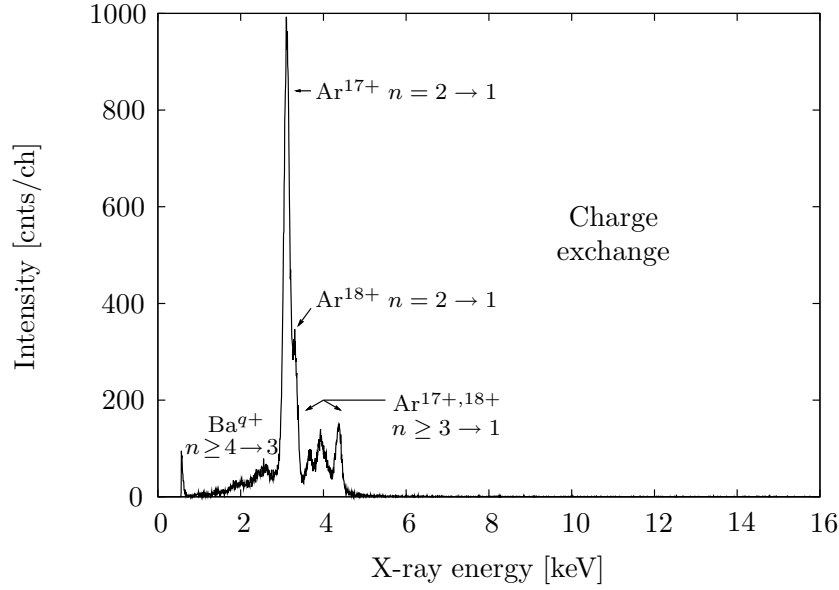
Figure 5.1: Time evolution of x-ray emission in a magnetic trapping experiment showing the photon events in 0.2 s of EBM (full ionization time 1 s) and 0.8 s of MTM. $V_a = 10.1$ kV, $I_e = 100$ mA and $V_{trap} = 100$ V.

is off, thus emission due to electron impact excitation and radiative recombination is absent in the MTM spectrum of Figure 5.2(b). The remaining emissions due to the radiative cascades following charge exchange with background gas in the trap are marked. It can be seen that the K_α peaks for capture into $\text{Ar}^{17+,18+}$ ions are again the most prominent. However, now the intensities of the higher $n \geq 3 \rightarrow 1$ transitions rise with increasing x-ray energy, whereas in Figure 5.2(a) their intensities tailed off. This is further evidence of charge exchange, because electron capture proceeds to higher n -levels than direct excitation, which mainly populates levels of lower n . In depth discussion of the $\text{Ar}^{17+,18+}$ charge exchange spectra is reserved for the subsequent pages.

Note that the x-ray emission in the MTM plot below 3 keV is attributed to cascade transitions into the $n = 3$ shell of highly charged barium ions and is thus neglected from the analysis which follows. Based on the EBM plot, however, it might be expected that a further emission band associated with charge exchange by barium ions, namely that due to $n = 3 \rightarrow 2$ cascade transitions of Ba^{q+} between 4 and 5 keV, could also be present in the MTM results. If this was the case, the intensity of the high energy emission from highly charged argon charge exchange in Figure 5.2(b) could be falsified.



(a) EBM



(b) MTM

Figure 5.2: X-ray spectra from EBM and MTM, with the peaks from direct excitation, radiative recombination (magnified) and charge exchange clearly visible. $V_a = 10.1$ kV, $I_e = 100$ mA and $V_{trap} = 100$ V.

However, only Ba^{q+} ions with a vacancy in the $n = 2$ shell, i.e. charge states $q \geq 47$, can give rise to $n = 3 \rightarrow 2$ cascade transitions. While an electron beam energy of 10.1 keV is sufficient to generate such charge states, there is no sign of emission from Ba^{q+} $n \geq 4 \rightarrow 2$ cascade transitions, which would appear between 6 and 8 keV. Hence it can be concluded that any Ba^{q+} ions with $q \geq 47$ were present in negligible amounts and thus any emission due to Ba^{q+} $n = 3 \rightarrow 2$ transitions overlapping with the high energy argon charge exchange peak is also negligible.

The emission from radiative recombination in EBM can be used to estimate the number of HCIs which are produced in each ionization cycle and are thus available for charge exchange in the magnetic trapping experiment. This is calculated here from the $n = 1$ recombination peaks for Ar^{17+} and Ar^{18+} in Figure 5.2(a), which have detected count rates, R_{RR}^{det} , of 12 and 12.5 photons per second, respectively, to within an error of less than one percent. Assuming 100% detector efficiency, the number density, n_{ion} , is given by:

$$n_{ion} = \frac{e}{l_{eff} I_e \sigma_{RR} \frac{d\Omega}{4\pi} W_{RR}} R_{RR}^{det}. \quad (5.1)$$

with the effective (visible) trap length $l_{eff} = 1.6$ cm, electron beam current $I_e = 100$ mA, detector solid angle $d\Omega = 4.2 \cdot 10^{-3}$ sr, cross section for radiative recombination σ_{RR} and angular correction factor W_{RR} . For an electron beam energy of 10 keV, the empirical relation in [Kim and Pratt, 1983] gives $\sigma_{RR, \text{Ar}^{17+}} = 1.1 \cdot 10^{-23} \text{ cm}^2$ and $\sigma_{RR, \text{Ar}^{18+}} = 3.0 \cdot 10^{-23} \text{ cm}^2$. The angular correction factor takes into account the anisotropy in the intensity of radiation emitted from ions recombining with electrons from the electron beam. It depends strongly on the electron beam energy, but is largely independent of ion species. For an observation angle of 90° to a 10 keV electron beam, $W_{RR} = 1.25$ is inferred [Fuchs et al., 1998]. Substituting these values into Equation 5.1 gives $n_{\text{Ar}^{17+}} = 2.6 \cdot 10^9 \text{ cm}^{-3}$ and $n_{\text{Ar}^{18+}} = 1.0 \cdot 10^9 \text{ cm}^{-3}$. From an effective trap volume of $6.2 \cdot 10^{-5} \text{ cm}^3$, determined assuming an electron beam diameter of $70 \mu\text{m}$ and using the effective trap length from above, it can be calculated that approximately $1.6 \cdot 10^5$ Ar^{17+} ions and $6.2 \cdot 10^4$ Ar^{18+} ions were available for charge exchange at the start of each magnetic trapping phase of the experiment.

For comparison it is useful to know the number of neutrals in the trap which serve as charge exchange partners for the HCIs. The pressure used for gas injection provides no indication of the amount which actually intersects the trap region. Direct measurement of the pressure is not possible, because

the ionization gauges are located in remote positions. Moreover, the gauges cannot detect the low pressures reached when the cryogenic pumping in the EBIT chamber comes into effect. An estimation can, however, be inferred from analysis of the decay of the x-ray signal observed in MTM. For this purpose an experiment with an extended magnetic trapping period of 20 s was implemented, with data accumulated over 1100 switching cycles. The results are presented in Figure 5.3, for which the x-ray intensity was integrated separately over the energy ranges of 2.9 to 3.2 keV and 4.3 to 4.6 keV. By choosing these ranges it is possible to distinguish the x-ray emission following charge exchange into Ar^{17+} and Ar^{18+} . The lower energy band corresponds to $n = 2 \rightarrow 1$ transitions for electron capture into Ar^{17+} and the higher energy band probes the $n \geq 4 \rightarrow 1$ transitions for capture into Ar^{18+} . Fitting exponential decay functions to each data set allows the mean MTM trapping lifetime, τ , for each ion charge state to be calculated. Values of $\tau_{\text{Ar}^{17+}} = 9.36$ s and $\tau_{\text{Ar}^{18+}} = 7.76$ s are obtained. The mean trapping lifetime of the bare ion is shorter, as the highest charge state has the largest cross section for charge exchange. Due to the fact that in MTM the dominant ion loss mechanism is charge exchange with background gas, the density of neutrals in the trap, n_{neutral} , can be estimated from:

$$n_{\text{neutral}} = \frac{1}{\tau \sigma_{CX} v_{\text{ion}}}, \quad (5.2)$$

where the denominator gives the average volume associated with a single interaction. Using the empirical formula in [Müller and Salzborn, 1977], values for the cross sections of $\sigma_{CX, \text{Ar}^{17+}} = 1.9 \cdot 10^{-14} \text{ cm}^2$ and $\sigma_{CX, \text{Ar}^{18+}} = 2.1 \cdot 10^{-14} \text{ cm}^2$ are derived. Estimating the kinetic energy of the ions in the trap using $0.2qV_{\text{trap}}$ (see Section 5.1.2) gives $v_{\text{Ar}^{17+}} = 4.0 \cdot 10^6 \text{ cm s}^{-1}$ and $v_{\text{Ar}^{18+}} = 4.2 \cdot 10^6 \text{ cm s}^{-1}$. Substituting into Equation 5.2 for each ion then returns a consistent estimate of the neutral density of $1.4 \cdot 10^6 \text{ cm}^{-3}$. Multiplying by the volume of the electron beam in the trap, as for the previous calculation for the number of ions, an estimate of 90 neutrals is obtained. Thus during standard EBIT operation the HCIs clearly outnumber the neutrals. In this case the neutrals were outnumbered by the $\text{Ar}^{17+, 18+}$ ions by a factor of $\sim 10^3$.

The neutrals are continuously replenished by the gas injector. Therefore as the magnetic trapping phase progresses, the rate of $\text{Ar}^{17+, 18+}$ charge exchange decreases according to the removal of these ions by electron capture. From the densities of ions and neutrals calculated, the rate of charge

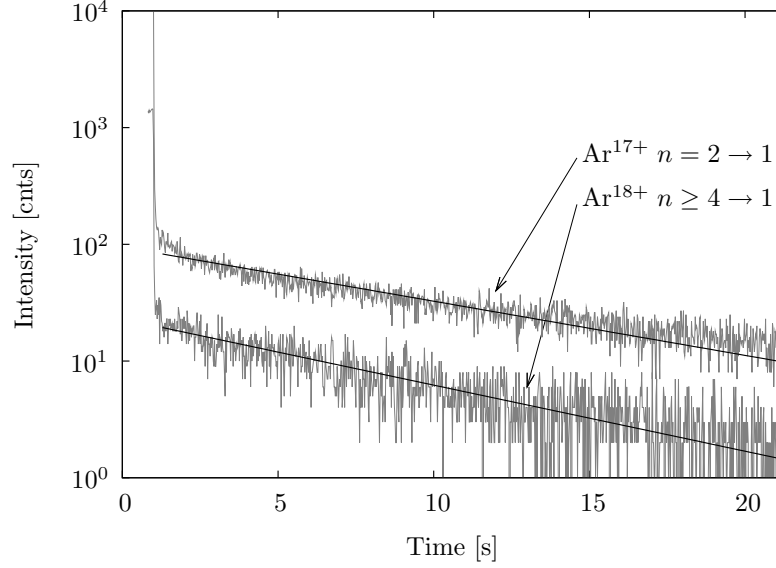


Figure 5.3: Intensity of x-ray emission in the energy ranges 2.9 to 3.2 keV and 4.3 to 4.6 keV, due to electron capture by Ar^{17+} and Ar^{18+} ions, respectively, as a function of time. The electron beam was switched off at 1 s to give 20 s of MTM. $V_a = 10.1$ kV, $I_e = 100$ mA and $V_{trap} = 100$ V.

exchange in the trap at the start of MTM can be estimating using:

$$\begin{aligned} R_{CX}^{trap} &= \sigma_{CX} v_{ion} n_{neutral} n_{ion} V \\ &= \frac{n_{ion} V}{\tau}, \end{aligned} \quad (5.3)$$

where τ is introduced into the second line from Equation 5.2 and V is the trap volume. For Ar^{17+} and Ar^{18+} this gives charge exchange rates of 17000 and 8000 s^{-1} , respectively, which are in good agreement with the rates inferred from the MTM photon count rates measured.

The full range of x-ray emission spectra recorded in the MTM experiments is now presented. In order to ensure that the data slices from the time-integrated scatter plots are completely free of photons emitted as a result of electron beam interactions in EBM, they were taken 10 ms after MTM began. This is well above the beam ramp down time of 4 ms. The spectra shown are all for the same magnetic trapping time of 0.8 s.

Figure 5.4 shows the outcome of the experiments with Ar^{17+} ions, for which Ar^{18+} ions were excluded by appropriate selection of the electron beam

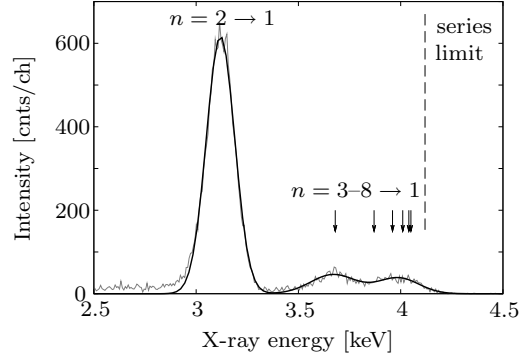
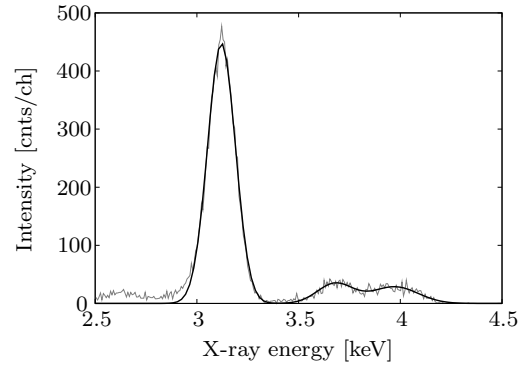
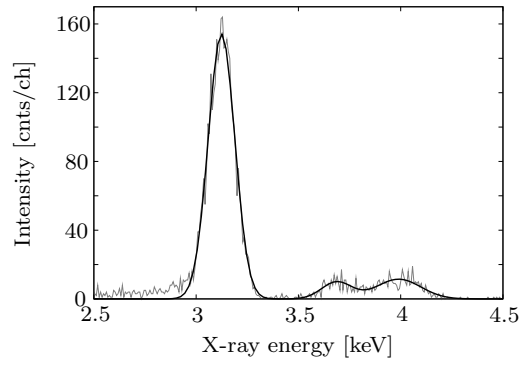

 (a) 700 V trap Ar^{17+}

 (b) 100 V trap Ar^{17+}

 (c) 30 V trap Ar^{17+}

Figure 5.4: X-ray emission spectra for charge exchange of Ar^{17+} ions in MTM for three different trap depths. Experimental data are plotted in grey and black curves represent the sum of Gaussian fits. $V_a = 4.3 \text{ kV}$ and $I_e = 70 \text{ mA}$.

energy in the ionization phase. Three axial trapping potentials were investigated, using $V_{trap} = 30, 100$ and 700 V. The experimental data are plotted in grey. In the given energy range the radiative transitions of electrons cascading into the K -shell following capture into Rydberg states are probed. The positions of these so-called normal satellite lines for Ar^{17+} are marked in Figure 5.4(a), together with the series limit. Photon emission from electron capture by lower charge state argon ions present in the trap does not mar the spectra, since for such ions the K -shell is fully occupied. Thus their emission is of a lower energy corresponding to transitions into the L - and M -shell. As discussed in Section 4.2, however, it is likely that in addition to single electron capture a significant amount of double capture occurred, though in contrast to the situation for double capture by Ar^{18+} , no evidence for this in the Ar^{17+} K -shell emission spectra will be found.

The principal charge exchange partner in the trap is the argon gas which is continuously injected into the chamber. However, electron capture from background gas, mainly nitrogen and oxygen, is also conceivable. These background gases are likely to enter the trap as a result of impure gas injection. Evidence for their presence can be found in charge state scans of extracted HCIs, as demonstrated in Figures 3.4 and 3.5. The ionization potential of molecular nitrogen (15.6 eV) is very close to that of argon (15.8 eV), so the COB prediction from Equation 4.7 for the principal quantum number of the dominant state in Ar^{17+} into which an electron is transferred remains at $n_c = 8$. Accordingly the distribution of ℓ_c -states should be very similar and thus significant differences in the radiative cascades are not expected. For molecular oxygen (ionization potential 12.1 eV) the COB model predicts $n_c = 9$, yet experiments investigating the target dependence of charge exchange x-rays indicate that the ionization potentials of argon and oxygen are still close enough not to significantly alter the relative intensities of the radiative emission peaks observed [Takács et al., 2007].

Fits to the Ar^{17+} spectra in Figure 5.4 are marked with black curves. Each comprises the sum of three Gaussian distributions corresponding to the $n = 2 \rightarrow 1$, $n = 3 \rightarrow 1$ and $n \geq 4 \rightarrow 1$ cascade transitions. The K_α peak at 3.1 keV is the most dominant, because the $n = 2$ level is populated by all the radiative cascades apart from those ending in the direct transitions $np \rightarrow 1s$ ($n \geq 3$). As discussed in Section 4.1, the latter are de-emphasized in Ar^{17+} charge exchange spectra as only singlet states can give rise to direct (Lyman) transitions into the ground state $n = 1$. The spectral shapes bear similarity to a comparable MTM measurement from the LLNL EBIT [Beiersdorfer

et al., 2000] and most closely resemble the simulated spectra for capture into 8d- and 8f-states (see Figure 4.6). A comparison based on hardness ratios will follow.

Analysis of the Ar^{18+} charge exchange spectra is more involved, because not only do those spectra result from radiative cascades following capture into the bare ion, but they also comprise a significant component arising from cascades associated with Ar^{17+} . The mixed $\text{Ar}^{17+,18+}$ spectra are presented in Figure 5.5. The detector resolution of 160 eV allows the two peaks at 3.1 keV (normal satellite emission) and 3.3 keV (hypersatellite emission), due to the $n = 2 \rightarrow 1$ cascade transitions for electron capture into Ar^{17+} and Ar^{18+} ions, respectively, to be resolved. Gaussian distributions fitted to the $n = 2 \rightarrow 1$ pair in each plot are marked with dashed lines. From the radiative recombination peaks in Figure 5.2(a), it is estimated that in the $\text{Ar}^{17+,18+}$ experiments there were between two to three times as many Ar^{17+} ions as Ar^{18+} ions in the trap at the start of MTM. The other source of normal satellite emission is the electron cascade in the second stage of asymmetric double electron transfer into Ar^{18+} , as discussed in Section 4.2.

In order to isolate the hypersatellite emission for electron capture into Ar^{18+} from the mixed spectra in Figure 5.5, the normal satellite contributions corresponding to capture into Ar^{17+} were subtracted out. This was achieved by using the $n = 2 \rightarrow 1$ peak at 3.1 keV in each mixed spectrum to generate a normalized Ar^{17+} fit for the same trap depth from Figure 5.4. First the $n = 2 \rightarrow 1$ peaks were matched and then the higher energy $n \geq 3 \rightarrow 1$ emission bands in the Ar^{17+} fits were scaled accordingly. The spectra resulting from the subtraction of each normalized Ar^{17+} fit from its respective mixed spectrum are presented in Figure 5.6. The counts below 3.1 keV, due to charge exchange of highly charged barium ions in the trap, are omitted.

Fits to the Ar^{18+} spectra were obtained similarly to those for the Ar^{17+} spectra, although four Gaussian peaks were fitted rather than just three. The additional peak, which is the smallest of the four, corresponds to $n = 4 \rightarrow 1$ transitions. In the Ar^{17+} spectra this peak is not individually resolved and falls within the $n \geq 4 \rightarrow 1$ emission band. The fit to this extra peak was facilitated by fixing its position to the theoretical value (4.15 keV) and its standard deviation to that obtained for the $n = 2 \rightarrow 1$ peak. For reference, the energies of the K -shell hypersatellite transitions, together with the series limit, are marked in Figure 5.6(a).

The main source of emission in the Ar^{18+} spectra is again the $n = 2 \rightarrow 1$ transition, but the relative intensity of the $n \geq 3 \rightarrow 1$ peaks is significantly

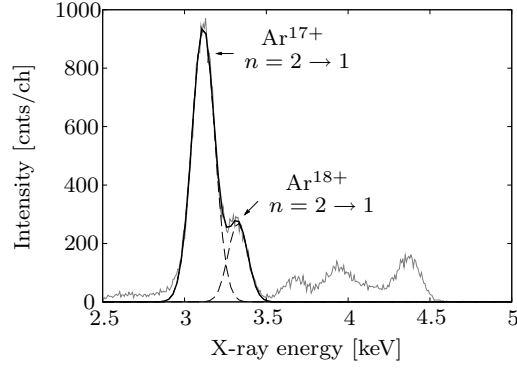
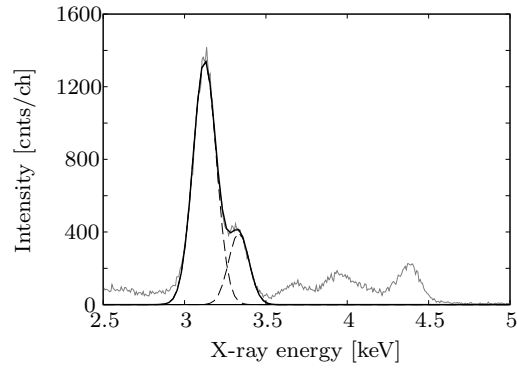
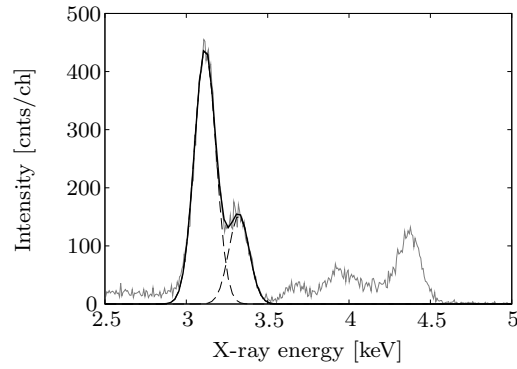

 (a) 700 V trap $\text{Ar}^{17+,18+}$

 (b) 100 V trap $\text{Ar}^{17+,18+}$

 (c) 30 V trap $\text{Ar}^{17+,18+}$

Figure 5.5: X-ray emission spectra for charge exchange of $\text{Ar}^{17+,18+}$ ions in MTM for three different trap depths. Experimental data are plotted in grey and dashed curves represent Gaussian fits to the $n = 2 \rightarrow 1$ cascade transitions for each charge state. $V_a = 10.1$ kV and $I_e = 100$ mA.

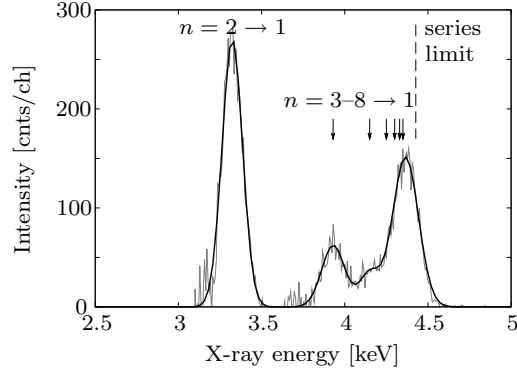
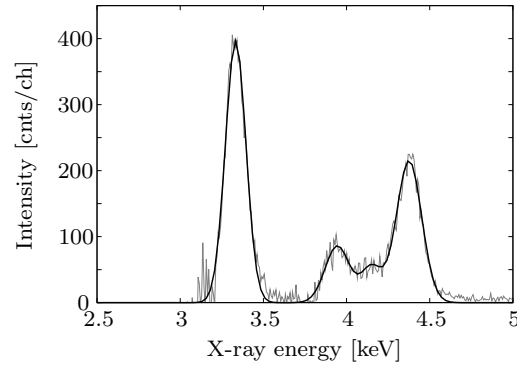
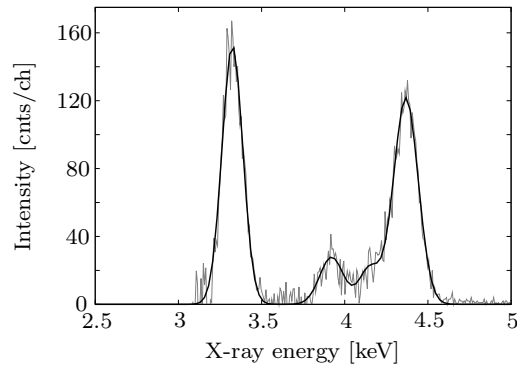

 (a) 700 V trap Ar^{18+}

 (b) 100 V trap Ar^{18+}

 (c) 30 V trap Ar^{18+}

Figure 5.6: X-ray emission spectra for charge exchange of Ar^{18+} ions in MTM for three different trap depths. Experimental data are plotted in grey and black curves represent the sum of Gaussian fits. $V_a = 10.1 \text{ kV}$ and $I_e = 100 \text{ mA}$.

greater than in the Ar^{17+} spectra (i.e. the hardness ratio is larger). Of the latter, the emission associated with the closely-lying $n \geq 5 \rightarrow 1$ transitions is the most prominent, indicating a high proportion of Lyman transitions from high np -states and consequently a high proportion of capture into np -states. The spectral shapes resemble the result of a similar MTM measurement made at the LLNL EBIT [Beiersdorfer et al., 2000], but there is not an obvious likeness to the simulated spectra for Ar^{18+} given in Figure 4.5. A possible explanation is that the simulations neglect double electron capture, which in the symmetric form will have the effect to increase the intensity of certain high energy peaks. This is due to the fact that when one of the two captured electrons is ejected into the continuum, the remaining electron is demoted into the highest excited level allowed by energy conservation. Using n' to denote the principal quantum number of the shell which the second electron enters after demotion, this gives $n' < n_c/\sqrt{2}$, which in the case of symmetric double capture into $n_c = 8$ gives $n' = 5$. Consequently an enhancement of $n = 5 \rightarrow 1$ emission could be expected, adding to the overall intensity of the $n \geq 5 \rightarrow 1$ emission band. This effect, albeit for different collision partners, has also been reported elsewhere [Rigazio et al., 2002; Beiersdorfer et al., 2003; Otranto et al., 2006]. Thus revisiting the simulated spectra with this enhancement of the high energy peak in mind, capture into 8d- and 8f-states, as in the Ar^{17+} case, becomes conceivable.

A further noticeable feature in the Ar^{18+} spectra is that the centroid of the high energy peak is ~ 20 eV higher than the theoretical energy of the $8p \rightarrow 1s$ transition. This suggests that capture predominantly occurs one or two shells higher than the COB model prediction of $n_c = 8$. The Ar^{18+} charge exchange spectra measured at LLNL show a similar shift [Beiersdorfer et al., 2000] and a slight underestimation of n_c by the COB model has also been reported elsewhere [Hasan et al., 2001].

In the same way that hardness ratios (the intensity ratio of $n \geq 3 \rightarrow 1$ to $n = 2 \rightarrow 1$ emission) are calculated from the simulated spectra in Section 4.1, they are obtained here to compare the experimental results for Ar^{17+} and Ar^{18+} charge exchange shown in Figures 5.4 and 5.6. Figure 5.7 shows the outcome, a plot of the hardness ratios calculated from the K -shell emission for each ion, against the axial trapping potential applied in the respective experiment. The error bars are Gaussian errors, determined from the accuracy of the fitted peak areas. A couple of MTM data points from [Beiersdorfer et al., 2000] for a trap depth of a 300 V are also plotted.

Within the accuracy of the measurements, the hardness ratios obtained

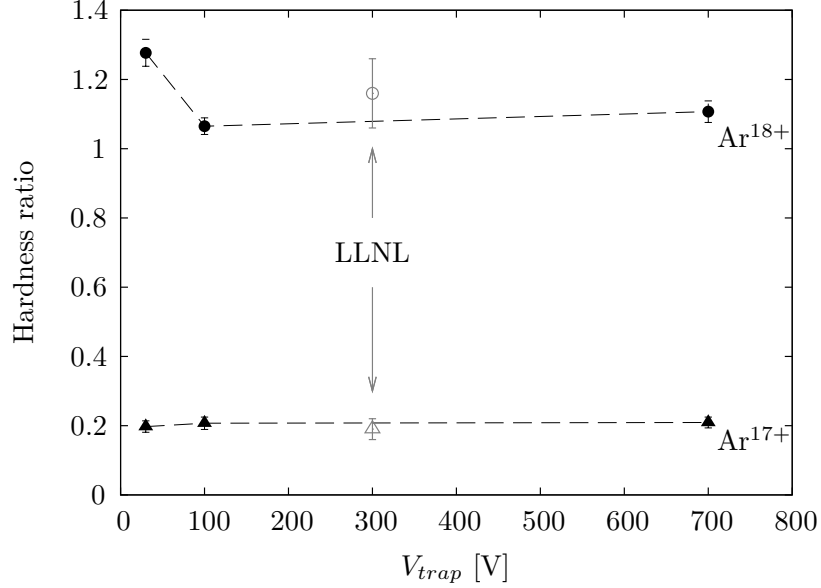


Figure 5.7: Dependence of hardness ratio on trap depth for Ar^{17+} and Ar^{18+} charge exchange in MTM. Data points from LLNL [Beiersdorfer et al., 2000] are plotted in grey.

for Ar^{17+} charge exchange appear independent of trap depth, taking values of ~ 0.2 . There is close agreement with the data from [Beiersdorfer et al., 2000]. Compared with the hardness ratios from the cascade simulations for Ar^{17+} in Figure 4.7, this correlates most closely to capture into a combination of 8p-, 8d- and 8f-states. However, as the hardness ratios from the Ar^{17+} simulations do not vary significantly with ℓ_c , comparison of the experimental hardness ratios for Ar^{17+} may not be that informative. In contrast, the experimental results from Ar^{18+} , for which the simulated spectra show marked differences, are expected to be more informative of any dependence of charge exchange on the trap depth implemented.

In the Ar^{18+} measurements using trap depths of 100 and 700 V, hardness ratios of ~ 1.1 are obtained. On comparing these data with the hardness ratios from the Ar^{18+} simulations this could indicate capture into a combination of 8s-, 8p- and 8d-states. The hardness ratio from the LLNL measurement for a 300 V trap [Beiersdorfer et al., 2000] is slightly higher, although as this data point has a relatively large error bar, it seems that in the range of trap depths between 100 to 700 V the hardness ratio remains fairly constant. For the measurement using a trap depth of 30 V, however, a hardness ratio of

~ 1.3 is obtained. Referring again to Figure 4.7, this increase could be indicative of a higher proportion of capture into 8p-states. As will be seen this might reflect the lower ion velocities expected for shallower traps. The relationship between axial trap depth and ion temperature in the EBIT is discussed towards the end of this section.

If the hardness ratio can be used to probe the conditions in the trap, then it is interesting to see whether the experimental hardness ratios vary over the duration of an MTM cycle. To investigate this, the results of the experiment using a magnetic trapping time of 20 s, presented near the beginning of this section, have been analyzed in more detail. The focus is on the Ar^{18+} hardness ratios, as these are much more sensitive to capture state than those for Ar^{17+} , as demonstrated in the simulations. Analysis of the x-ray emission in MTM was implemented in time groups, subtracting out the normalized Ar^{17+} components from each. The Ar^{17+} spectrum used for this purpose was that recorded using the same trap depth of 100 V, although only for 0.8 s magnetic trapping cycles, it being assumed that any change in Ar^{17+} hardness ratio over time will be negligible. Time groups of increasing length were chosen in order to compensate for the decreasing count rate. This keeps the errors in the fits roughly constant. The result of this study is presented in Figure 5.8, a plot of hardness ratio versus time for Ar^{18+} charge exchange in MTM. For comparison the data has also been analyzed using shorter time groups throughout and a similar trend in the hardness ratios, albeit with larger error bars, was obtained.

Compared with the total number of x-ray counts from the full duration of MTM, the number of counts contributing to each time group in Figure 5.8 is relatively small. Hence the fits for the time study are less accurate, giving rise to larger errors. However, the analysis does suggest that after switching off the electron beam the hardness ratio from Ar^{18+} charge exchange takes about half a second to stabilize, rising from a value of 1.1 to an average of ~ 1.4 . Note that as with all the MTM x-ray analysis, only data recorded more than 10 ms after the electron beam was switched off are considered, well above the ramp down time of 4 ms. An increase in hardness ratio indicates a decrease in collision energy, as will be revealed. Hence the indication is that after the electron beam is extinguished there is a sudden reduction in the temperature of the HCIs in the trap. This is due to the compromised ion trapping in the absence of the space charge of the electron beam, V_e , both radially and axially, as can be seen from Equations 2.2 and 2.3. Consequently once the electron beam is switched off the fastest ions quickly escape and the

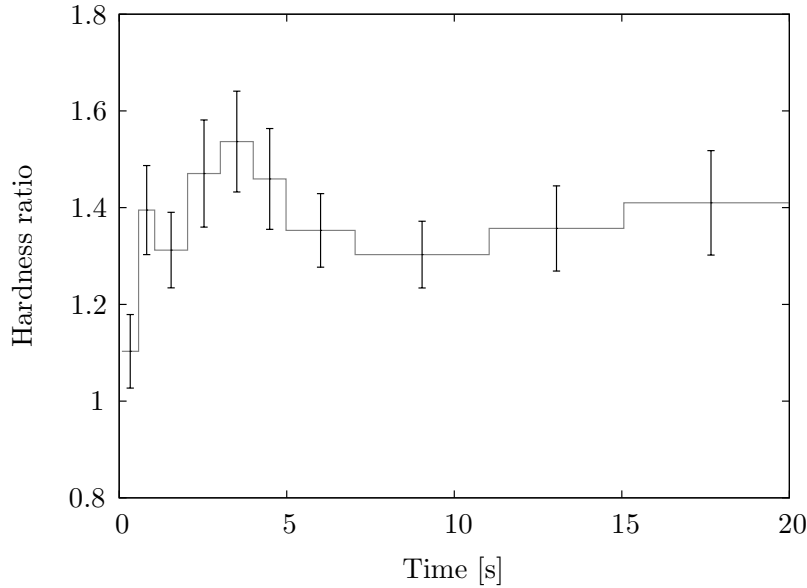


Figure 5.8: Hardness ratios for charge exchange of Ar^{18+} ions calculated in time groups for a 20 s MTM experiment. $V_a = 10.1 \text{ kV}$, $I_e = 100 \text{ mA}$ and $V_{\text{trap}} = 100 \text{ V}$.

remaining ion ensemble is cooled. From the results of this time study it would appear to be most appropriate to analyze MTM data only from the point that the hardness ratio stabilizes onwards. However, such a method would be at the expense of higher count rates, since in MTM the amount of HCIs in the trap decreases quite rapidly, as Figure 5.3 demonstrates. Alternatively, if the data at the beginning of MTM is included one should always compare time slices of the same duration, which is the method used in the analysis presented here.

5.1.2 X-ray emission from charge exchange at the gas target

The experiments using beams of HCIs extracted onto an external gas target enabled a more controlled investigation of charge exchange than the magnetic trapping experiments. It was possible to select the HCI velocity and vary it over a wide range via the retardation assembly in the beamline and the partner for charge exchange was determined by the gas species injected into the target region. X-ray emission spectra following charge exchange of

Ar^{17+,18+} ions with argon neutrals for projectile energies ranging from 5q keV ($\sim 6.5 \cdot 10^7 \text{ cm s}^{-1}$) down to 10q eV ($\sim 3 \cdot 10^6 \text{ cm s}^{-1}$) were obtained.

In Figure 5.9 the x-ray emission recorded for charge exchange of Ar¹⁷⁺ with argon for five projectile energies, 5040q eV, 515q eV, 70q eV, 50q eV and 10q eV, are presented. There is no emission from Ar¹⁸⁺ because the Wien filter was set to select Ar¹⁷⁺ ions only. Emission from lower charge states formed as a result of charge exchange in the beamline does not appear in the Lyman spectra due to the fully occupied *K*-shell of those ions, as discussed in the previous section. In the plots grey lines represent the experimental data and in Figure 5.9(a) the energies of the normal satellite x-rays together with the series limit are marked. Note that in the Ar¹⁷⁺ *K*-shell spectra any emission due to double electron capture cannot be distinguished from that due to single capture, as previously discussed.

Fits to the Ar¹⁷⁺ spectra are marked with black curves, each constituting three Gaussian distributions corresponding to the $n = 2 \rightarrow 1$, $n = 3 \rightarrow 1$ and $n \geq 4 \rightarrow 1$ transitions. The spectral shapes for the various collision energies are very similar. They bear close resemblance to the results of extraction experiments using 3q and 8q keV Ar¹⁷⁺ ions conducted elsewhere [Tawara et al., 2001, 2006]. In addition, there is close resemblance to the spectra from the MTM Ar¹⁷⁺ experiments shown previously, which compared favourably with the spectral shapes from the simulations for capture into 8d- and 8f-states. The extension of the fit in Figure 5.9(e) well beyond the series limit is thought to be due to the higher noise level in that measurement.

The x-ray emission spectra for the extraction experiments in which Ar¹⁸⁺ ions were selected for charge exchange at the target are shown in Figure 5.10. The projectile energies investigated were 4750q eV, 485q eV, 40q eV and 10q eV. In these spectra the dominant peak is much broader than in the Ar¹⁷⁺ extraction spectra, because in addition to comprising the hypersatellite $n = 2 \rightarrow 1$ peak from Ar¹⁸⁺ charge exchange at 3.3 keV, it is also composed of the normal satellite $n = 2 \rightarrow 1$ Ar¹⁷⁺ peak at 3.1 keV. The latter arises due to charge exchange in the beamline, causing Ar¹⁷⁺ ions to reach the target area despite charge selection by the Wien filter, and also as a result of asymmetric double electron capture. Hence as in the magnetic trapping experiments, the spectra recorded for Ar¹⁸⁺ ions extracted from the trap are marred by emission associated with Ar¹⁷⁺.

From the reverse bias measurement presented in Figure 3.7, it was estimated that 4 % of 4.8q keV Ar¹⁷⁺ ions charge exchanged to produce Ar¹⁶⁺ en route from the Wien filter to the gas target. The measurement was made

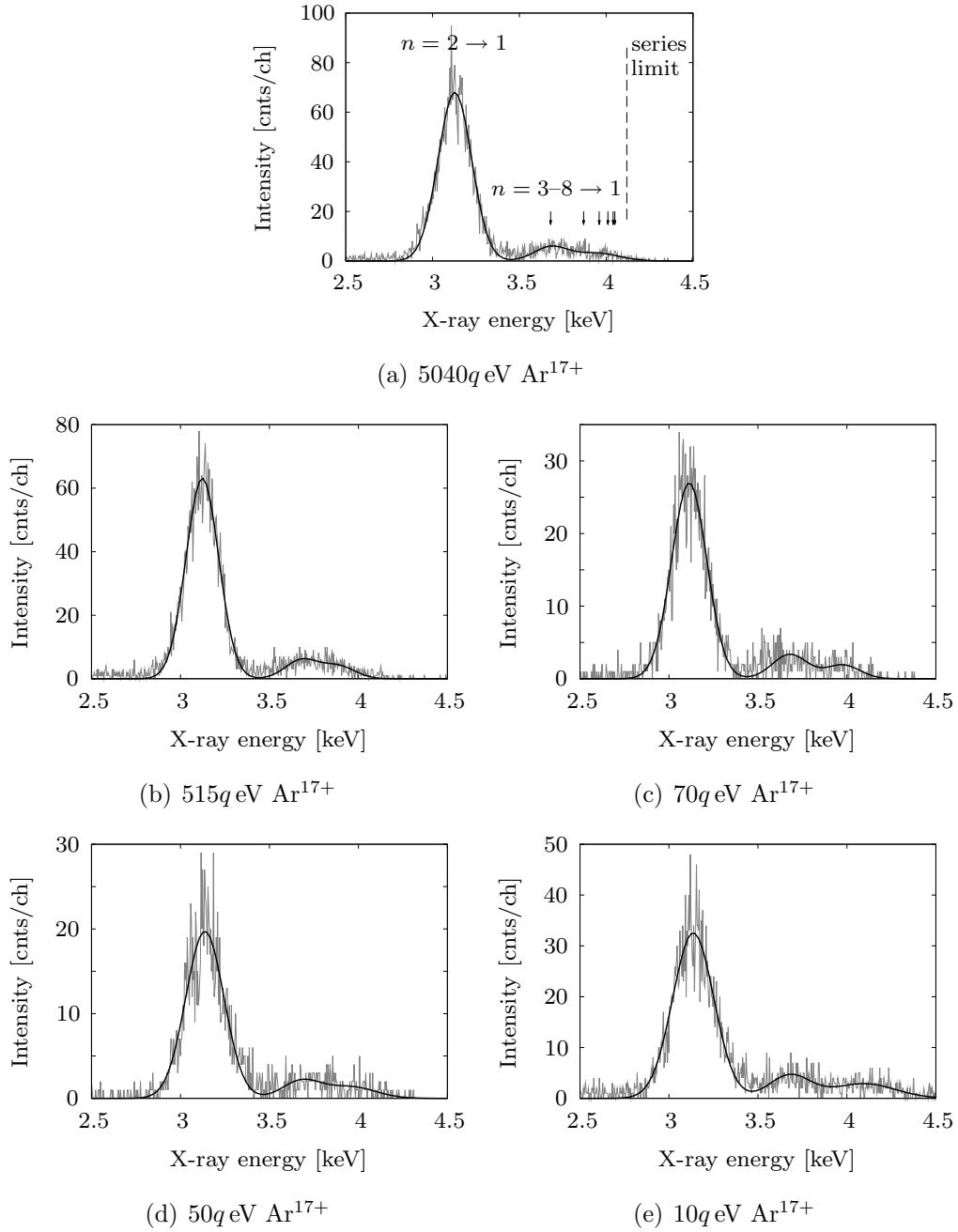


Figure 5.9: X-ray emission spectra for charge exchange of Ar^{17+} ions with an argon gas target for a range of projectile energies. Experimental data are plotted in grey and black curves represent the sum of Gaussian fits.

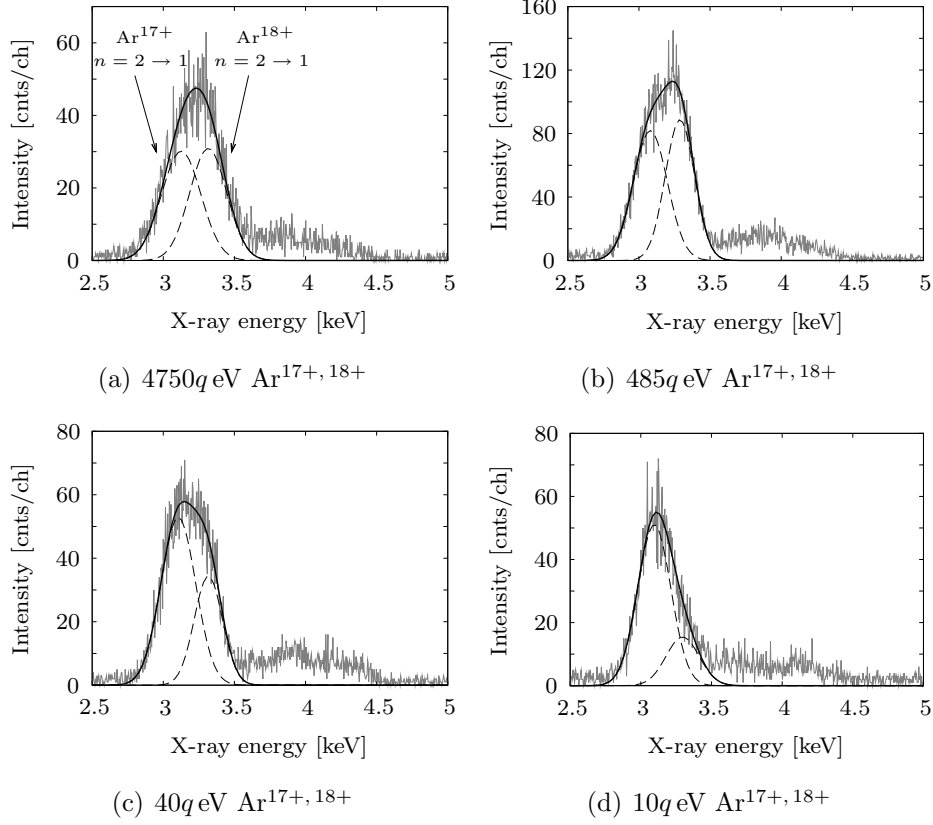


Figure 5.10: X-ray emission spectra for charge exchange of $\text{Ar}^{17+}, 18+$ ions with an argon gas target for a range of projectile energies. Experimental data are plotted in grey and dashed curves represent Gaussian fits to the $n = 2 \rightarrow 1$ cascade transitions for each charge state.

without gas pulsing into the target area, i.e. the pressure in the beamline was of the order of 10^{-5} Pa. Assuming a cross section for single electron capture of $\sigma_{CX} = 1.9 \cdot 10^{-14} \text{ cm}^2$ [Müller and Salzborn, 1977] and that $4 \cdot 10^4$ Ar^{17+} ions, N_{ion} , were extracted per pulse (calculated from the count rate measured on the MCPs assuming 50% detection efficiency), the rate of charge exchange can be estimated using:

$$R_{CX}^{beamline} = \sigma_{CX} v_{ion} n_{neutral} N_{ion}. \quad (5.4)$$

For an ion velocity of $v_{ion} = 6.5 \cdot 10^7 \text{ cm s}^{-1}$ and a neutral density of $n_{neutral} = 3.2 \cdot 10^9 \text{ cm}^{-3}$, this gives $R_{CX}^{beamline} = 1.6 \cdot 10^8 \text{ s}^{-1}$. The ions travel a distance

of 1.2 m from the Wien filter to the gas target, giving a flight time of $1.8 \mu\text{s}$. Thus the amount of charge exchange expected is $\sim 1\%$, which is in line with the experimental value and the findings for other EBIT beamlines [Schneider et al., 1991].

The normal satellite x-ray contributions to the broadened $n = 2 \rightarrow 1$ peaks in the spectra in Figure 5.10 are, however, significant. In fact, during the charge exchange experiments the beamline pressure actually rose above the base pressure, due to poor isolation of the pulsed gas jet from the main beamline section. Therefore the amount of charge exchange occurring before the target will have actually been higher than the value just quoted. The experimental setup did not allow the pressure at the gas target to be measured directly, but the target atom density can be estimated according to:

$$n_{\text{neutral}} = \frac{R_{CX}^{\text{target}}}{\sigma_{CX} l_{\text{target}} N_{\text{ion}}}. \quad (5.5)$$

This is very similar to Equation 5.4, except that in place of ion velocity, the effective length of the target as viewed by the x-ray detector, l_{target} , appears and N_{ion} enters as the number of ions pulsed per second. The viewing length of the detector is estimated from the geometry of the setup at 3.5 cm. Each single electron capture event gives rise to one K -shell x-ray photon, so the rate of charge exchange at the target can be estimated from the detected count rate and detector solid angle using $R_{CX}^{\text{target}} = \frac{4\pi}{\Omega} R_{CX}^{\text{det}}$. For Ar^{17+} , with $R_{CX}^{\text{det}} = 0.5 \text{ s}^{-1}$ and $\Omega = 2.6 \cdot 10^{-3} \text{ sr}$, this gives $R_{CX}^{\text{target}} \approx 2400 \text{ s}^{-1}$. From Equation 5.5, using $N_{\text{ion}} = 4 \cdot 10^4 \text{ s}^{-1}$ and the same value for σ_{CX} as before, the density of atoms at the target is estimated at $1.7 \cdot 10^{12} \text{ cm}^{-3}$. Converting to pressure, assuming a temperature of 298 K, this gives $7 \cdot 10^{-3} \text{ Pa}$, which is between two and three orders of magnitude higher than the beamline base pressure. Thus if, as a result of the gas jet pulses, the average pressure along the beamline rises by one order of magnitude, for instance, the percentage of ion beam charge exchange before the gas target, according to Equation 5.4, would rise from 1 % to $\sim 10\%$. Hence it can be concluded that charge exchange in the beamline prior to the target region can contribute significantly to the normal satellite emission in the Ar^{18+} measurements. The additional contribution of asymmetric double electron capture at the target will be discussed presently.

As an interlude it is interesting to consider the effect electron capture could have on the projectile velocity, i.e. whether HCIs which charge exchange in the beamline then reach the target with a different kinetic energy.

After the electron is transferred, there is a repulsion between the collision products, since they are then both positively charged. Due to energy conservation the electron is bound more strongly in the capture state of the projectile than it was in the target. The amount of kinetic energy gained can thus be calculated from the difference between these binding energies, which from Equation 4.4, using atomic units, gives:

$$\Delta E = \frac{q-1}{R_c}, \quad (5.6)$$

where q is the charge of the HCI and R_c is the critical capture distance, given by Equation 4.5 in Section 4.1. The validity of Equation 5.6 has been confirmed by energy gain spectroscopy measurements, as for example in [Hvelplund et al., 1985]. Calculating here for electron capture by Ar^{18+} from an argon atom, for which $R_c \approx 0.9 \text{ nm}$, a value of $\Delta E = 28 \text{ eV}$ is obtained. This is a relatively small amount compared with the ion's kinetic energy prior to charge exchange (180 eV for the slowest ions). Therefore any increase in the projectile energy as a result of charge exchange in the beamline can be neglected.

In order to extract the Ar^{18+} charge exchange components from the spectra in Figure 5.10, Gaussian distributions have been fitted to the two $n = 2 \rightarrow 1$ peaks in each plot (marked by dashed lines) and the corresponding normalized Ar^{17+} spectrum was then subtracted out. Thus the same technique as for the $\text{Ar}^{17+,18+}$ magnetic trapping spectra was implemented. Here the fitting of the two $n = 2 \rightarrow 1$ peaks is more challenging due to the poorer resolution of the x-ray detector in the beamline to that installed at the trap. The 10q eV spectrum was the most difficult of the four $\text{Ar}^{17+,18+}$ extraction spectra to fit. In this case the FWHM of the lower energy peak was obtained from the flank below 3.1 keV and the position of the higher energy peak was fixed to its theoretical value. The pairings of the spectra in Figures 5.9 and 5.10 used to obtain the Ar^{18+} charge exchange results are as follow: 4750q eV $\text{Ar}^{17+,18+}$ with 5040q eV Ar^{17+} , 485q eV $\text{Ar}^{17+,18+}$ with 515q eV Ar^{17+} , 40q eV $\text{Ar}^{17+,18+}$ with 50q eV Ar^{17+} and 10q eV $\text{Ar}^{17+,18+}$ with 10q eV Ar^{17+} . Figure 5.11 shows the outcome, with the experimental data plotted in grey.

The black curves in the Ar^{18+} spectra of Figure 5.11 mark fits, each the sum of three Gaussian distributions corresponding to the $n = 2 \rightarrow 1$, $n = 3 \rightarrow 1$ and $n \geq 4 \rightarrow 1$ transitions. The energies of the various transitions and the series limit are marked in Figure 5.11(a). To facilitate the fits, the

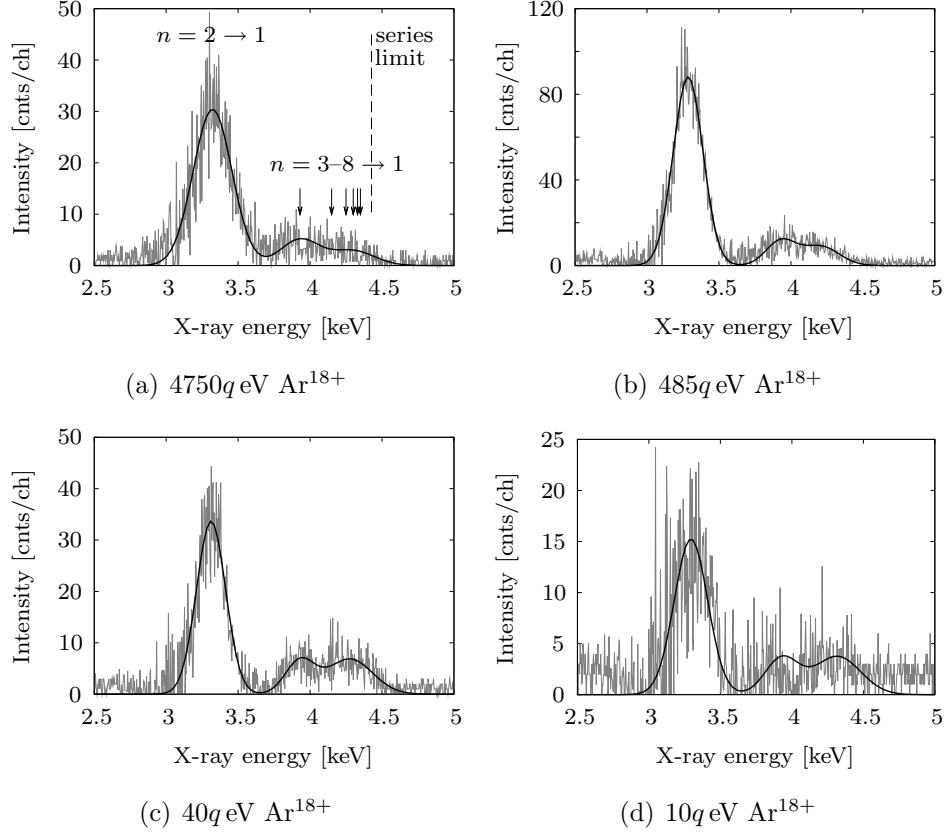


Figure 5.11: X-ray emission spectra for charge exchange of Ar¹⁸⁺ ions with an argon target for a range of projectile energies. Experimental data are plotted in grey and black curves represent the sum of Gaussian fits.

centroid of the $n = 3 \rightarrow 1$ peak was fixed to its theoretical value (3.93 keV) and the standard deviation to that obtained for the $n = 2 \rightarrow 1$ peak. In addition, for the 10q eV spectrum, which has the lowest signal-to-noise ratio, the standard deviation of these peaks was fixed to the value obtained from the Ar^{17+,18+} spectrum. Hence the apparent misfit in Figure 5.11(d).

The spectral shapes of the x-ray emission for 4750q eV and 485q eV Ar¹⁸⁺ ions resemble the spectrum obtained in a similar experiment conducted elsewhere for 8q keV Ar¹⁸⁺ ions [Tawara et al., 2006] and are also similar to the simulated spectra for capture into 8f- and 8g-states shown in Figure 4.5. In the 40q eV and 10q eV spectra, however, the proportion of $n \geq 3 \rightarrow 1$ emission is visibly higher, with the $n \geq 4 \rightarrow 1$ peak being about as intense as

the $n = 3 \rightarrow 1$ peak. This suggests a mixture of the spectra simulated for 8p and 8d capture. All the extraction spectra look very different from the Ar^{18+} MTM results, in which the emission from $n \geq 5 \rightarrow 1$ transitions was greatly enhanced.

Before comparing the sets of Ar^{17+} and Ar^{18+} charge exchange spectra, the relative intensities of the $n = 2 \rightarrow 1$ peaks in the mixed $\text{Ar}^{17+,18+}$ spectra of Figure 5.10, which are seen to vary strongly with the projectile energy, are investigated. For this purpose first the fraction of emission corresponding to $n = 2 \rightarrow 1$ transitions in the various Ar^{17+} and Ar^{18+} spectra of Figures 5.9 and 5.11, respectively, has been calculated, i.e. the intensity ratio of $n = 2 \rightarrow 1$ to $n \geq 2 \rightarrow 1$ transitions. Then by dividing the areas of the fitted $n = 2 \rightarrow 1$ peaks in Figure 5.10 by the respective fraction from above, i.e. for the corresponding energy and ion charge state, the ratios of the total amount of normal to hypersatellite K -shell emission in the mixed spectra were determined. The findings are presented in Figure 5.12, which shows a plot of this ratio against the centre-of-mass collision energy. In the laboratory frame the target argon atoms are effectively at rest, therefore the centre-of-mass collision energies are simply obtained by assuming a reduced mass of $m_{\text{Ar}}/2$. The error bars in the figure are calculated from the Gaussian errors in the areas of the fitted peaks and from the FWHM values of the reverse bias measurements of the projectile energies described in Section 3.2.3.

The figure shows a clear energy dependence of the ratio of normal to hypersatellite K -shell emission in the Ar^{18+} experiments. For the experiment using non-retarded Ar^{18+} ions, the ratio is about unity. If the normal satellite x-rays only resulted from electron capture by Ar^{17+} ions, which arrived at the target due to Ar^{18+} charge exchange after the Wien filter, this would mean that in the experiment the amount of beamline charge exchange was $\sim 50\%$. This seems very high, although from the previous discussion of beamline charge exchange a percentage of the order of 10%, due to streaming of the gas out of the target area, was estimated. For decreasing collision energies, however, the ratio increases, reaching a value of 2.7 for the slowest ions investigated. While the rate of charge exchange in the beamline is velocity dependent, the total amount of beamline charge exchange is not, since one has to multiply the rate by the flight time, i.e. the velocity cancels. Consequently, the reason for the different ratios of normal to hypersatellite K -shell x-rays cannot be attributed to varying amounts of charge exchange in the beamline.

Alternatively it is proposed that a significant amount of the hypersatellite x-rays results from asymmetric electron capture by the Ar^{18+} ions at the

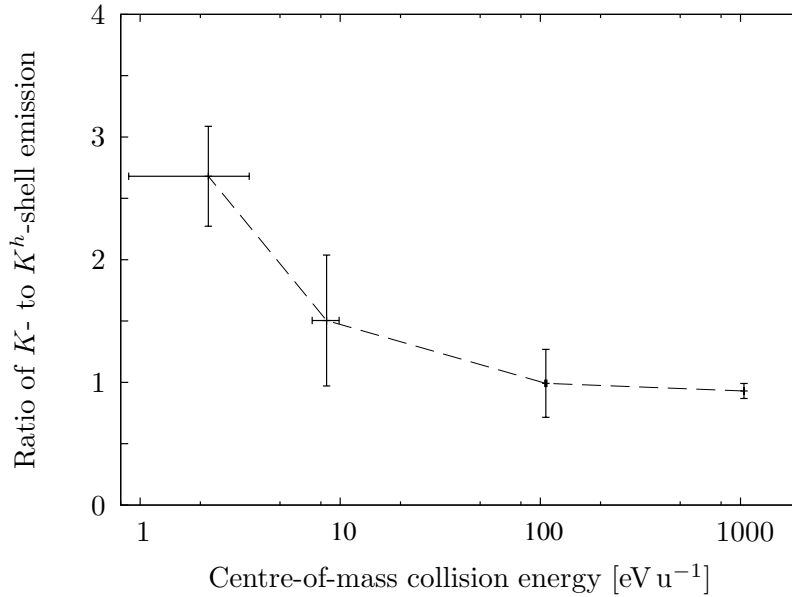


Figure 5.12: Ratio of normal to hypersatellite K -shell emission from the mixed $\text{Ar}^{17+}, 18+$ spectra of Figure 5.10 versus centre-of-mass collision energy.

target and that the velocity dependence of the cross sections for single and double electron capture come into play. In work conducted elsewhere for collision energies below 10 keV u^{-1} , it has been found that while the cross sections for symmetric (autoionizing) double electron capture are relatively independent of collision energy, those for asymmetric double capture increase strongly with decreasing impact energy [Chesnel et al., 1998]. In contrast, below 100 eV u^{-1} the cross sections for single electron capture *decrease* with decreasing impact energy and at higher energies remain roughly constant [Nielsen et al., 1984]. If the increase in the cross section for asymmetric double electron capture is greater than the decrease in the value for single electron capture, then the trend observed in Figure 5.12 can be understood on the basis of the cross section velocity dependencies discussed.

The various Ar^{17+} and Ar^{18+} x-ray emission spectra from the extraction experiments are compared by the same method used for the magnetic trapping spectra in Section 5.1.1, i.e. by calculating hardness ratios. Figure 5.13 shows the result, a plot of hardness ratio versus the centre-of-mass collision energy. Solid black triangles and circles represent the results for the charge exchange of Ar^{17+} and Ar^{18+} ions, respectively. The ion collision energy is given in electronvolts per atomic mass unit, with error bars calculated from

the FWHM values obtained from the reverse bias measurements. A scale showing the relative collision velocity in atomic units, i.e. as a fraction of the Bohr velocity, is also shown. The error bars for the hardness ratios are Gaussian errors determined from the uncertainty in the fitted peak areas. Selected data from the MTM experiments are also plotted and are compared with the extraction results in the next section.

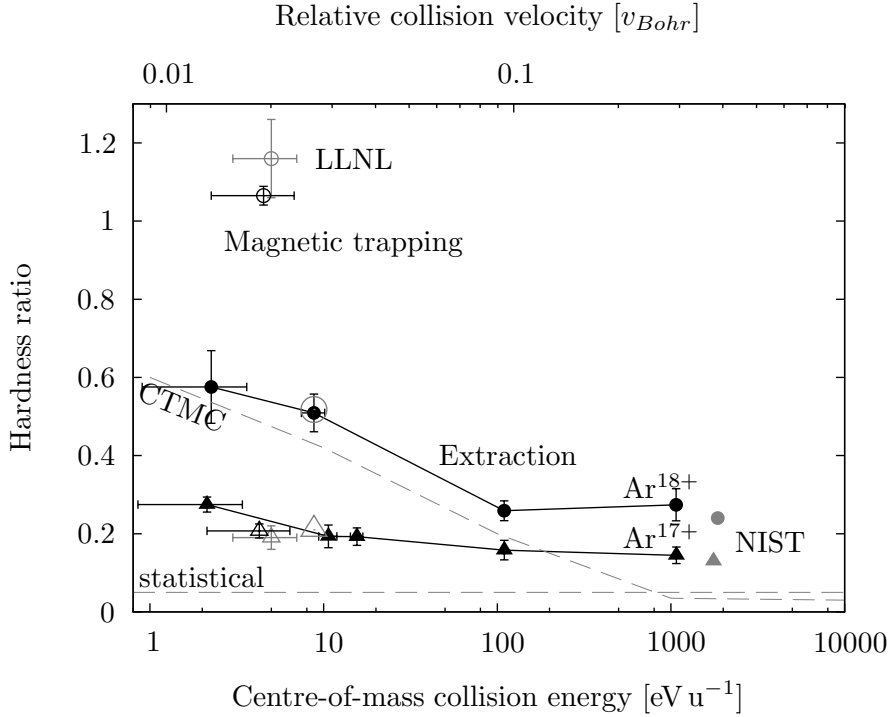


Figure 5.13: Dependence of hardness ratio on the centre-of-mass collision energy for charge exchange of Ar^{17+} and Ar^{18+} with argon. Solid and hollow black symbols represent the results of the extraction and magnetic trapping experiments, respectively. Grey symbols show extraction and magnetic trapping measurements made by NIST [Tawara et al., 2006] and LLNL [Beiersdorfer et al., 2000]. CTMC results for single electron capture into Ar^{18+} from a hydrogen target [Beiersdorfer et al., 2000] and the hardness ratio predicted on the grounds of statistical assumptions are marked with dashed lines. CTMC predictions for single electron capture into Ar^{17+} and Ar^{18+} from an argon target for a collision energy of 8.8 eV u^{-1} are plotted using large light grey open symbols [Otranto, 2006].

In high energy collisions electrons tend to populate the initial capture states according to their statistical weights, or j degeneracy, i.e. the ℓ_c -state with the maximum probability for capture is $\ell_c = n_c - 1$. Thus for high energy $\text{Ar}^{17+,18+}$ charge exchange, assuming $n_c = 8$, capture into the 8j-state is most likely. Capture into a high ℓ_c -state results in a small hardness ratio, because then the radiative cascade predominantly follows the Yrast chain ending with the transition $n = 2 \rightarrow 1$. The principal contribution to $n = n_c \rightarrow 1$ decay will be radiative cascades following capture into the $\ell_c = 1$ (p) state. As a result, an estimate of the hardness ratio for a high energy collision based on statistical assumptions can be obtained from the fractional population of the p -subshell of n_c , calculated from the state degeneracies:

$$\begin{aligned} \mathcal{H}_{\text{statistical}} &\approx \frac{2\ell_c + 1 |_{\ell_c=1}}{\sum_{\ell_c=0, \ell_c \neq 1}^{n_c-1} (2\ell_c + 1)} \\ &\approx \frac{3}{n_c^2 - 3}. \end{aligned} \quad (5.7)$$

For cascades in $\text{Ar}^{17+,18+}$ this gives $\mathcal{H}_{\text{statistical}} \approx 0.05$, which is marked in the figure by the horizontal dashed line. Note that the statistical hardness ratio is not the high energy limit. This is because the cross section for charge exchange, which remains roughly constant at low energies, decreases for high collision energies and a broader band of lower n -levels becomes populated [Janev and Winter, 1985].

The experimental hardness ratios from the extraction experiments vary significantly with collision energy, particularly in the case of Ar^{18+} charge exchange. Hence it can be concluded that the collisions were slow enough for non-statistical population of ℓ_c -states to occur. Furthermore, the trend is for hardness ratio to increase with decreasing collision energy, indicating that in slower collisions capture into lower ℓ_c -states is favoured, i.e. for lower collision energies there is a higher proportion of capture into np -states, resulting in the direct $np \rightarrow 1s$ cascade transitions which give the larger hardness ratio measured.

The experimental hardness ratios for Ar^{18+} charge exchange are consistently higher than the corresponding values for Ar^{17+} and the increase in the ratio with decreasing collision velocity is more marked for Ar^{18+} . This can be explained by reference to the hardness ratios obtained from the simulated spectra presented in Figure 4.7. There it is seen that in general, the Ar^{18+} hardness ratios for capture into the various ℓ_c -states are higher than their Ar^{17+} counterparts, especially for low ℓ_c , and that the hardness ratios for

Ar^{18+} vary over a wider range. A larger hardness ratio for Ar^{18+} than for Ar^{17+} charge exchange can also be inferred from the x-ray emission spectra obtained by the NIST EBIT group in similar experiments using non-retarded Ar^{17+} and Ar^{18+} ions incident on an external argon gas target [Tawara et al., 2006]. Data points from the latter are plotted in Figure 5.13 using solid grey triangles and circles, respectively, and lie in the range of the data obtained using the non-retarded ions in this work.

Data from experiments investigating different collision energies are limited and mainly concentrate on high energy collisions ($>1 \text{ keV u}^{-1}$), for which only a slight energy dependence of hardness ratio has been reported [Tawara et al., 2001]. Thus the work presented here constitutes the first detailed experimental survey of the energy dependence of ℓ_c -selective electron capture in low energy HCI-gas collisions. The basic trend observed supports theoretical work based on CTMC simulations of charge exchange [Olson, 1981]. In the CTMC method Hamilton's equations of motion are solved numerically for three-dimensional trajectories of the three bodies involved. For example, for a bare ion colliding with atomic hydrogen, the three bodies would be the ion, the active electron and the hydrogen nucleus. The forces between the three bodies are Coulombic, and for the start of each trajectory the impact parameter of the projectile ion together with the position and momentum of the electron orbiting the target nucleus are randomly selected using the Monte Carlo method. After the completion of each trajectory the system is tested to see if the electron is now orbiting the projectile ion. If the electron has been captured, its binding energy and orbital angular momentum are calculated, from which quantized n_c - and ℓ_c -values, respectively, are assigned. Subsequently the radiative cascade of the captured electron is simulated using a decay matrix for hydrogenic ions.

The results of CTMC calculations for single electron capture into Ar^{18+} from a hydrogen gas target over a range of collision energies [Beiersdorfer et al., 2000] are plotted in Figure 5.13 using a dashed grey line. (Note that the scale for the relative collision velocity at the top of the figure does not apply to these results, as the collision partners now have different masses.) The theoretical hardness ratios given are actually for the ratio of $n \geq 4 \rightarrow 1$ to $n = 2 \rightarrow 1$ emission, therefore the true hardness ratios, which also include $n = 3 \rightarrow 1$ emission, will be higher. Moreover, capture from an argon target as opposed to the hydrogen target used in the calculations proceeds to slightly lower n -levels (see Equation 4.7). This will also increase the hardness ratio due to a smaller range of possible ℓ_c -states, which leads to a larger

proportion of captured electrons entering np -states. Indeed, the experimental data points for Ar^{18+} are consistently higher than the CTMC predictions from [Beiersdorfer et al., 2000]. The results of CTMC calculations for Ar^{18+} and Ar^{17+} ions from [Otranto, 2006] for a collision energy of 8.8 eV u^{-1} , which state the true hardness ratio and consider an argon target, are in very close agreement with the experimental results from the extraction experiments. These data points are plotted using large light grey open symbols.

An apparent difference between the experimental results and the CTMC predictions in [Beiersdorfer et al., 2000] is that the CTMC calculations predict that collision energy starts to have an effect on hardness ratio when decreased below 1 keV u^{-1} , whereas the experimental data suggest that the critical point is actually several 100 eV u^{-1} lower.

5.1.3 Comparison of the *in situ* and extraction results

Selected data from the magnetic trapping measurements have been added to Figure 5.13 for comparison with the extraction results. They are plotted using an open black circle and triangle representing charge exchange of Ar^{18+} and Ar^{17+} ions, respectively, and correspond to the MTM experiments in which an axial trap depth of 100 V was implemented. The temperature of the HCIs in the trap is a function of the axial trapping potential and can be estimated according to the empirical relation:

$$T_{ion} = 0.2qV_{trap}, \quad (5.8)$$

which gives the ion temperature in electronvolts [Currell and Fussmann, 2005]. The centre-of-mass collision energies are again calculated assuming that the velocity of the target argon atoms in the laboratory frame is zero. For the data points plotted, an error in the estimated collision energies of 50% is assumed. Data from LLNL magnetic trapping measurements using a trap depth of 300 V are plotted using open grey symbols [Beiersdorfer et al., 2000]. The ion temperatures in the latter are assigned on the basis of high resolution x-ray measurements of Doppler line broadening due to the thermal motion of the ions in the trap [Beiersdorfer et al., 1996c; Beiersdorfer, 1997]. It should be noted that it is not clear whether the duration of magnetic trapping in the LLNL experiments was always the same. If different timing patterns were used, this could have had an effect on the hardness ratio measured, as the results presented in Figure 5.8 show.

While the Ar^{17+} magnetic trapping data lie close to the Ar^{17+} extraction results, this is far from the case for Ar^{18+} . From the Ar^{18+} extraction data it can be seen that for the lowest collision energy of 2.2 eV u^{-1} the hardness ratio takes a value of 0.58, whereas the Ar^{18+} magnetic trapping data point at 4.5 eV u^{-1} corresponds to a hardness ratio of almost double that, of 1.07. Larger hardness ratios are indicative of capture into lower ℓ_c -states and slower collision velocities, as discussed. Thus the question arises, whether the collision energy inferred from the empirical relation for ion temperature in the trap, which is for standard operation with the electron beam switched on, is an overestimation. Consideration of the ion cooling which occurs as a result of the reduced trapping in MTM, described towards the end of Section 5.1.1, supports this line of argument. However, according to CTMC calculations for capture into Ar^{18+} , hardness ratios of the order of unity and above are never reached. Instead, for collision energies below 1 eV u^{-1} , they level out to a plateau [Otranto, 2006]. Therefore an incorrect assignment of the collision energy in the trap does not appear to account for the discrepancy between the MTM and extraction results and an alternative explanation is sought.

An obvious difference between the conditions at the external gas target compared to those in the trap is the presence of the 3 T magnetic field in the latter. To investigate the effect of such a field on an electron captured into a Rydberg state of a HCI, it is instructive to calculate the magnetic force on that electron and to compare this with the electrostatic Coulomb force of attraction due to the HCI's nucleus. Considering an electron in the $n = 8$ shell of Ar^{18+} , for which the Bohr model predicts a velocity of $5 \cdot 10^8 \text{ cm s}^{-1}$, a maximum value for the magnetic force of the order of 10^{-12} N is obtained. In contrast, the Coulomb force on this electron is much higher, of the order of 10^{-7} N . As a result the 3 T magnetic field is not expected to influence the bound electrons in the trap. However, it is conceivable that when the electron has reached the potential maximum between the potential wells of the HCI and target just prior to capture, the magnetic force could then have an effect on its momentum and thus also on ℓ_c . To test this, MTM experiments with the EBIT operated at fields down to 1 T have been carried out, but a change in the hardness ratio was not measured. There is of course also the electrostatic field in the trap due to the voltages applied to the drift tubes. However, this is of the order of 10^4 Vm^{-1} , hence would only result in an electrostatic force on the electron of the order of 10^{-15} N , which is even lower than the magnetic force just discussed.

A further disparity between the two experimental techniques is that while

the HCIs in the trap remain in the viewing range of the x-ray detector for several seconds (see Figure 5.3), the extracted HCIs pass through the viewing range of the x-ray detector in the beamline in a fraction of that time. Therefore it is important to compare the distance traveled by an ion during the radiative cascade, with the viewing length of the detector. The time taken for an electron to cascade via electric dipole-allowed transitions from a Rydberg state to the ground state is of the order of picoseconds [Fritzsche, 2003]. Calculating for the fastest ions investigated ($6.5 \cdot 10^7 \text{ cm s}^{-1}$), the distance traveled before the cascade ends is of the order of micrometres. With a detector viewing length of 3.5 cm it can be concluded that the *K*-shell x-ray photons emitted at the end of such cascades are well within detection range. In contrast, for electron capture into Ar^{17+} the cascading process efficiently feeds the metastable $1s2s \ ^1S_0$ (singlet) and $1s2s \ ^3S_1$ (triplet) states, which have lifetimes of the order of a few hundred nanoseconds [Tawara et al., 2001] corresponding to an ion flight distance of a number of centimetres. Consequently these metastable states, which are thought to receive a considerable proportion of the cascading electrons [Tawara et al., 2001], will decay beyond the range of photon detection. Thus it could be expected that the MTM hardness ratios, which will include metastable decay, are lower than the ratios obtained for Ar^{17+} charge exchange at similar energies in the extraction experiments. In Figure 5.13 the MTM hardness ratios for Ar^{17+} are indeed found to be slightly lower than their extraction counterparts. However, as the real discrepancy is in the results for Ar^{18+} charge exchange, where the aforementioned metastable states do not arise, an argument based on detector viewing ranges does not clarify the situation either.

To summarize, the cause of the much higher hardness ratios measured for Ar^{18+} charge exchange in the magnetic trapping experiments compared to those obtained using the extraction setup remains unclear. The experimental results suggest a difference in the conditions of the EBIT environment compared with those of an external gas target, and a detailed theoretical treatment of the problem is required. Conclusions are drawn in Chapter 6.

5.2 Electron capture by HCIs from surfaces

The results of the HCI-surface charge exchange experiments are analyzed using a modified form of the COB model introduced in Chapter 4. The extended model focuses on electron capture by HCIs from metal surfaces [Burgdörfer et al., 1991] and is now described.

As in the HCI-atom case, electrons are transferred resonantly from the target into Rydberg states of the HCI. However, with a metal surface as the target the active electron experiences a superposition of three Coulomb potentials, rather than just two. These three potentials are due to the image charge of the electron on the metal, the charge of the HCI and the image charge of the HCI on the metal. Hence the potential experienced by the electron, using atomic units, becomes:

$$U(z) = -\frac{1}{4|r|} - \frac{q}{|R-r|} + \frac{q}{|R+r|}, \quad (5.9)$$

where r is the electron-surface distance, R is the HCI-surface distance and q is the charge on the HCI. For $q \gg 1$, the potential maximum between the surface and the HCI, which determines the barrier to charge exchange, is then given by:

$$U_{max} \simeq -\frac{\sqrt{2q}}{R}. \quad (5.10)$$

Electron transfer becomes classically allowed once, on approach of the HCI towards the surface, the potential maximum dips below the Fermi level of the metal. This is represented schematically in Figure 5.14. The condition for capture can be written as:

$$|U_{max}| \leq W_{\Phi}, \quad (5.11)$$

where W_{Φ} is the work function of the metal, i.e. the binding energy of the electrons. As in the HCI-atom case, electron transfer via quantum mechanical tunneling is neglected, due to the comparatively long timescales involved.

Substituting Equation 5.10 into Equation 5.11 and approximating using $q \gg 1$, the following relation for the critical distance for electron capture is derived:

$$R_c \simeq \frac{\sqrt{2q}}{W_{\Phi}}. \quad (5.12)$$

Charge transfer of the weakly bound conduction band electrons is thus estimated to set in at relatively large distances of a few nanometres from the

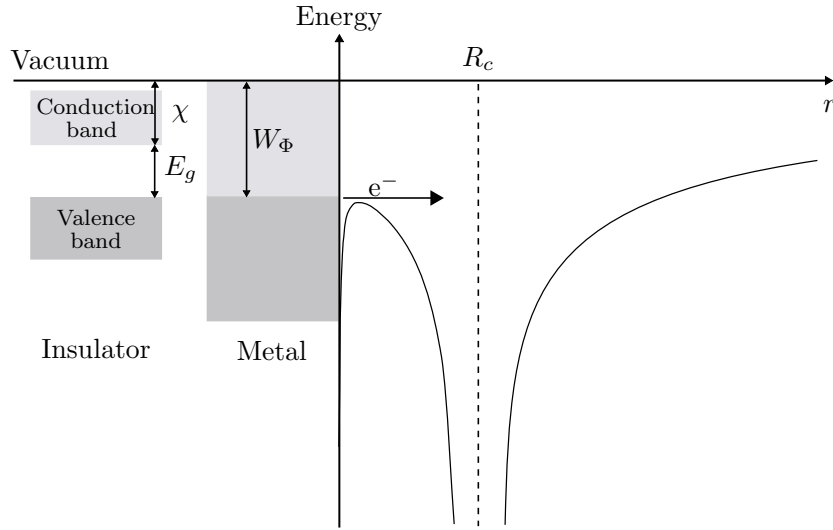


Figure 5.14: Electrostatic potential experienced by an active electron at the critical distance R_c for electron capture by a HCI from a metallic surface with work function W_Φ . For comparison the band diagram for an insulator is also shown, with the electron affinity χ and band gap E_g marked.

surface, which has been verified by experiment [Aumayr et al., 1993]. Note that even though Equation 5.12 has been obtained using the approximation $q \gg 1$, it can also be used for ion charge states as low as $q = 2$, with an error of less than a few percent compared with the exact solution.

When an ion beam is directed through a capillary parallel to its axis, it follows that only those ions which approach the inner walls to within a distance of R_c can capture electrons. In metallic capillaries ions are attracted to the walls by their image charge. Thus as shown in Figure 5.15, three types of trajectories result:

- 1) ions pass through without undergoing an interaction;
- 2) ions collide with the capillary walls and are lost;
- 3) ions reach the critical distance for electron capture at the exit.

In the last case ions which have undergone charge exchange emerge from the capillary and can be detected.

Based on these prepositions a theoretical description of charge exchange on transport of HCIs through metallic capillaries has been developed [Tórkési et al., 2001]. Good agreement between the modeled charge state distributions and the experimental results was found. The total amount of electron capture

for a given ion can be estimated geometrically from the ratio of the area available for charge exchange at the capillary exit, $2\pi R_{cap}R_c$ (using $R_c \ll R_{cap}$ where R_{cap} is the radius of the capillary), to the total cross sectional area, πR_{cap}^2 . Thus the fraction of charge exchange is given by:

$$f_{CX} \approx \frac{2R_c}{R_{cap}}. \quad (5.13)$$

This relation is used in the following analysis to compare the experimentally determined charge exchange fractions with theoretical predictions.

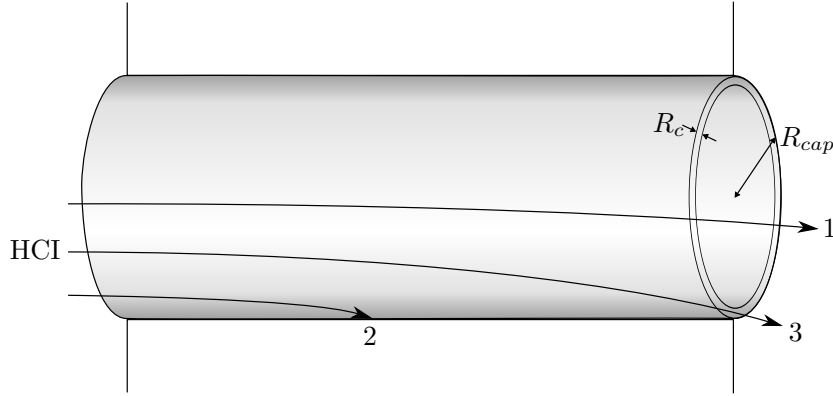


Figure 5.15: Schematic of the transport of HCl through an aperture in a metal foil showing the three trajectory scenarios. The critical capture distance, R_c , and capillary radius, R_{cap} , are marked.

The COB model for electron capture from metal surfaces has also been modified to describe electron capture from insulating surfaces [Hägg et al., 1997; Ducrée et al., 1998]. Amendments include a consideration of the local charges which accumulate on the insulator surface as a result of the removal of electrons, local work function changes and the dielectric response of the target. Since the nanoscale apertures used in the HCl-surface studies of this thesis were formed in an insulator, it is important to consider the effect the insulator is likely to have on the critical capture distance R_c . As shown in Figure 5.14, the effective work function, W_{Φ}^* , of an insulator can be approximated as the sum of its electron affinity, χ , and band gap, E_g . For silicon nitride, which is the insulator of interest here, $\chi \simeq 2 \text{ eV}$ and $E_g \simeq 5 \text{ eV}$ [Goodman, 1968]. This gives $W_{\Phi}^* \simeq 7 \text{ eV}$. Using the generalized relation for R_c given in [Hägg et al., 1997] it can be calculated that for a silicon nitride

target Equation 5.12 only underestimates R_c by $\sim 20\%$. Consequently, in the following discussion Equation 5.12 will continue to be used to estimate R_c and any resulting underestimation in the values of f_{CX} is borne in mind.

5.2.1 Transport of HCIs through nanoscale apertures

To begin with the result of an experiment using a beam of low charge state ions directed onto a target of nanoscale apertures is presented. The data are plotted in Figure 5.16 and correspond to the case of $0.3 \text{ keV u}^{-1} \text{ Ar}^{3+}$ ions transmitted through 100 nm diameter holes in a 500 nm thick silicon nitride membrane. The 2D scatter plots of particle events, recorded using the position sensitive MCP detector, were analyzed by binning the data along the plane of ion deflection, determined by the electrostatic analyzer, to give plots of ion intensity versus position.

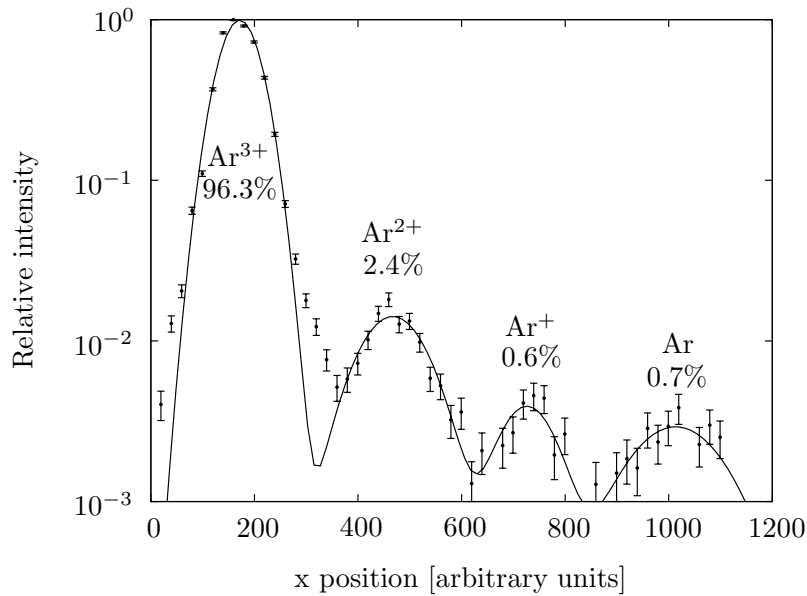


Figure 5.16: Charge state fractions of argon ions following transport of $0.3 \text{ keV u}^{-1} \text{ Ar}^{3+}$ through an array of 100 nm diameter holes in a 500 nm thick silicon nitride membrane.

The charge state fractions in the transmitted beam are calculated from the areas of Gaussian distributions fitted to the peaks in the lineout. In the example shown, approximately $(96.3 \pm 0.2)\%$ of the incident Ar^{3+} ions arrived at the detector in their original charge state, $(2.4 \pm 0.2)\%$ as Ar^{2+} ,

(0.6 ± 0.1) % as Ar^+ and (0.7 ± 0.1) % as neutrals. These fractions correspond to no charge exchange and to single, double and triple electron capture, respectively, from the aperture walls. The total percentage charge exchange inferred from these values is (3.7 ± 0.2) %. The errors are Gaussian errors determined from the accuracy of the fitted peak areas.

Similarly to Section 5.1.2, the amount of charge exchange occurring before the target, as a result of electron capture from residual gas in the beamline, is estimated using Equation 5.4. Calculating for the Ar^{3+} experiment, assuming a cross section for single electron capture from nitrogen of $\sigma_{CX} = 6.0 \cdot 10^{-16} \text{ cm}^2$ [Müller and Salzborn, 1977], and using an ion velocity of $v_{ion} = 2.4 \cdot 10^7 \text{ cm s}^{-1}$, density of neutrals $n_{neutral} = 3.2 \cdot 10^8 \text{ cm}^{-3}$ (calculated from 10^{-6} Pa) and the number of ions $N_{ion} = 2.1 \cdot 10^9 \text{ s}^{-1}$ (calculated from 1 nA), a rate of beamline charge exchange of $9.7 \cdot 10^9 \text{ s}^{-1}$ is obtained. After charge state selection by the bender magnet the ions travel 1 m to the target, which takes $4.2 \mu\text{s}$. This means that only ~ 0.002 % of the incident ions capture electrons prior to the target. Therefore the various charge state fractions measured on the MCP detector can be attributed solely to charge exchange with the nanoscale apertures.

A point to note is that the final charge state distribution recorded by the MCP detector is the result of a multitude of relaxation processes which succeed the actual charge exchange interaction [Tórkési et al., 2001]. The flight time for 0.3 keV u^{-1} argon ions from the aperture target to the electrostatic analyzer is about a microsecond. Thus by the time the ions arrive at the analyzer they are expected to have reached their ground states by Auger and/or photon emission. As a result, the final charge states detected, q_f , reflect the number of electrons retained by each ion after relaxation, which may be equal to or lower than the number of electrons initially transferred.

The charge state distribution presented in Figure 5.16 is in agreement with the measurements made elsewhere for Ne^{7+} ions transported through metallic nanoscale capillaries [Ninomiya et al., 1997]. Most of the ions emerge in their incident charge state and the charge exchange fractions generally decrease monotonically with q_f . In scattering experiments of HCIs from flat surfaces a very different distribution is measured. There the majority of ions become neutralized and the remaining charge fractions decrease dramatically with increasing q_f [Meyer et al., 1995; Folkerts et al., 1995]. In order to understand the difference, it is instructive to consider a particular result in the scattering investigations cited above, namely that for grazing collisions of HCIs on a silver surface, neutralization takes of the order of femtoseconds

and dominantly occurs at a distance of less than 2 \AA from the target surface. In contrast, the interaction time for a 0.3 keV u^{-1} argon ion traveling through a 500 nm length aperture could be up to a picosecond. Thus it can be concluded that for capillary targets charge exchange interactions with the inner walls are dominated by distant collisions which overall limit the number of electrons that can be transferred. This is a unique feature of capillary charge exchange and explains the further decrease in charge state fractions for multiple capture. The fraction of neutrals in Figure 5.16 is, however, slightly larger than the Ar^+ fraction. A similar enhancement of the neutral fraction was measured in [Ninomiya et al., 1997] and is thought to be due to the additional contribution of neutralizing hard collisions at the aperture exit.

A survey of the amount of charge exchange measured in the experiments using low charge state ions transported through apertures of different diameters is presented in Figure 5.17. Solid circles represent the total charge exchange fractions for 0.2 keV u^{-1} Ar^{2+} ions transported through 50, 100, 250 and 300 nm diameter holes in 200 nm thick silicon nitride. (The 50 nm hole size was achieved by platinum deposition on 100 nm holes.) Open circles mark data points for 0.3 keV u^{-1} Ar^{3+} ions transported through 100 nm diameter holes in 500 nm silicon nitride (from Figure 5.16) and 0.2 keV u^{-1} Ar^{2+} ions transported through a single $1.5\text{ }\mu\text{m}$ diameter hole in a chromium AFM tip.

In accordance with geometrical considerations, the fraction of ions undergoing charge exchange increases with decreasing aperture size. Since the membranes were coated on both sides with a thin film of gold-palladium alloy, it is conceivable that electron capture from both the silicon nitride and the metallic layer at the aperture exits occurred. Furthermore, in the case of the 50 nm holes, electron capture could have also proceeded from the platinum film on that sample. To investigate this, the work functions of the various materials are considered. The gold-palladium alloy has the lowest work function, estimated at $W_{\Phi} \simeq 5\text{ eV}$ [Michaelson, 1977] and silicon nitride has the highest, estimated at $W_{\Phi}^* \simeq 7\text{ eV}$, as shown earlier. For platinum $W_{\Phi} = 6.4\text{ eV}$ [Michaelson, 1977]. Thus the alloy is expected to give rise to the largest critical capture distance and the membrane is expected to give the smallest. Using Equations 5.12 and 5.13, the resulting maximum and minimum total percentages of electron capture predicted for Ar^{2+} ions from the alloy and the insulator, respectively, are calculated and plotted in Figure 5.17 as curves.

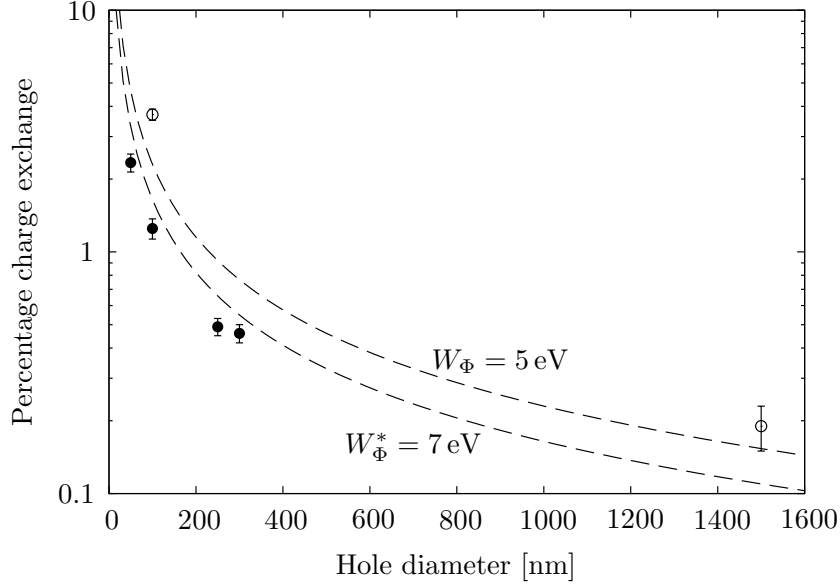


Figure 5.17: Survey of the effect of aperture diameter on the total amount of charge exchange. Solid circles represent the data obtained for $0.2 \text{ keV u}^{-1} \text{ Ar}^{2+}$ passing through holes of various sizes in 200 nm thick silicon nitride membranes. Open circles correspond to the transport of $0.3 \text{ keV u}^{-1} \text{ Ar}^{3+}$ through 100 nm diameter holes in 500 nm silicon nitride from Figure 5.16, and $0.2 \text{ keV u}^{-1} \text{ Ar}^{2+}$ through a single $1.5 \mu\text{m}$ diameter hole in a chromium AFM tip. Curves mark the predictions for the total amount of electron capture calculated using the COB model for two work functions.

It can be seen that the Ar^{2+} data points for the membrane targets follow most closely the model predictions using the effective work function for silicon nitride. This suggests that electron capture mainly proceeded from the membrane. Yet the data points do all lie below the theoretical curve for the insulator, on average by about one-quarter of the respective COB values. Hence the indication is that a certain degree of charge exchange suppression occurred. If the aforementioned underestimation of R_c for silicon nitride is considered, then the corresponding theoretical curve in the figure must also be underestimated. As a result the disparity between the experimental data and COB predictions becomes larger still. The suppression of charge exchange is discussed in more detail in connection with the results of the experiments with HClIs.

Calculating for Ar^{2+} ions transmitted through the $1.5 \mu\text{m}$ hole in the

chromium AFM tip, using $W_{\Phi} = 4.5 \text{ eV}$ [Michaelson, 1977], a total amount of electron capture of 0.2 % is predicted. This agrees with the experimental value rather well. In contrast, the data point from the Ar^{3+} experiment for 100 nm diameter holes in silicon nitride is higher than model predictions. Calculating for silicon nitride and the gold-palladium alloy, total percentages of charge exchange of 2 % and 2.8 %, respectively, are obtained (the experimentally determined value is 3.7 %). The reason for the discrepancy is not clear. An important point to note, however, is that the work functions of the surfaces used in the investigations were not well defined. This is because the exact composition and structure of the materials was unknown and the experiments were not performed in ultra high vacuum. As a result the work functions may have also varied slightly from one sample to the next.

Figure 5.18 presents the lineouts obtained from the experiments with HCIs. The silicon nitride membrane was 500 nm thick with an array of 200 nm diameter holes. Beams of 2 keV u^{-1} argon ions and 3 keV u^{-1} xenon ions were extracted from the EBIT and specific charge states selected. Figures 5.18(a) and 5.18(b) display the results for Ar^{16+} and Xe^{44+} ions, respectively. The scale bar in each figure shows the positions expected for the various charge states of each ion species. These are calculated from the distance of a non-deflected reference peak to the peak at full deflection. The COB model predictions of the critical capture radii for Ar^{16+} and Xe^{44+} from silicon nitride, using $q = 16, 44$ and $W_{\Phi}^* \simeq 7 \text{ eV}$ in Equation 5.12, are 1.2 and 1.9 nm, respectively. Accordingly, the percentages of electron capture predicted using Equation 5.13 are 2.3 and 3.8 %. These levels are marked in the figures as dashed lines.

In both lineouts, however, only one peak is observed. By comparing the width of the Ar^{16+} peak in Figure 5.18(a) with the spacings between the expected positions of the various charge states shown on the scale bar, it can be seen that the deflection voltage implemented should have been sufficient to resolve individual charge states. Consequently it is concluded that in the argon experiment the main peak corresponds solely to the incident Ar^{16+} ions. Due to the larger number of charge states to be accommodated in the Xe^{44+} case, the peaks corresponding to individual charge states would be much closer, as the scale bar in Figure 5.18(b) shows. However, the xenon peak does appear to be symmetrical, thus it too is assumed to correspond to the incident ion charge state only. Therefore, to within the sensitivity of the experiments, no charge exchange was detected. Due to the non-zero baselines it cannot be stated that no electron capture took place at all, but

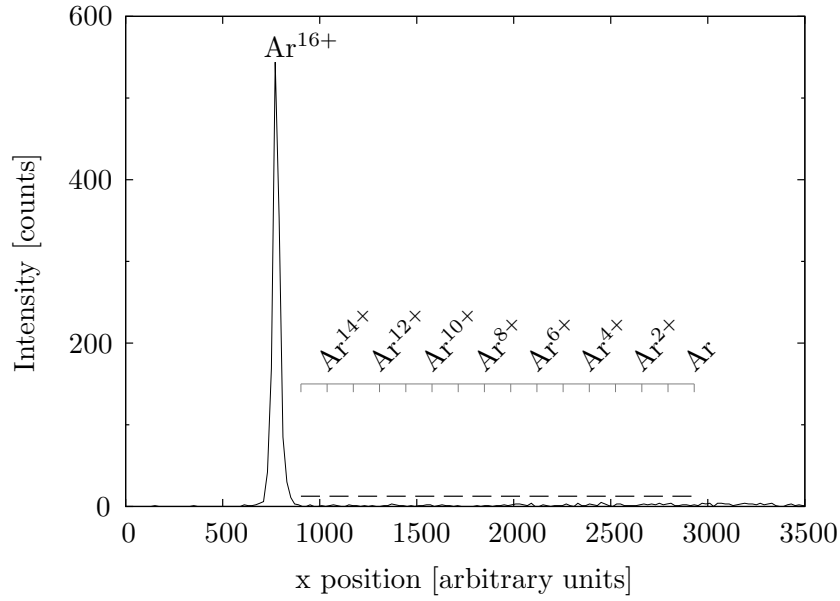
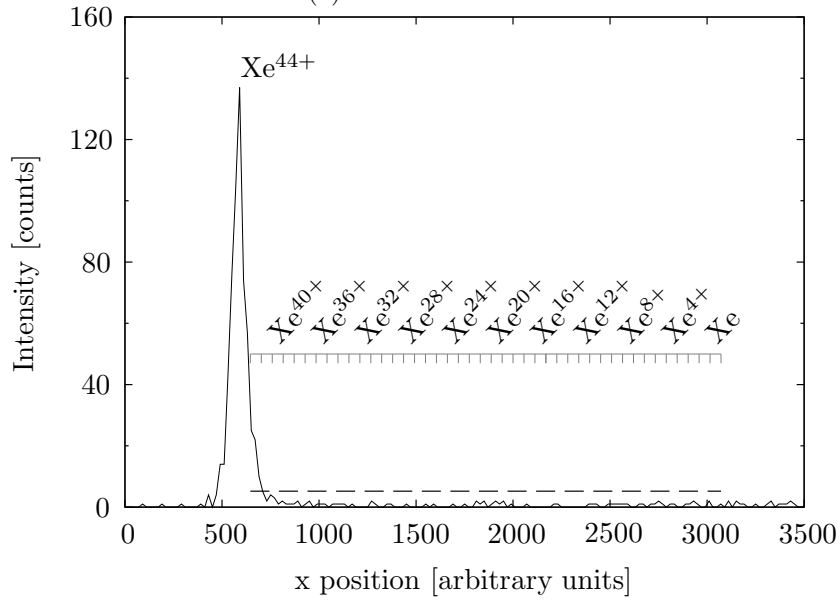

 (a) $2 \text{ keV u}^{-1} \text{ Ar}^{16+}$

 (b) $3 \text{ keV u}^{-1} \text{ Xe}^{44+}$

Figure 5.18: Transport of HCIs through an array of 200 nm diameter holes in a 500 nm thick silicon nitride membrane. The scale bar in each figure shows the expected positions of the various charge state fractions. Dashed lines represent the COB model predictions for the total amount of electron capture into Ar^{16+} and Xe^{44+} , at 2.3 and 3.8 %, respectively.

by calculating the ratio of background counts to the intensity of the main peak in each plot, upper limits for charge exchange can be inferred. Applying this method to the Ar^{16+} results, an upper limit of 1 % is obtained, which is about two-fifths of the COB model prediction for the total amount of electron capture. In the Xe^{44+} experiment an upper limit for charge exchange of 1.4 % is obtained, which is also approximately two-fifths of the COB value.

Taking into consideration the aforementioned underestimation of R_c for silicon nitride targets, it follows that the COB values calculated for the insulator in Figure 5.18 will also be underestimated. Furthermore, even if electron capture proceeded from the metal coating, which has a lower work function than the insulator, then the COB predictions plotted would underestimate that too. Thus in any event it is found that on transport of HCIs through nanoscale apertures in the silicon nitride membrane, charge exchange is suppressed. Moreover, the Ar^{16+} results allow a very marked suppression to be inferred. In an investigation using dielectric capillary targets conducted elsewhere, albeit for HCIs of lower Z than those investigated here, charge state fractions lower than the COB model predictions have indeed been resolved [Stolterfoht et al., 2002]. The experiment used $0.1 \text{ keV u}^{-1} \text{ Ne}^{7+}$ ions transported through 100 nm diameter capillaries in $10 \mu\text{m}$ polyethylene terephthalate foil. A total of $\sim 2.5 \%$ electron capture was measured. The COB model prediction for these parameters is $\sim 4 \%$. Charge state fractions corresponding to multiple capture were detected and fall off in much the same way as those recorded for metallic capillaries in [Ninomiya et al., 1997]. The superior statistics of the Stolterfoht experiments are due to the fact that the ions were extracted from an Electron Cyclotron Resonance source at higher currents than are possible using an EBIT.

The cause of the reduced charge exchange on transmission through dielectric capillaries is likely to be a capillary guiding phenomenon, proposed by Stolterfoht *et al.* to explain the observed angular distributions of HCIs transmitted through the polymer foils in the aforementioned experiment [Stolterfoht et al., 2002]. It was found that when the foils were tilted the direction of the emergent beam changed, which indicates that the ions still propagated through the capillaries parallel to their axes. Significant intensities of the incident charge state were even measured when tilt angles of $\pm 20^\circ$ were implemented. This was very unexpected, since it means that even after the presumed multiple scattering events of HCIs from the capillary walls (aspect ratio 1:100), the initial charge state is predominantly preserved rather than becoming depleted as a result of the commonly accepted neutralization ob-

served for scattering from flat surfaces [Meyer et al., 1995; Folkerts et al., 1995].

In the capillary guiding mechanism put forward, Stolterfoht *et al.* suggested that the HCIs pass through two distinct regions, a scattering region and a guiding region. In the scattering region ions incident on the inner walls deposit charge in a self-organizing manner. Charge accumulates until ions are repelled by the electrostatic field established, which in turn limits further charge collection. Subsequent ions are then deflected from one charge patch to another until they reach the so-called guiding region. This was introduced to explain the symmetrical angular distributions of the transmitted beams. The depth of the guiding potential governs the divergence of the emerging ions. Time studies confirm that guiding through the dielectric capillaries can only commence after a certain amount of charge has been deposited [Stolterfoht et al., 2002, 2004a,b] and in very recent experiments the reduction in charge exchange as a result of the increasing repulsive field has been measured [Kanai et al., 2007]. Even so it is still not fully understood how the potential in the guiding region is produced. The charge distribution on the inner walls certainly cannot be uniform, because the electrostatic field in the capillary would then be very weak, due to the fact that a continuously charged infinite tube is field free. In any case, in the model proposed most of the charge exchange occurs near the capillary entrance, as a result of the dynamic interplay between charge deposition and reflection. This differs from the situation for metallic capillaries, where charge exchange is thought to occur at the exit, as previously discussed, and guiding does not arise [Stolterfoht et al., 2002, 2005].

In order to account for the observed decrease in transmitted ion intensity on increasing the tilt angle of the target, the initial capillary guiding model has been extended to include non-linear charge dependencies [Stolterfoht et al., 2003, 2004a]. Recently the first theoretical treatment of the problem was reported [Schiessl et al., 2005a,b]. Using a CTMC technique the trajectories of ions passing through the capillaries were simulated and it is shown that arrays of multiple charge patches, such as those proposed for the scattering region of the model discussed above, are in fact unstable. Instead, guiding can result from a single charge patch formed at the capillary entrance, which reflects subsequent ions towards the end without additional deflections. The charge deposited migrates along the capillary walls according to the electrical properties of the dielectric, and the electrostatic field developed then causes a certain defocusing of the ion beam at the exit. Thus in addition

to charge exchange occurring at the entrance of the dielectric capillary, it is also suggested to take place at the exit [Sahana et al., 2006]. This theory is partially borne out by the experimental results, but the interpretation of capillary guiding still remains an ongoing and challenging task.

The guiding potential U_g required to reflect an ion of charge state q from the capillary wall can be estimated using the relation:

$$U_g \geq \frac{E \sin^2 \theta}{eq}, \quad (5.14)$$

i.e. U_g must be greater than or equal to the component of the ion's total kinetic energy, E , perpendicular to the wall. In the experiments presented here ion beams were directed onto apertures approximately parallel to their axes, therefore θ is the beam divergence. Figure 5.19 presents a schematic of the scenario, showing how an ion is reflected from the sidewall of one of the silicon nitride apertures at a distance greater than R_c , thus emerging without having undergone charge exchange. With $\theta \approx 0.8^\circ$, estimated from the experimental setup, the minimum values of U_g calculated for the $2 \text{ keV u}^{-1} \text{ Ar}^{16+}$ and $3 \text{ keV u}^{-1} \text{ Xe}^{44+}$ ions investigated are 1 V and 1.8 V, respectively. For the $0.2 \text{ keV u}^{-1} \text{ Ar}^{2+}$ and $0.3 \text{ keV u}^{-1} \text{ Ar}^{3+}$ ions used in the preliminary experiments, a minimum value of 0.8 V is calculated. These values are in agreement with the guiding potentials of $U_g \approx 1 \text{ V}$ inferred from experiments conducted elsewhere [Stolterfoht et al., 2002, 2004a; Víkor et al., 2005].

The amount of charge which can accumulate on the capillary walls can be calculated from the rate at which elementary charges, e , enter a single capillary in a given experiment. For the guiding studies using nanoampere Ne^{7+} beams transmitted through the 100 nm diameter capillaries in polyethylene terephthalate in [Stolterfoht et al., 2002], it was estimated that $2200 e$ entered each capillary per minute. Furthermore, the time dependence of the transmitted beam intensity for a tilted sample was investigated and it was found that the intensity rose from a very small value (onset of charging) to a maximum (dynamic equilibrium) with an exponential time constant of 2.5 minutes. The final amount of charge deposited on the capillary walls was thus evaluated at $5500 e$.

In contrast, in this work the picoampere beams of HClIs collimated onto a 3 mm wide beam spot, assuming homogenous exposure, resulted in $\sim 2 e$ entering each 200 nm diameter aperture per minute. The relatively low ion dose rates precluded a time study of the charge up of the aperture walls, e.g. by monitoring the charge exchange fractions over time. However, it

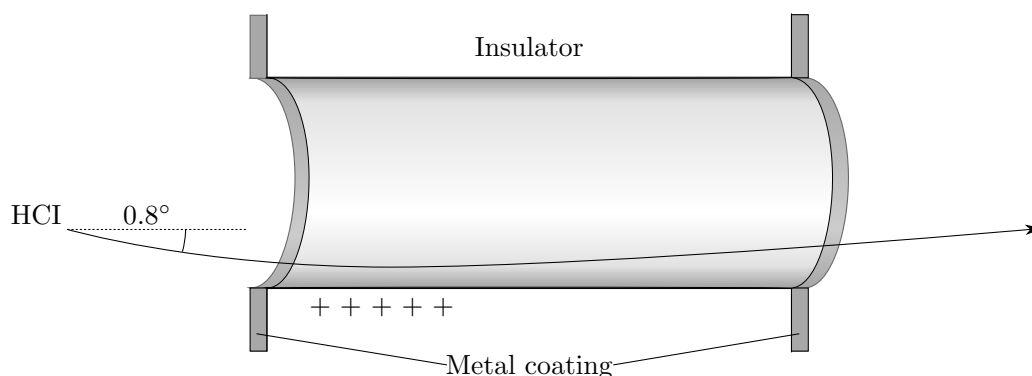


Figure 5.19: Schematic of the transport of HCl⁺ through one of the apertures in the metal-coated silicon nitride membranes used in this study. A trajectory for ions deflected by an accumulation of positive charge on the aperture wall is marked.

is clear that there is a significant difference between the currents entering single capillaries/apertures in each investigation. Moreover, even though the experiments here were conducted continuously for many hours, the disparity between the degrees of charging is larger still. This is because of the small aspect ratios and non-tilted setup implemented in this work, meaning that the majority of incident ions could pass through the apertures without interacting at all. It thus seems very likely that the capillary walls in [Stolterfoht et al., 2002] charged up to a greater extent than the aperture walls in the HCl⁺ experiments carried out here, yet suppression of charge exchange in the experiments of this thesis still occurred.

Calculating for the experiments using nanoampere beams of low charge state ions from the ion gun, $\sim 1700 e$ entered a 200 nm aperture per minute, which is nearly three orders of magnitude higher than the amount calculated for the HCl⁺ experiments and in line with the values quoted for the guiding experiments in [Stolterfoht et al., 2002]. This supports the supposition based on the Ar²⁺ results presented in Figure 5.17, that there too charge exchange was suppressed. In fact, in experiments conducted elsewhere the guiding of protons and molecular hydrogen ions (with negligible fragmentation) through insulating capillaries is also reported [Stolterfoht et al., 2004b, 2005].

In summary, the experimental results have shown a suppression of charge exchange for the transport of HCIs and low charge state ions through nanoscale apertures in insulating membranes. Of course the apertures used in these studies did not have the large aspect ratios of the nanoscale capillaries used in the guiding studies conducted elsewhere. Neither were such large aspect ratios desired, since the focus of this work was on the specific setup for ion implantation described in Chapter 1. The implication of the results on the implantation scheme are discussed in the following, final chapter of this thesis.

Chapter 6

Conclusions and Outlook

The studies of charge exchange between HCIs and gases focused on the K -shell x-ray emission following electron capture by slow $\text{Ar}^{17+}, 18+$ ions from argon neutrals. This was aimed towards shedding light on the dependence of the angular momentum capture state on collision energy. Beams of HCIs were extracted from an EBIT and directed onto an external gas target via a retardation assembly. This enabled a controlled investigation over a range of collision energies to be carried out. Magnetic trapping experiments using the HCIs in the EBIT itself allowed comparative measurements for HCIs at the lower end of this energy range to be made. Similar work in this field is carried out by the EBIT groups at NIST and LLNL, in the first case using extracted HCIs and in the second, by implementing magnetic trapping. However, the extraction beamline at NIST is not equipped with a device for ion deceleration. Hence prior to the results presented here there was a gap in experimental data for energies between those of non-decelerated extracted HCIs ($\sim 1000 \text{ eV u}^{-1}$) and the HCIs in the trap ($\sim 10 \text{ eV u}^{-1}$).

Comparison of the experimental x-ray emission spectra proceeded on the basis of the intensity ratio of the sum of $n \geq 3 \rightarrow 1$ to $n = 2 \rightarrow 1$ transitions (the hardness ratio), the value of which increases with an increasing fraction of electron capture into np -states. The calculation of hardness ratios is a common analytical method, which is of particular use in the interpretation of spectra recorded using low resolution detectors. The results of the experiments with extracted HCIs show an increase in hardness ratio with decreasing collision energy. This is most marked for capture into Ar^{18+} , increasing from a value of ~ 0.3 at 1000 eV u^{-1} , to ~ 0.6 at 2 eV u^{-1} . A deviation from the statistical population of angular momentum states is thus confirmed and instead, a rising tendency for capture into np -states with de-

creasing collision energy is measured. This is in line with, and forms the first thorough experimental test of, a set of CTMC calculations implemented elsewhere [Beiersdorfer et al., 2000; Otranto, 2006]. The lower sensitivity of the Ar^{17+} spectra to capture state is explained in terms of a de-emphasizing of the Lyman transitions, due to the unpaired electron in the K -shell of the hydrogenic ion.

Interestingly, the hardness ratios from the Ar^{18+} magnetic trapping measurements do not conform with the extraction results. For example, at a collision energy of 4.5 eV u^{-1} , inferred from the axial trap depth, a hardness ratio of ~ 1.1 is measured. This is about twice the value of the hardness ratio obtained using a similar energy in the extraction experiments. The discrepancy is attributed to a difference in the population mechanism and/or stabilization process of the Rydberg states of the HCIs in the EBIT environment when compared to the conditions of an external gas target. The exact cause and nature of this difference is not yet known. Various scenarios have been discussed and concluded to be unlikely. These included an overestimation of the collision energy of the trapped ions and the influence of the magnetic field in the trap on the momentum of an electron just prior to capture. Large hardness ratios for Ar^{18+} charge exchange have also been measured in magnetic trapping experiments conducted at LLNL [Beiersdorfer et al., 2000]. However, in the absence of comparative data it had been stated that for decreasing collision energies the hardness ratio increases much more steeply than the extraction results of this thesis have now revealed.

As discussed in Chapter 1, investigations of HCI-gas charge exchange recently gained impetus due to the discovery of x-ray emission from comets, the main cause of which is established as electron capture by HCIs in the solar wind from gas neutrals in the cometary coma. To aid the interpretation of such spectra, the EBIT projects at NIST and LLNL have therefore also focused on measuring charge exchange spectra using astrophysically relevant collision partners. As a result of this thesis, it can now be said that, because charge exchange is affected by the conditions in the trap, data acquired in the magnetic trapping experiments such as those of LLNL should be applied to the astrophysical case with caution. In addition, a time study undertaken in this work detected a sharp increase in hardness ratio in the first half a second of magnetic trapping. Hence it is also crucial to compare data collected within the same time frame. In contrast, experiments using extracted beams of HCIs allow a much more controlled investigation of charge exchange. Furthermore, by incorporating a retardation assembly into the extraction beam-

line, as in the Berlin setup, charge exchange spectra for a range of collision energies can be obtained. A point to note, however, is that theoretical work has shown that electric dipole-forbidden transitions from metastable states in the HCIs can give rise to intense emissions [Kharchenko and Dalgarno, 2001]. These will be absent from the spectra obtained in beamline experiments. However, depending on the density of gas in the coma of the comet, such states may be collisionally quenched.

For future experiments of this type it would be of great benefit to use high resolution x-ray detectors, such as the microcalorimeter at NIST. This would allow the individual K_α peaks in mixed spectra to be resolved more clearly. Narrower peaks would also enable a more accurate determination of the contribution of double electron capture to the spectra which, as discussed, can have relatively large cross sections and should therefore not be neglected. In the extraction experiments improved isolation of the gas jet from the rest of the beamline would considerably reduce charge exchange events of the HCIs prior to impact on the target, which were detrimental to the interpretation of the Ar^{18+} data. Improvements in the transport efficiency of HCIs through the beamline, in particular through the deceleration assembly where many ions were lost, would also significantly improve count rates. Building on the success of this first experimental program of charge exchange spectral measurements at the Berlin EBIT, an extension to other collision partners and the measurement of, for example, L -shell spectra would also yield highly sought-after data.

In the studies of charge exchange between HCIs and surfaces, the technique of ion transport through small apertures was implemented. This allowed the detection of ions which emerge from the apertures having captured electrons from the side walls, to be contrasted with experiments using flat surfaces (except grazing incidence studies) where ions are destined to collide with the solid and therefore escape direct detection. The goal of the experiments was to obtain benchmark data for an aligned single ion implantation setup, in which HCIs are transported through a small hole in the cantilever of an AFM tip. Silicon nitride membranes fashioned with apertures formed via FIB-drilling are used as beam collimators and these were used as the targets in the transport studies.

The experimental results reveal a suppression of charge exchange for HCIs, as well as for low charge state ions, transported through the nanoscale apertures. For example, for 2 keV u^{-1} Ar^{16+} ions transported through an array of 100 nm holes, an upper limit to charge exchange of 1 % is inferred.

The COB model predicts 2.3 %. The observed suppression is attributed to an accumulation of charge on the inner surfaces of the insulating aperture, preventing the critical distance for electron capture from being reached. These findings support a capillary guiding phenomenon reported in experiments using high aspect ratio capillaries in polymer foils. A complete theoretical description of the guiding mechanism has yet to be finalized. For the application of such apertures as collimators in the single ion implantation setup with an ion detection scheme based on the production of secondary electrons, the preservation of transmitted HCIs in their high charge states is advantageous. This is because the yield of secondary electrons generated on ion impact scales with ion charge.

In the field of nanotechnology tiny pores and capillaries are widely used and it is proposed that the chemical and physical properties of their inner surfaces, which are essentially unknown as they are difficult to explore, could be probed by slow ions. In addition, channeling by nanocapillaries, for example carbon nanotubes, as a means to transport ions in their original charge state efficiently from one place to another is an exciting and emerging field. Consequently, further investigations of ion transport through nanocapillaries are required. If the targets comprise capillary arrays, it is important to ensure uniformity and parallelism in order to avoid geometrical effects. This can be achieved by using optical lithography in combination with photo-assisted electrochemical etching, as in [Kumar et al., 2005].

Possible improvements to the experimental arrangement used for the studies of charge exchange presented in this work include an optimization of the ion transport efficiency of the Berkeley EBIT and REBIT beamlines and an increased separation of charge states in the electrostatic analysis of the ions emerging from the targets. The latter would be of particular use for experiments with the highest ion charge states, for example the Xe^{44+} ions investigated here, and would best be achieved by implementing an ion spectrometer.

To summarize, as a result of this research, key missing experimental data for the energy dependence of hardness ratio in slow charge exchange collisions between HCIs and gases have been obtained. In addition, a suppression of charge exchange for insulating apertures, previously only measured for moderately charged ions, has now also been observed for HCIs. The effects have been analyzed and discussed, suggestions for experimental improvements have been made and ideas for new experiments to answer open questions have been given.

Bibliography

- R. Ali, C.L. Cocke, M.L.A. Raphaelian, and M. Stockli. . *Phys. Rev. A*, 49: 3586, 1994.
- F. Aumayr, H. Kurz, D. Schneider, M.A. Briere, J.W. McDonald, C.E. Cunningham, and HP. Winter. . *Phys. Rev. Lett.*, 71:1943, 1993.
- P. Beiersdorfer. . *Annu. Rev. Astron. Astrophys.*, 41:343, 2003.
- P. Beiersdorfer. . *AIP Conf. Proc.*, 389:121, 1997.
- P. Beiersdorfer, B. Beck, St. Becker, and L. Schweikhard. . *Int. J. Mass Spectrom. Ion Proc.*, 157/158:149, 1996a.
- P. Beiersdorfer, G.V. Brown, J. Crespo López-Urrutia, V. Decaux, S.R. Elliott, D.W. Savin, A.J. Smith, G.S. Stefanelli, K. Widmann, and K.L. Wong. . *Hyperfine Int.*, 99:203, 1996b.
- P. Beiersdorfer, A.L. Osterheld, V. Decaux, and K. Widmann. . *Phys. Rev. Lett.*, 77:5353, 1996c.
- P. Beiersdorfer, L. Schweikhard, J. Crespo López-Urrutia, and K. Widmann. . *Rev. Sci. Instrum.*, 67:3818, 1996d.
- P. Beiersdorfer, R.E. Olson, G.V. Brown, H. Chen, C.L. Harris, P.A. Neill, L. Schweikhard, S.B. Utter, and K. Widmann. . *Phys. Rev. Lett.*, 85:5090, 2000.
- P. Beiersdorfer, J.A. Britten, G.V. Brown, H. Chen, E.J. Clothiaux, J. Cottam, E. Förster, M.-F. Gu, C.L. Harris, S.M. Kahn, J.K. Lepson, P.A. Neill, D.W. Savin, H. Schulte-Schrepping, L. Schweikhard, A.J. Smith, E. Träbert, J. Tschischgale, S.B. Utter, and K.L. Wong. . *Phys. Scr.*, T92:268, 2001a.

BIBLIOGRAPHY

- P. Beiersdorfer, C.M. Lisse, R.E. Olson, G.V. Brown, and H. Chen. . *Astrophys. J.*, 549:L147, 2001b.
- P. Beiersdorfer, K.R. Boyce, G.V. Brown, H. Chen, S.M. Kahn, R.L. Kelly, M. May, R.E. Olson, F.S. Porter, K. Stahle, and W.A. Tillotson. . *Science*, 300:1558, 2003.
- C. Biedermann, A. Förster, G. Fussmann, and R. Radtke. . *Phys. Scr.*, T73:360, 1997.
- F. Bosch. . *Phys. Scr.*, T80:28, 1999.
- I.G. Brown. . In I.G. Brown, editor, *The Physics and Technology of Ion Sources*, page 331. Wiley, New York, 1989.
- J. Burgdörfer, R. Morgenstern, and A. Niehaus. . *J. Phys. B*, 19:L507, 1986.
- J. Burgdörfer, P. Lerner, and F.W. Meyer. . *Phys. Rev. A*, 44:5674, 1991.
- A. Bárány, G. Astner, H. Cederquist, H. Danared, S. Huldt, P. Hvelplund, A. Johnson, H. Knudsen, L. Liljeby, and K.-G. Rensfelt. . *Nucl. Instr. and Meth. B*, 9:397, 1985.
- A. Cassimi, S. Duponchel, X. Flechard, P. Jardin, P. Sortais, D. Hennecart, and R.E. Olson. . *Phys. Rev. Lett.*, 76:3679, 1996.
- J.-Y. Chesnel, B. Sulik, H. Merabet, C. Bedouet, F. Frémont, X. Husson, M. Grether, A. Spieler, and N. Stolterfoht. . *Phys. Rev. A*, 57:3546, 1998.
- R.D. Cowan. *The Theory of Atomic Structure and Spectra*, page 570. University of California Press, Berkeley and Los Angeles, 1981.
- T.E. Cravens. . *Science*, 296:1042, 2002.
- T.E. Cravens. . *Geophys. Res. Lett.*, 24:105, 1997.
- J.R. Crespo López-Urrutia, P. Beiersdorfer, D.W. Savin, and K. Widmann. . *Phys. Rev. A*, 58:238, 1998.
- F. Currell and G. Fussmann. . *IEEE Transactions on Plasma Science*, 33:1763, 2005.

- F.J. Currell. . In F.J. Currell, editor, *The Physics of Multiply and Highly Charged Ions*, volume 1, page 39. Kluwer Academic, Dordrecht, 2003.
- F.J. Currell. . In J. Gillaspy, editor, *Trapping Highly Charged Ions: Fundamentals and Applications*, page 3. Nova Science Publishers, Inc., Huntington, New York, 1999.
- K. Dennerl, J. Englhauser, and J. Trümper. . *Science*, 277:1625, 1997.
- D. Dijkkamp, Yu.S. Gordeev, A. Brazuk, A.G. Drentje, and F.J. de Heer. . *J. Phys. B*, 18:737, 1985.
- E.D. Donets. . *IEEE Trans. Nucl. Sci.*, NS-23:897, 1976.
- E.D. Donets. . *Rev. Sci. Instrum.*, 69:614, 1998.
- E.D. Donets and V.P. Ovsyannikov. . *Sov. Phys. JETP*, 53:466, 1981.
- J.J. Ducrée, F. Casali, and U. Thumm. . *Phys. Rev. A*, 57:338, 1998.
- K.G. Dyall, I.P. Grant, C.T. Johnson, F.A. Parpia, and E.P. Plummer. . *Comput. Phys. Commun.*, 55:425, 1989.
- B. Edlén. . *Z. Astrophysik*, 22:30, 1942.
- U. Feldman, W. Curdt, E. Landi, and K. Wilhelm. . *Astrophys. J.*, 544:508, 2000.
- L. Folkerts, S. Schippers, D.M. Zehner, and F.W. Meyer. . *Phys. Rev. Lett.*, 74:2204, 1995.
- S. Fritzsche. . *J. Electr. Spec. Rel. Phenon.*, 114-116:1155, 2001.
- S. Fritzsche. . *Phys. Scr.*, T100:37, 2002.
- S. Fritzsche. . Private communications, 2003.
- T. Fuchs, C. Biedermann, R. Radtke, E. Behar, and R. Doron. . *Phys. Rev. A*, 58:4518, 1998.
- G. Fussmann, C. Biedermann, and R. Radtke. . In H. Schlüter and A. Shivarova, editors, *Advanced Technologies based on Wave and Beam Generated Plasmas*, page 429. Kluwer Academic, Amsterdam, 1999.

BIBLIOGRAPHY

- J.D. Gillaspy. . *J. Phys. B*, 34:R93, 2001.
- J.D. Gillaspy. . *Phys. Scr.*, T65:168, 1996.
- J.D. Gillaspy. . *Phys. Scr.*, T71:99, 1997.
- A.M. Goodman. . *Appl. Phys. Lett.*, 13:275, 1968.
- J.B. Greenwood, I.D. Williams, S.J. Smith, and A. Chutjian. . *Phys. Rev. A*, 63:062707, 2001.
- L. Hägg, C.O. Reinhold, and J. Burgdörfer. . *Phys. Rev. A*, 55:2097, 1997.
- A.A. Hasan, F. Eissa, R. Ali, D.R. Schultz, and P.C. Stancil. . *Astrophys. J.*, 560:L201, 2001.
- G. Hermann. . *J. Appl. Phys.*, 29:127, 1958.
- P. Hvelplund, L.H. Anderson, A. Bárány, H. Cederquist, J. Heinemeier, H. Knudsen, K.B. MacAdam, E.H. Nielsen, and J. Sørensen. . *Nucl. Instr. and Meth. B*, 9:421, 1985.
- R.K. Janev and H. Winter. . *Phys. Rep.*, 117:265, 1985.
- Y. Kanai, M. Hoshino, T. Kambara, T. Ikeda, R. Hellhammer, N. Stolterfoht, and Y. Yamazaki. . *Nucl. Instr. and Meth. B*, 258:155, 2007.
- V. Kharchenko and A. Dalgarno. . *Astrophys. J.*, 554:L99, 2001.
- Y.S. Kim and R.H. Pratt. . *Phys. Rev. A*, 27:2913, 1983.
- D.A. Knapp, R.E. Marrs, M.A. Levine, C.L. Bennett, M.H. Chen, J.R. Henderson, M.B. Schneider, and J.H. Scofield. . *Phys. Rev. Lett.*, 62:2104, 1989.
- D.A. Knapp, R.E. Marrs, S.R. Elliott, E.W. Magee, and R. Zasadzinski. . *Nucl. Instr. and Meth. A*, 334:305, 1993.
- G. Kraft. . In F.J. Currell, editor, *The Physics of Multiply and Highly Charged Ions*, volume 1, page 149. Kluwer Academic, Dordrecht, 2003.
- V. Krasnopolsky. . *Icarus*, 128:368, 1997.

- R.T. Rajendra Kumar, X. Badel, G. Vikor, J. Linnros, and R. Schuch. . *Nanotechnology*, 16:1697, 2005.
- D. Leitner and C. Lyneis. . In I.G. Brown, editor, *The Physics and Technology of Ion Sources*, page 203. Wiley-VCH Weinheim, second edition, 2004.
- M.A. Levine, R.E. Marrs, and R.W. Schmieder. . *Nucl. Instr. and Meth. A*, 237:429, 1985.
- M.A. Levine, R.E. Marrs, J.R. Henderson, D.A. Knapp, and M.B. Schneider. . *Phys. Scr.*, T22:157, 1988.
- M.A. Levine, R.E. Marrs, J.N. Bardsley, P. Beiersdorfer, C.L. Bennett, M.H. Chen, T. Cowan, D. Dietrich, J.R. Henderson, D.A. Knapp, A. Osterheld, B.M. Penetrante, M.B. Schneider, and J.H. Scofield. . *Nucl. Instr. and Meth. B*, 43:431, 1989.
- J. Li, D. Stein, C. McMullan, D. Branton, M.J. Aziz, and J.A. Golovchenko. . *Nature*, 412:166, 2001.
- C.M. Lisse, K. Dennerl, J. Englhauser, M. Harden, F.E. Marshall, M.J. Mumma, R. Petre, J.P. Pye, M.J. Ricketts, J. Schmitt, J. Trümper, and R.G. West. . *Science*, 274:205, 1996.
- C.M. Lisse, D. Christian, K. Dennerl, J. Englhauser, J. Trümper, M. Desch, F.E. Marshall, R. Petre, and S. Snowden. . *Icarus*, 141:316, 1999.
- W. Lotz. . *Z. Phys.*, 216:241, 1968.
- R. Mann, F. Folkmann, and H.F. Beyer. . *J. Phys. B*, 14:1161, 1981.
- R.E. Marrs, M.A. Levine, D.A. Knapp, and J.R. Henderson. . *Phys. Rev. Lett.*, 60:1715, 1988.
- R.E. Marrs, S.R. Elliott, and D.A. Knapp. . *Phys. Rev. Lett.*, 72:4082, 1994.
- R.E. Marrs, P. Beiersdorfer, S.R. Elliott, D.A. Knapp, and Th. Stoehlker. . *Phys. Scr.*, T59:183, 1995.
- S. Martin, J. Bernard, L. Chen, A. Denis, and J. Désesquelles. . *Phys. Scr.*, T73:149, 1997.

BIBLIOGRAPHY

- I. Martinson. . *Rep. Prog. Phys.*, 52:157, 1989.
- J.W. McDonald and D.H.G. Schneider. . *Nucl. Instr. and Meth. B*, 241:870, 2005.
- J.W. McDonald, R.W. Bauer, and D.H.G. Schneider. . *Rev. Sci. Instrum.*, 73:30, 2002.
- F.W. Meyer, L. Folkerts, and S. Schippers. . *Nucl. Instr. and Meth. B*, 100:366, 1995.
- H.B. Michaelson. . *J. Appl. Phys.*, 48:4729, 1977.
- A.M. Minor, F.I. Allen, V.R. Radmilovic, E.A. Stach, and T. Schenkel. . *Microscopy and Microanalysis*, 10:1118, 2004.
- A. Müller and E. Salzborn. . *Phys. Lett. A*, 62:391, 1977.
- A. Niehaus. . *J. Phys. B*, 19:2925, 1986.
- E.H. Nielsen, L.H. Andersen, A. Bárány, H. Cederquist, P. Hvelplund, H. Knudsen, K.B. MacAdam, and J. Sørensen. . *J. Phys. B*, 17:L139, 1984.
- S. Ninomiya, Y. Yamazaki, F. Koike, H. Masuda, T. Azuma, K. Komaki, K. Kuroki, and M. Sekiguchi. . *Phys. Rev. Lett.*, 88:4557, 1997.
- R.E. Olson. . *Phys. Rev. A*, 24:1276, 1981.
- S. Otranto. . Private communications, 2006.
- S. Otranto, R.E. Olson, and P. Beiersdorfer. . *Phys. Rev. A*, 73:022723, 2006.
- B.M. Penetrante, J.N. Bardsley, D. DeWitt, M. Clark, and D. Schneider. . *Phys. Rev. A*, 43:4861, 1991.
- A.I. Pikin, C.A. Morgan, E.W. Bell, L.P. Ratliff, D.A. Church, and J.D. Gillaspay. . *Rev. Sci. Instrum.*, 67:2528, 1996.
- M. Rigazio, V. Kharchenko, and A. Dalgarno. . *Phys. Rev. A*, 66:064701, 2002.

- H. Ryufuku, K. Sasaki, and T. Watanabe. . *Phys. Rev. A*, 21:745, 1980.
- M.B. Sahana, P. Skog, Gy. Viktor, R.T. Rajendra Kumar, and R. Schuch. . *Phys. Rev. A*, 73:040901, 2006.
- T. Schenkel, A.V. Barnes, M.A. Briere, A. Hamza, A. Schach von Wittenau, and D.H. Schneider. . *Nucl. Instr. and Meth. B*, 125:153, 1997.
- T. Schenkel, A.V. Hamza, A.V. Barnes, and D.H. Schneider. . *Prog. Surf. Sci.*, 61:23, 1999.
- T. Schenkel, A. Persaud, A. Kraemer, J.W. McDonald, J.P. Holder, A.V. Hamza, and D.H. Schneider. . *Rev. Sci. Instrum.*, 73:663, 2002.
- T. Schenkel, A. Persaud, S.J. Park, J. Nilsson, J. Bokor, J.A. Liddle, R. Keller, D.H. Schneider, D.W. Cheng, and D.E. Humphries. . *J. Appl. Phys.*, 94:7017, 2003a.
- T. Schenkel, V. Radmilovic, E.A. Stach, S.J. Park, and A. Persaud. . *J. Vac. Sci. Technol. B*, 21:2720, 2003b.
- K. Schiessl, W. Palfinger, C. Lemell, and J. Burgdörfer. . *Nucl. Instr. and Meth. B*, 232:228, 2005a.
- K. Schiessl, W. Palfinger, K. Tökési, H. Nowotny, C. Lemell, and J. Burgdörfer. . *Phys. Rev. A*, 72:062902, 2005b.
- D. Schneider, D. DeWitt, M.W. Clark, R. Schuch, C.L. Cocke, R. Schmieder, K.J. Reed, M. Chen, R.E. Marrs, M. Levine, and R. Fortner. . *Phys. Rev. A*, 42:3889, 1990.
- D. Schneider, M.W. Clark, B.M. Penetrante, J. McDonald, D. DeWitt, and J.N. Bardsley. . *Phys. Rev. A*, 44:3119, 1991.
- B. Sharkov. . In I.G. Brown, editor, *The Physics and Technology of Ion Sources*, page 233. Wiley-VCH Weinheim, second edition, 2004.
- J.D. Silver, A.J. Varney, H.S. Margolis, P.E.G. Baird, I.P. Grant, P.D. Groves, W.A. Hallet, A.T. Hanford, P.J. Hirst, A.R. Holmes, D.J.H. Howie, R.A. Hunt, K.A. Nobbs, M. Roberts, W. Studholme, J.S. Wark, M.T. Williams, M.A. Levine, D.A. Dietrich, W.G. Graham, I.D. Williams, R. O’Neil, and S.J. Rose. . *Rev. Sci. Instrum.*, 65:1072, 1994.

BIBLIOGRAPHY

- M.P. Stöckli. . *Z. Phys. D*, 21:S111, 1991.
- T. Stöhlker, T. Ludziejewski, and H. Reich. . *Phys. Rev. A*, 58:2043, 1998.
- N. Stolterfoht, K. Sommer, J.K. Swenson, C.C. Havener, and F.W. Meyer. . *Phys. Rev. A*, 42:5396, 1990.
- N. Stolterfoht, J.-H. Bremer, V. Hoffmann, R. Hellhammer, D. Fink, A. Petrov, and B. Sulik. . *Phys. Rev. Lett.*, 88:133201, 2002.
- N. Stolterfoht, V. Hoffmann, R. Hellhammer, Z.D. Pešić, D. Fink, A. Petrov, and B. Sulik. . *Nucl. Instr. and Meth. B*, 203:246, 2003.
- N. Stolterfoht, R. Hellhammer, Z.D. Pešić, V. Hoffmann, J. Bundesmann, A. Petrov, D. Fink, and B. Sulik. . *Vacuum*, 73:31, 2004a.
- N. Stolterfoht, R. Hellhammer, Z.D. Pešić, V. Hoffmann, J. Bundesmann, A. Petrov, D. Fink, B. Sulik, M. Shah, K. Dunn, J. Pedregosa, and R.W. McCullough. . *Nucl. Instr. and Meth. B*, 225:169, 2004b.
- N. Stolterfoht, R. Hellhammer, P. Sobocinski, Z.D. Pešić, J. Bundesmann, B. Sulik, M.B. Shah, K. Dunn, J. Pedregosa, and R.W. McCullough. . *Nucl. Instr. and Meth. B*, 235:460, 2005.
- E. Takács, K. Tőkési, H. Tawara, C.J. Verzani, T. Hohl, J.D. Gillaspay, and J. Pálinkás. . *Rad. Phys. Chem.*, 76:617, 2007.
- H. Tawara. . In F.J. Currell, editor, *The Physics of Multiply and Highly Charged Ions*, volume 1, page 103. Kluwer Academic, Dordrecht, 2003.
- H. Tawara, P. Richard, U.I. Safronova, and P.C. Stancil. . *Phys. Rev. A*, 64:042712, 2001.
- H. Tawara, E. Takács, L.P. Ratliff, J.D. Gillaspay, and K. Tőkési. . *Nucl. Instr. and Meth. B*, 205:605, 2003.
- H. Tawara, E. Takács, T. Suta, K. Makónyi, L.P. Ratliff, and J.D. Gillaspay. . *Phys. Rev. A*, 73:012704, 2006.
- A.C. Thompson, D. Vaughan, D.T. Attwood, E.M. Gullikson, M.R. Howells, J.B. Kortright, A.L. Robinson, J.H. Underwood, K.-J. Kim, J. Kirz, I. Lindau, P. Pianetta, H. Winick, G.P. Williams, and J.H. Scofield. X-ray data

- booklet. Center for X-ray Optics and Advanced Light Source, Lawrence Berkeley National Laboratory, January 2001. Second.
- K. Tőkési, L. Wirtz, C. Lemell, and J. Burgdörfer. . *Phys. Rev. A*, 64: 042902, 2001.
- Gy. Vîkor, R.T. Rajendra Kumar, Z.D. Pešić, N. Stolterfoht, and R. Schuch. . *Nucl. Instr. and Meth. B*, 233:218, 2005.
- B.J. Wargelin, P. Beiersdorfer, P.A. Neill, R.E. Olson, and J.H. Scofield. . *Astrophys. J.*, 634:687, 2005.
- Y. Yamazaki. . *Phys. Scr.*, T73:293, 1997.

BIBLIOGRAPHY

Acronyms

AFM Atomic Force Microscope

COB classical over-the-barrier

CTMC classical trajectory Monte Carlo

EBM electron beam mode

EBIS Electron Beam Ion Source

EBIT Electron Beam Ion Trap

FIB Focused Ion Beam

FWHM full width at half maximum

HCI highly charged ion

LBNL E. O. Lawrence Berkeley National Laboratory

LLNL Lawrence Livermore National Laboratory

MCP multi channel plate

MTM magnetic trapping mode

NCEM National Center for Electron Microscopy

NIST National Institute of Standards and Technology

REBIT Refrigerated EBIT

SEM Scanning Electron Microscope

ACRONYMS

List of Figures

1.1	Ultraviolet emission from HCIs in the solar corona	2
1.2	X-ray emission from Comet Hyakutake	4
1.3	Setup for aligned single ion implantation at LBNL	7
2.1	Schematic of an EBIT	15
2.2	Schematic of the trap region	16
2.3	Ionization energies of argon ions	20
2.4	Electron impact ionization cross sections vs. energy	21
2.5	Evolution of charge state and temperature of argon ions	26
3.1	Setup for magnetic trapping experiments	31
3.2	Timing pattern for magnetic trapping experiments	32
3.3	Leaky and pulse mode ion extraction	35
3.4	Magnet scan of extracted xenon ions	38
3.5	Wien filter scan of extracted argon ions	39
3.6	Schematic of Berlin EBIT extraction beamline	40
3.7	Reverse bias analysis of extracted argon ions	41
3.8	Rate of hole closing by platinum deposition	44
3.9	Targets for HCI-surface charge exchange experiments	45
3.10	Schematic of Berkeley EBIT extraction beamline	46
3.11	Electrostatic charge state analysis of transported ions	48
4.1	Potential diagram for HCI-gas charge exchange	53
4.2	Energy levels and electron cascade in Ar^{18+}	56
4.3	Photon emission spectrum simulated for capture into Ar^{18+} 8s	57
4.4	X-ray emission spectra simulated for capture into $\text{Ar}^{17+,18+}$ 8s	59
4.5	X-ray emission spectra simulated for capture into Ar^{18+} 8s–8j	60
4.6	X-ray emission spectra simulated for capture into Ar^{17+} 8s–8i	61
4.7	Comparison of hardness ratios from simulated spectra	63

LIST OF FIGURES

5.1	Scatter plot of x-ray emission from the EBIT	69
5.2	X-ray emission from the EBIT in EBM and MTM	70
5.3	Decay of x-ray emission during MTM	73
5.4	X-ray emission from Ar^{17+} charge exchange in the EBIT . . .	74
5.5	X-ray emission from $\text{Ar}^{17+,18+}$ charge exchange in the EBIT .	77
5.6	X-ray emission from Ar^{18+} charge exchange in the EBIT . . .	78
5.7	Hardness ratio vs. trap depth for $\text{Ar}^{17+,18+}$ charge exchange .	80
5.8	Hardness ratio time study for charge exchange in the EBIT . .	82
5.9	X-ray emission from Ar^{17+} charge exchange with a gas target .	84
5.10	X-ray emission from $\text{Ar}^{17+,18+}$ charge exchange with a gas target	85
5.11	X-ray emission from Ar^{18+} charge exchange with a gas target .	88
5.12	Ratio of K - to K^h -shell emission in Ar^{18+} extraction experiments	90
5.13	Hardness ratio vs. collision energy for $\text{Ar}^{17+,18+}$ charge exchange	91
5.14	Potential diagram for HCI-surface charge exchange	98
5.15	Schematic of HCI transport through a metallic aperture	99
5.16	Transport of Ar^{3+} through 100 nm holes in SiN	100
5.17	Percentage charge exchange vs. aperture diameter	103
5.18	Transport of Ar^{16+} and Xe^{44+} through 200 nm holes in SiN . .	105
5.19	Schematic of HCI transport through an insulating aperture . .	109

Acknowledgments

On the journey which has led to the completion of this thesis I have not been alone. I am indebted to many people for making this task possible and for supporting me along the way. I would now like to express my sincere thanks to them all.

I am most grateful to my Doktorvater, Prof. Dr. Gerd Fußmann, for giving me the opportunity to carry out my doctorate in the EBIT group of the Max Planck Institute for Plasma Physics in Berlin. Under his prudent guidance I have been able to pursue my research freely and have benefitted greatly from his insightful council. I am also very appreciative of the research stay at LBNL which he made possible and supported, and which has enriched my time as a PhD student considerably.

In the EBIT laboratory in Berlin I was able to work under the steadfast guidance of Dr. Christoph Biedermann and Dr. Rainer Radtke, from whom I learnt many tools of the trade. Their dedication to work for long hours alongside me on the experiment made the acquisition of the HCI-gas charge exchange data possible. I derived great benefit from our meticulous discussions of the experimental results. I also thank them sincerely for the time and care they took to critically evaluate the manuscript for this thesis.

The EBIT experiments in Berlin were supported by our technical colleagues Hans-Joachim Mans in the electronics workshop and Siegfried Mettchen in the machine shop. Their contributions were always highly valued and much appreciated.

I thank further members of the group in Berlin for their warmth and encouragement: Dr. Werner Bohmeyer, Mandy Baudach, Tilmann Lunt, Dennis Schröder, and Ole Waldmann. In addition, I would like to express my gratitude to Marlis Blaschke, for her kindness and assistance with administrative matters.

For the calculation of atomic data for the cascade simulations I am very grateful to Dr. Stephan Fritzsche. I have valued his collaboration greatly

ACKNOWLEDGMENTS

and enjoyed his ease of manner. I am also very pleased that he has agreed to write a Gutachten for this dissertation.

I also thank Prof. Dr. Oliver Benson for agreeing with equal readiness to write a Gutachten for this work.

At LBNL I was supervised by Dr. Thomas Schenkel, whom I owe considerable thanks for a very enjoyable year working in his group. His unassuming willingness to explain the underlying principles of experimental apparatus and physics concepts helped to consolidate my understanding significantly and has left a lasting impression on me.

Further members of the group in Berkeley included Dr. Joon Park, whom I thank for his help in the laboratory and for some entertaining escapades; Dr. Joe McDonald, for his support with the REBIT; Dr. Dieter Schneider, likewise for his support with the REBIT and for allowing me to run such long experiments with it; and Steve Wilde, for his expertise in the machine shop. In addition, I would like to express my gratitude to Dr. Andrew Minor from NCEM for his approachable nature and competent assistance with the FIB microscope.

Throughout the course of my PhD I have been supported by friends and family who have seen me through the ups and downs that such an undertaking can bring. I especially thank my parents, Mecki Spormann-Allen and Paul Allen. Over the years they have been a constant source of immeasurable strength and guidance, always giving their utmost to set me up in the best way possible and to provide me with all that I might need. Their understanding and support during the writing of this thesis has been a great help and I am very grateful for and moved by the effort they have gone to, to carefully proofread the manuscript.

I also thank my brother, Ansgar Allen, for his critical reading of chapters of this thesis, together with my sisters, Fabia and Zanna Allen, for their companionship and timely diversion. In addition, I would like to thank my aunt, Marlis Spormann-Lagodzinski, for helping me settle into Berlin and for her continued kindness. I am also very grateful to Marie-Luise Krebs and Bastian Schlagowsky for their close friendship.

Finally, I would like to express my heartfelt thanks to Dr. Arun Persaud, who has been there for me without fail since the day we met when I had just arrived in Berkeley for my year's stay at LBNL. Arun has contributed to the realization of this thesis in so many ways, as the very skillful yet modest physicist that he is and as a very special friend. I have been able to work alongside him in the laboratory and to discuss with him all aspects of this

ACKNOWLEDGMENTS

PhD. His patience and willingness to help are unending. It is hard to put into words how lucky I have been to find him.

ACKNOWLEDGMENTS

Curriculum Vitae

Personal Details

Full Name: Frances Isabel Allen
Date and Place of Birth: 22.12.1978, Portsmouth, England

Academic Development

Secondary School Education:
Simon Langton Grammar School, Canterbury, England 1990-1997
Further Education:
University of Southampton, England
University of Kent, England
Universität Tübingen, Germany 1997-2001
First Class Honours in Chemistry and Physics, M.Sci.
Technische Universität Berlin, Germany 2001-2002
Study of History and Philosophy of Science
Doctorate in Physics:
Max-Planck-Institut für Plasmaphysik Berlin, Germany 2002-2006
E. O. Lawrence Berkeley National Laboratory, CA, USA 2003-2004

Work Experience

NASA stardust project, University of Kent Summer 1998
Solid state NMR project, University of Kent Summer 1999
Electronic Nose research assistant, Universität Tübingen Jan-Jul 2000
Molecular modeling, University of Kent Summer 2000

CURRICULUM VITAE

Publications

F.I. Allen, C. Biedermann, R. Radtke, S. Fritzsche, and G. Fussmann, Energy Dependence of Angular Momentum Capture States in Charge Exchange Collisions between Slow Highly Charged Argon Ions and Argon Neutrals, *submitted to Physical Review A* (2007)

F.I. Allen, C. Biedermann, R. Radtke, and G. Fussmann, Charge Exchange of Highly Charged Argon Ions as a Function of Projectile Energy, *Journal of Physics: Conference Series*, 58:181 (2007)

C. Biedermann, R. Radtke, G. Fussmann, and F.I. Allen, Extreme Ultraviolet Spectroscopy of Highly Charged Argon Ions at the Berlin EBIT, *Journal of Physics: Conference Series*, 72:012004 (2007)

F.I. Allen, C. Biedermann, R. Radtke, and G. Fussmann, Extraction of Highly Charged Ions from the Berlin EBIT for Interactions with a Gas Target, *Review of Scientific Instruments*, 77:03B903 (2006)

F.I. Allen, A. Persaud, S.J. Park, A. Minor, M. Sakurai, D.H. Schneider, and T. Schenkel, Transport of Multiply and Highly Charged Ions through Nanoscale Apertures in Silicon Nitride Membranes, *Nuclear Instruments and Methods in Physics Research B*, 244:323 (2006)

A. Persaud, F.I. Allen, F. Gicquel, S.J. Park, J.A. Liddle, T. Schenkel, Tzv. Ivanov, K. Ivanova, I.W. Rangelow, and J. Bokor, Single Ion Implantation with Scanning Probe Alignment, *Journal of Vacuum Science and Technology B*, 22:2992 (2004)

CURRICULUM VITAE

A.M. Minor, F.I. Allen, V.R. Radmilovic, E.A. Stach, and T. Schenkel, Nanoscale Holes formed by *in situ* Thin Film Deposition in a FIB, *Microscopy and Microanalysis*, 10:1118 (2004)

S.J. Park, J.A. Liddle, A. Persaud, F.I. Allen, J. Bokor, and T. Schenkel, Formation of 15 nm Scale Coulomb Blockade Structures in Silicon by Electron Beam Lithography with a Bilayer Resist Process, *Journal of Vacuum Science and Technology B*, 22:3115 (2004)

A. Persaud, S.J. Park, J.A. Liddle, I.W. Rangelow, J. Bokor, R. Keller, F.I. Allen, D.H. Schneider, and T. Schenkel, Quantum Computer Development with Single Ion Implantation, *Quantum Information Processing*, 3:233 (2004)

Selbstständigkeitserklärung

Hiermit erkläre ich, die vorliegende Dissertation selbstständig und ohne unerlaubte Hilfe angefertigt zu haben.

Frances Allen
Berlin, den 22. Oktober 2007.